



Theses and Dissertations

---

2016-07-01

# Theoretical and Experimental Investigation of a Quadspectral Nonlinearity Indicator

Kyle Glen Miller  
*Brigham Young University*

Follow this and additional works at: <https://scholarsarchive.byu.edu/etd>



Part of the [Physical Sciences and Mathematics Commons](#)

---

## BYU ScholarsArchive Citation

Miller, Kyle Glen, "Theoretical and Experimental Investigation of a Quadspectral Nonlinearity Indicator" (2016). *Theses and Dissertations*. 8710.  
<https://scholarsarchive.byu.edu/etd/8710>

This Thesis is brought to you for free and open access by BYU ScholarsArchive. It has been accepted for inclusion in Theses and Dissertations by an authorized administrator of BYU ScholarsArchive. For more information, please contact [scholarsarchive@byu.edu](mailto:scholarsarchive@byu.edu), [ellen\\_amatangelo@byu.edu](mailto:ellen_amatangelo@byu.edu).

Theoretical and Experimental Investigation of a  
Quadspectral Nonlinearity Indicator

Kyle Glen Miller

A thesis submitted to the faculty of  
Brigham Young University  
in partial fulfillment of the requirements for the degree of  
Master of Science

Kent L. Gee, Chair  
Tracianne B. Neilsen  
Brian D. Jeffs

Department of Physics and Astronomy  
Brigham Young University

July 2016

Copyright © 2016 Kyle Glen Miller

All Rights Reserved

## ABSTRACT

### Theoretical and Experimental Investigation of a Quadspectral Nonlinearity Indicator

Kyle Glen Miller

Department of Physics and Astronomy, BYU  
Master of Science

Understanding the impact of jet noise and other high-amplitude sound sources can be improved by quantifying the nonlinearity in a signal with a single-microphone measurement. An ensemble-averaged, frequency-domain version of the generalized Burgers equation has been used to derive a quantitative expression for the change in spectral levels (in decibels) over distance due to geometric spreading, thermoviscous absorption, and nonlinearity, respectively. The nonlinearity indicator, called  $\nu_N$ , is based on the quadspectral Morfey-Howell indicator, which has been used in the past to characterize nonlinearity in noise waveforms. Unlike the Morfey-Howell indicator, the  $\nu_N$  indicator has direct physical significance, giving a change in decibels per meter of the sound pressure level spectrum specifically due to nonlinearity.

However, a detailed characterization of the expected behavior and potential issues for the nonlinearity indicator has been lacking. The quadspectral nonlinearity indicator is first calculated for well-known solutions to several basic acoustical scenarios to determine its expected behavior in both the near field and far field. Next, the accuracy of  $\nu_N$  is examined as a function of measurement parameters such as sampling frequency, signal bandwidth, scattering, and noise. Recommendations for conducting experiments are given based on the findings. Finally, the indicator is calculated for model-scale and military jet noise waveforms. These tests reveal the utility and accuracy of the  $\nu_N$  indicator for characterizing broadband noise; the indicator gives frequency-dependent information about the waveform from a single-point measurement.

Keywords: nonlinearity, acoustics, jet noise, Morfey-Howell, quadspectrum

## ACKNOWLEDGEMENTS

Funding for this research has come from the Small Business Innovation Research (SBIR) program, the Utah NASA Space Grant Consortium, the Air Force Research Laboratory (AFRL), and from Brigham Young University. I also wish to especially thank Drs. Kent Gee and Traci Neilsen for their strong encouragement and advisement during the year and a half that I have done research with them. I also thank Brent Reichman for his constant willingness to answer my incessant questions and my wife, Hannah Miller, for her continued patience.

# Table of Contents

<b>Title Page</b> .....	<b>i</b>
<b>Abstract</b> .....	<b>ii</b>
<b>Acknowledgements</b> .....	<b>iii</b>
<b>Table of Contents</b> .....	<b>iv</b>
<b>List of Tables</b> .....	<b>vi</b>
<b>List of Figures</b> .....	<b>vii</b>
<b>Chapter 1 Introduction</b> .....	<b>1</b>
1.1 Overview and Motivation .....	1
1.2 Background.....	2
1.2.1 Nonlinear Acoustics.....	2
1.2.2 Characterizing Nonlinearity.....	4
1.3 The $v_N$ Indicator .....	5
1.4 Thesis Outline .....	6
<b>Chapter 2 Theoretical Investigations with the Generalized Burgers Equation</b> .....	<b>8</b>
2.1 Blackstock Bridging Function .....	9
2.2 Mendousse Solution.....	12
2.3 Generalized Burgers Equation with Spherical Spreading.....	14
2.4 Summary of Indicator Trends .....	19
<b>Chapter 3 Practical Implementation and Issues</b> .....	<b>22</b>
3.1 Case Study: Sawtooth Waveform .....	22
3.2 Effect of Sampling Frequency: Sawtooth .....	25
3.2.1 Ideal Sawtooth Waveform .....	25
3.2.2 Bandlimited Sawtooth Waveforms .....	27
3.2.3 Experimental Sawtooth Waveform.....	29
3.2.4 Mendousse Solution Revisited.....	30
3.3 Effect of Sampling Frequency: Bandwidth.....	32
3.3.1 Narrowband Gaussian Noise.....	32
3.3.2 Experimental Broadband Noise .....	36
3.3.3 Broadband Noise from the Literature .....	38
3.4 Effect of Scattering and Measurement Noise .....	41
3.4.1 Effect of Scattering .....	41

3.4.2	Effect of Measurement Noise .....	42
3.5	Summary and Experimental Recommendations .....	43
<b>Chapter 4</b>	<b>Nonlinearity Analysis of Model-Scale Jet Data.....</b>	<b>46</b>
4.1	Spectral Analysis for Mach 2.0.....	46
4.2	Nonlinearity Analysis at Mach 2.0 .....	50
4.3	Comparison of Jet Conditions.....	53
4.3.1	Summary of Comparisons.....	56
<b>Chapter 5</b>	<b>Quadspectral Analysis of Military Aircraft Jet Noise Data.....</b>	<b>57</b>
5.1	Experimental Setup.....	57
5.2	Spectral Analysis .....	59
5.3	Nonlinearity Analysis .....	63
5.3.1	Spectral and Spatial Plots of $v_N$ for Minimum Afterburner .....	63
5.3.2	Comparison of Engine Conditions.....	67
5.3.3	Other Nonlinearity Metrics.....	71
<b>Chapter 6</b>	<b>Concluding Discussion.....</b>	<b>75</b>
6.1	Summary of Findings.....	75
6.2	Summary of Contributions.....	76
6.3	Implications and Recommendations .....	77
<b>References.....</b>		<b>79</b>
<b>Appendix A</b>	<b>Computing <math>v_N</math> for One-Third-Octave Bands.....</b>	<b>86</b>

# List of Tables

Table 2.1. Asymptotic values of $v_N$ and the sum $v_N + v_\alpha$ for the three cases studied in this chapter. .....	20
Table 3.1. Frequency ratio at which $v_N$ exhibits greater than 20% error for various cases. ....	44

# List of Figures

Figure 1.1. A sine wave of sufficient amplitude will nonlinearly deform into a sawtooth and begin to decay as it propagates. .... 2

Figure 2.1. (a) Progression of the BBF solution from a sinusoid to a sawtooth at various values of the normalized distance,  $\sigma$ . The shock first begins at  $\sigma = 1$  and reaches a maximum height at  $\sigma = \pi/2$ . (b) Amplitude coefficients of the waveform harmonics. Note the delayed onset of successive harmonics. (c) Waveform spectrum. This plot is simply a logarithmic scale of part (b). .... 9

Figure 2.2. Change in sound pressure level with distance for several harmonics. (a) Near field results for various harmonics. The colored lines represent the predicted change,  $v_N$ . The circles represent the numerical derivatives. Note that the values for all harmonics converge at about  $\sigma = 3$ . (b) Far field results for various harmonics. The asymptotic value is  $(\sigma + 1)^{-1}$ , or more loosely  $\sigma^{-1}$ . .... 11

Figure 2.3. (a) Comparison of the BBF and the Mendousse solution. (b)-(f) Values of  $v_N$ ,  $v_\alpha$ , their sum, and the actual numerical derivative (red circles). .... 13

Figure 2.4. (a) Harmonic amplitude of the Mendousse solution on a logarithmic scale at  $\sigma = 30$ . The decay of the high-frequency harmonic amplitude closely matches a linear exponential decay. (b) The  $v_N$  values at the same distance. Note the values are exactly as predicted in Eq. (2.8). .... 14

Figure 2.5. (a) Comparison of a linearly and nonlinearly propagated waveform at  $1000 D_f$  ( $\sigma \approx 6.9$ ). (b)-(d) The values of  $v_S$ ,  $v_\alpha$ ,  $v_N$ , their sum  $v$ , and the numerical derivatives (red circles) as a function of the scaled distance for various harmonics. .... 17

Figure 2.6. The  $v_N$  values at a radial normalized distance of about 10.6. Note the values are predicted from Eq. (2.11) to within 8% error. This propagated waveform had twice the initial amplitude as the waveform discussed in Fig. 2.5. .... 19

Figure 3.1. Example sawtooth waveform that is under study in this section. .... 23

Figure 3.2. (a) Calculations of  $v_N$  for an ideal sawtooth waveform sampled at various rates. (b) The error in  $v_N$  compared to the analytic value. A 20% error occurs at about one-quarter the sampling frequency. .... 26

Figure 3.3. PSD of the sawtooth waveform and the waveform squared. The cross-spectrum between these two values is used to calculate  $Q/S$ . Errors due to aliasing can be seen in both quantities. The blue, red, and green curves are sampled at 1024, 2048, and 4096 Hz, respectively. .... 26

Figure 3.4. (a) Calculations of  $v_N$  for a sawtooth waveform calculated from a truncated Fourier series for various sample rates. (b) The error in  $v_N$  compared to the analytic value. A 20% error occurs at about one-hundredth the sampling frequency, much lower than for the ideal sawtooth waveform. .... 27

Figure 3.5. PSD of the waveform and the waveform squared for a sawtooth calculated from a truncated Fourier series. The sampling rates for each color line are as in Fig. 3.4. There is

no aliasing error because the series is truncated. The error for the PSD of $x^2(t)$ is very large.....	28
Figure 3.6. (a) Experimentally measured sawtooth waveform. (b) Calculated value of $v_N$ . (c) Error from the expected analytic value. A 20% error occurs at about 2% the sampling frequency. (d) PSD of the waveform and waveform squared. Note the sharp rolloff in the waveform PSD and the large error in the waveform squared PSD.....	29
Figure 3.7. (a) Mendousse solution waveforms at various normalized distances with $\Gamma = 30$ . (b) Spectral amplitudes of the waveforms. (c) Percent error in the $v_N$ indicator. The vertical black line is at one-quarter the sampling frequency. The legend in part (a) applies to parts (b) and (c) as well.....	31
Figure 3.8. (a) Comparison of the linear (spreading and absorption), and output (including nonlinearity) waveforms. (b) Shock rise time of the largest shock in the waveform. The waveform quickly shocks up over a short distance. (c) The $v_N$ values for various distances. The $v_N$ curve at $1 D_j$ is zero everywhere. The vertical black line marks one-quarter the sampling frequency. (d) PSD at various distances. The initial spectrum at $1 D_j$ has a power-law decay in the high frequencies. Note the waveform becomes more broadband due to nonlinear harmonic generation.....	33
Figure 3.9. Values of $v_S$ , $v_\alpha$ , $v_N$ , their sum ( $v$ ), and the actual numerical derivative ( $\Delta L/\Delta D_j$ ) for six different harmonics of narrowband Gaussian noise. The fundamental frequency is defined as the center frequency of the lowest noise band. The agreement between the prediction and the numerical derivative worsens with harmonic number. ....	34
Figure 3.10. (a) PSDs of the computationally propagated narrowband Gaussian noise at various distances. (b) Percent error in $v_N$ for the same distances. At $1000 D_j$ , a 20% error occurs at about 5% the sampling frequency. ....	35
Figure 3.11. Predicted change in sound pressure level— $v$ , or the sum $v_S + v_\alpha + v_N$ —with numerical derivatives of the PSD levels between microphones. The derivatives are taken between (a) microphones 1 and 2, (b) microphones 2 and 3, and (c) microphones 3 and 4. ....	36
Figure 3.12. (a) PSDs of model-scale jet noise waveforms. (b) PSDs of the same model-scale jet noise waveforms squared. The PSDs of the waveforms squared exhibit a smooth behavior.....	38
Figure 3.13. One-third-octave (OTO) band (a) SPL and (b) $v_N$ values for F-35 noise data at two different power levels and with and without scattering. The scattering most adversely affects $v_N$ for the high-intensity noise. ....	41
Figure 3.14. (a) Values of $v_N$ for an ideal sawtooth waveform with added noise. (b) Error compared to the analytical value for the same. (c) PSD of the waveform and waveform squared. The noise more adversely affects the waveform squared PSD than the waveform PSD, creating the error. (d) OTO band averages of $v_N$ from part (a). The noise does not produce much effect for 80 and 100 dB SNR. ....	43
Figure 4.1. Plots for the Mach-2.0 model-scale jet noise data. (a) Overall sound pressure level (OASPL) for the microphone array. Circles represent 3.18-mm microphones and filled diamonds represent 6.35-mm microphones. (b) Peak frequency map.....	47

Figure 4.2. Sound pressure level maps for eight different frequencies at Mach 2.0. Note that the angle of radiation decreases (moves farther from the jet plume) with frequency. ....	48
Figure 4.3. (a) PSD for the six microphones along the principal radiation radial for Mach 2.0. Note the decrease in peak frequency along with a relatively constant high-frequency spectrum. (b) The $\nu_N$ values for the same microphones. The zero-crossing frequency of the indicator decreases with radius, tracking the decrease in peak frequency from part (a). ....	49
Figure 4.4. Spatial maps of $\nu_N$ for eight different frequencies at Mach 2.0. The transition to nonlinear loss (driving other harmonics) to nonlinear gain (being nonlinearly driven) can be seen.....	51
Figure 4.5. (a) Value of $\nu_\alpha$ (independent of position). The absorption decay closely follows a quadratic exponential decay from about 4 to 40 kHz. (b) Spatial map of $\nu_S$ . Its values are distinctly larger than either $\nu_\alpha$ or $\nu_N$ , showing that spreading is the most dominant effect. ....	52
Figure 4.6. (a) Value of the sum $\nu_N + \nu_\alpha$ along the principal radiation radial (145°) for Mach 2.0. Note that in the far field the sum is slightly negative. In addition, the rolloff with frequency is a linear exponential decay. (b) The same plot as (a) but on a logarithmic scale. Only negative values are shown. ....	53
Figure 4.7. (a) OASPL and (b) peak frequency spatial maps for Mach 0.85. (c)-(d) Similar maps for Mach 1.8.....	54
Figure 4.8. The $\nu_N$ values at 40 kHz for the three engine conditions: (a) subsonic (Mach 0.85), (b) overexpanded (Mach 1.8), and (c) ideally expanded (Mach 2.0). Parts (b) and (c) are plotted on the same scale. The nonlinearity for Mach 2.0 is nearly twice that at Mach 1.8. Part (c) is a copy of Fig. 4.4 (h). ....	54
Figure 4.9. The sum $\nu_N + \nu_\alpha$ on linear and logarithmic scales for (a)-(b) Mach 0.85 along 150° and (c)-(d) Mach 1.8 along 145°, respectively. The contribution due to nonlinearity is essentially zero for (a)-(b), the Mach-0.85 case, and the rolloff goes as absorption only (close to a quadratic exponential decay). For Mach 1.8, or (c)-(d), the rolloff approaches a linear exponential decay, though not as exact as in Fig. 4.6. The linear exponential decay does, however, indicate a reduction in the expected absorption decay due to nonlinearity. ....	55
Figure 5.1. Depiction of the experimental setup out to (a) 76.2 m (250 ft) and to (b) 305 m (1000 ft). The microphone array is centered 6.6 m (21.6 ft) behind the aircraft nozzle. Microphone angles ranged from 0° to 160° relative to the engine inlet. ....	58
Figure 5.2. Relative OTO SPL due to ground reflections at varying distances. Each curve was calculated based on the height of the microphone and modeling the ground with flow resistivity of 4000 kPa s/m <sup>2</sup> . ....	59
Figure 5.3. OASPL maps for each engine condition. The main radiation lobe moves upstream and levels increase with engine condition. ....	60
Figure 5.4. Peak frequency maps for each engine condition. Low frequencies are present in the peak radiation area, high frequencies perpendicular to the jet, and mid-range frequencies in the upstream direction.....	61

Figure 5.5. OTO SPL for six different angles and 130% ETR. Each plot displays the OTO SPL for all available microphones along the radial as a function of frequency. The peak frequency is larger for smaller angles. In addition, the rolloff at 1000 ft (305 m) is less at 130° and 135° than for the other angles.....	62
Figure 5.6. OTO $v_N$ values for six different angles. The curves that go negative for distances close to the source are erroneous and due to scattering in the PSDs. Strong nonlinearity is present for all angles. ....	64
Figure 5.7. Predicted and actual changes in sound pressure level between 500 and 1000 ft at angles of (a) 110° and (b) 135°. The nonlinear predictions (black lines) are generally closer to the numerical derivatives (red lines) than are the linear predictions (green lines). ....	65
Figure 5.8. Spatial maps of $v_N$ for eight different frequencies at 130% ETR. The trend shows loss of energy (negative values) at low frequencies and a transition to a gain of energy (positive values) at high frequencies. Ground reflections cause the 1-kHz data in (d) to be especially noisy.....	66
Figure 5.9. The spatial rate of change in SPL due to absorption, $v_a$ , as a function of frequency for typical measured weather conditions. The parameter $v_a$ is shown on a (a) linear and (b) logarithmic scale. ....	68
Figure 5.10. Spatial maps of $v_N$ . The first column shows $v_N$ at 100 Hz. Nonlinear losses are seen in the peak radiation range. The second column shows $v_N$ at 10 kHz. Nonlinear growth increases with engine condition, and the directivity moves upstream as well.....	69
Figure 5.11. Spatial maps of the sum $v_N + v_a$ at 10 kHz. Nonlinearity balances or overcomes absorption only for the 100%, 130%, and 150% engine conditions.....	70
Figure 5.12. Derivative skewness values for 130% ETR. The derivative skewness peaks at 76.2 m (250 ft) due to its dependence on the cube of the pressure derivative, or sensitivity to the largest shocks.....	72
Figure 5.13. Average steepening factor (ASF) for five engine conditions. Similar to $v_N$ and the derivative skewness, the breadth of the lobe increases with propagation. However, the ASF uniquely remains high in the far field.....	74

# Chapter 1

## Introduction

### 1.1 Overview and Motivation

Linear approximations accurately describe pressure waveforms for small oscillations about ambient conditions. However, loud sounds exhibit nonlinear effects when they are of sufficient amplitude. Waveforms steepen as they propagate, and shocks form as a result.<sup>1-3</sup> This occurs as the high (low) pressures at the peaks (troughs) of the waveform increase (decrease) the air temperature, which in turn increases (decreases) the local sound speed. The local changes in sound speed causes the peaks (troughs) to travel more quickly (slowly) than the rest of the waveform. When a peak overtakes a trough, a shock is formed. This general behavior causes high-amplitude sinusoidal waveforms to distort into sawtooth waves as they propagate and introduces nonlinear losses, seen in Fig. 1.1. This distortion introduces harmonics of the fundamental that are required to resolve the discontinuity.

However, most sounds of interest do not involve a simple sine wave, but are often stochastic, broadband signals. Recent work to measure the nonlinear evolution of acoustic waves has involved using microphones placed at various positions away from a source and characterizing the waveform evolution over distance<sup>4-7</sup> or using computer simulations to numerically propagate a waveform.<sup>8-10</sup> It is difficult to characterize nonlinear propagation effects

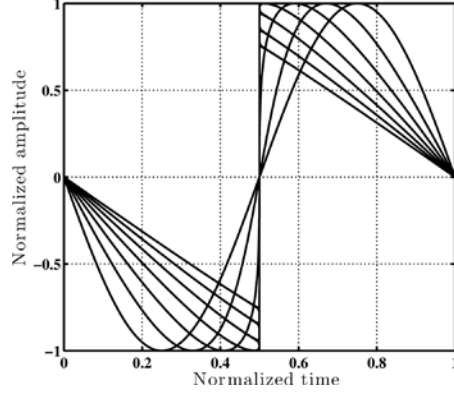


Figure 1.1. A sine wave of sufficient amplitude will nonlinearly deform into a sawtooth and begin to decay as it propagates.

based on a single measurement because such characterization relies on observing the distortion of waveforms and spectra across distance. The focus of this thesis is to develop, implement, and characterize a nonlinear indicator that will give information about shock formation, nonlinear losses, and the comparative strength of nonlinearity to other effects from a single waveform measurement.

## 1.2 Background

### 1.2.1 Nonlinear Acoustics

The nonlinear model equation that will be used in most of this thesis is the generalized Burgers equation (GBE):<sup>11</sup>

$$\frac{\partial p}{\partial r} + \frac{mp}{r} = \left( \frac{\beta}{\rho_0 c_0^3} \right) p \frac{\partial p}{\partial \tau} + \left( \frac{\delta}{2c_0^3} \right) \frac{\partial^2 p}{\partial \tau^2}, \quad (1.1)$$

where  $p$  is the sound pressure;  $m$  takes on values of 0, 0.5, or 1 for planar, cylindrical, and spherical waves, respectively;  $\beta$  is the coefficient of nonlinearity;  $\rho_0$  is the equilibrium density of air;  $c_0$  is the sound speed;  $\delta$  is the diffusivity of sound;  $r$  is the distance from the source; and  $\tau$  is the retarded time. Other, more generalized versions of the GBE have been used in nonlinear

modeling that include ray propagation and medium stratification.<sup>12, 13</sup> Future work could involve an analysis similar to that presented in Section 1.3, but for a more generalized model equation.

The rapidity and extent of the nonlinear deformation depends on the pressure waveform amplitude relative to ambient conditions. For an initially sinusoidal plane wave of frequency  $\omega$  and amplitude  $p_0$ , propagating in the  $x$  direction, the shock formation distance,  $\bar{x}$ , is defined as

$$\bar{x} = \frac{\rho_0 c_0^3}{\omega \beta p_0} . \quad (1.2)$$

The shape of a propagating waveform is dependent on the normalized distance,  $\sigma = x/\bar{x}$ . If there is no thermoviscous absorption, the waveform steepens until  $\sigma = 1$ , where the first pressure discontinuity appears. The shock continues to increase in amplitude until  $\sigma = \pi/2$ , where the pressure discontinuity is a maximum. After this distance the waveform begins to decay in amplitude due to the nonlinear losses that are present at the shock. In addition, after  $\sigma = 3$ , traditionally regarded as the onset of the sawtooth regime, the waveform continues to decay and remains a sawtooth for all subsequent distances.

In a thermoviscous medium, a plane wave of this type also experiences absorption according to the linear attenuation coefficient,  $\alpha$ , defined as

$$\alpha = \frac{\delta \omega^2}{2c_0^3} . \quad (1.3)$$

A useful parameter that quantifies the strength of nonlinearity compared to absorption is the well-known Gol'dberg number,  $\Gamma$ , which for a sinusoidal plane wave is defined as

$$\Gamma = \frac{1}{\bar{x}\alpha} = \frac{\beta \omega p_0}{\alpha \rho_0 c_0^3} . \quad (1.4)$$

The presence of absorption causes the shocks in a nonlinear waveform to be less steep than for a waveform without absorption. Because thermoviscous absorption increases with frequency, the

high frequencies required to resolve a pressure discontinuity—which are present in steepened waveforms—will eventually be attenuated and decrease the slope of the shock. This occurs in the old-age region, where the waveform continues to change shape, unlike the case with no absorption. The distance where the old-age region occurs depends on the value of  $\Gamma$ . The parameters in Eqs. (1.2)-(1.4) will be used in discussing the strength of the physical mechanism of nonlinearity.

## 1.2.2 Characterizing Nonlinearity

In hopes to gain further physical insight into wave propagation, many efforts have been made to characterize and quantify the degree of nonlinearity present in a waveform from the empirical data alone (i.e., without assuming that a particular model equation holds). These efforts involve using a variety of calculations to compute a nonlinearity indicator that will reveal quantitative information about the waveform. Examples of such nonlinearity indicators include the derivative skewness,<sup>5, 14</sup> average steepening factor,<sup>15</sup> bicoherence,<sup>16</sup> the Morfey-Howell indicator,<sup>7, 17-19</sup> and others.<sup>20-22</sup> Due to the ambiguity of some of these indicators, their calculation yields a qualitative rather than a quantitative analysis. For example, the derivative skewness value of a waveform is a single number, but without additional analysis the value carries with it little physical meaning. It is simply an intuitive classification that has been found to correlate with nonlinearity. It has only been recently that some physical meaning has been tied to the derivative skewness value.<sup>23</sup> Section 1.3 presents a new indicator that is both descriptive and carries physical insight.

### 1.3 The $\nu_N$ Indicator

In an attempt to reconcile the effects of geometric spreading, thermoviscous absorption, and nonlinearity, a frequency version of the GBE was used in conjunction with the Morfey-Howell indicator to derive a new nonlinearity indicator.<sup>24</sup> The Morfey-Howell indicator, known as  $Q/S$ , has been studied for a variety of signals<sup>25, 26</sup> and is defined below:

$$\frac{Q}{S} = \frac{Q_{pp^2}}{p_{\text{rms}}S_{pp}} = \frac{\text{Im}\{E[\mathcal{F}^*\{p(t)\}\mathcal{F}\{p^2(t)\}]\}}{p_{\text{rms}}S_{pp}} . \quad (1.5)$$

Here  $Q_{pp^2}$  is the imaginary part of the cross-spectral density (or quadspectral density) between the pressure and pressure squared waveforms,  $E$  denotes expectation value,  $\mathcal{F}$  denotes a Fourier transform,  $p_{\text{rms}}$  is the root-mean-square pressure, and  $S_{pp}$  is the autospectral or power spectral density. Taking the imaginary part reveals phase coupling between two different frequencies, which occurs in nonlinear harmonic generation. Sum and difference-frequency generation from steepening waves causes energy present in different harmonics to be phase coupled. This coupling is referred to as quadratic phase coupling (QPC) and has been studied using the bispectral density,<sup>16, 26-29</sup> defined as

$$S_{ppp}(f_1, f_2) = E[P(f_1)P(f_2)P^*(f_1 + f_2)] , \quad (1.6)$$

where  $P$  is the Fourier transform of the pressure waveform,  $p(t)$ . A normalization of the bispectral density, known as the bicoherence, has also been used to examine nonlinearity in jet-like signals.<sup>16</sup>

The definition of  $Q/S$  in Eq. (1.5), combined with the frequency-domain version of the GBE, yields an expression for the change in sound pressure level over distance:<sup>24</sup>

$$\frac{\partial L_p}{\partial r} = -10 \log_{10}(e) \times \left( \frac{2m}{r} + 2\alpha + \frac{\omega\beta p_{\text{rms}} Q}{\rho_0 c_0^3 S} \right) \equiv \nu_S + \nu_\alpha + \nu_N , \quad (1.7)$$

where  $L_p$  is the sound pressure level spectrum;  $10 \log_{10}(e) \approx 4.34$ ;

$$\begin{aligned}
\nu_S &\equiv -10 \log_{10}(e) \times \frac{2m}{r} , \\
\nu_\alpha &\equiv -10 \log_{10}(e) \times 2\alpha , \\
\nu_N &\equiv -10 \log_{10}(e) \times \frac{\omega\beta p_{\text{rms}} Q}{\rho_0 c_0^3 S} .
\end{aligned} \tag{1.8}$$

That is, Eq. (1.8) gives an expression for the change in sound pressure level over distance due to geometric spreading, thermoviscous absorption, and nonlinearity, respectively. These indicators are especially useful because not only do they relate these separate effects directly to each other, but they do so in a meaningful way. Their values carry physical meaning, as defined in Eq. (1.7).

Trends in the sum of  $\nu_\alpha + \nu_N$  will be examined in Chapters 4 and 5. This sum gives the change in sound pressure level due essentially to a modified absorption. Similar to this sum is the spectral Gol'dberg number,  $\Gamma_s$ , defined by Falco to be<sup>25</sup>

$$\Gamma_s = \frac{\omega\beta}{2\alpha\rho_0 c_0^3} \frac{Q_{pp^2}}{S_{pp}} . \tag{1.9}$$

In fact, this quantity is most closely related to the difference of  $\nu_N - \nu_\alpha$ , which directly compares the strength of nonlinearity and absorption. The sum  $\nu_\alpha + \nu_N$  can be written as

$$\nu_\alpha + \nu_N = 20\alpha \log_{10}(e) [1 + \Gamma_s] , \tag{1.10}$$

but is not a comparison of the two effects. The sum  $\nu_\alpha + \nu_N$  will be used in this thesis to compute the added effects of absorption and nonlinearity.

## 1.4 Thesis Outline

The objective of this thesis is to determine the utility, potential issues, and quantitative behavior of a quadspectral nonlinearity indicator,  $\nu_N$ , through numerical investigation and jet noise analysis. Chapter 2 explores the near-field and asymptotic behavior of the indicator for

various solutions to the GBE. This includes solutions with and without geometric spreading and thermoviscous absorption. Performing the actual calculations described by Eq. (1.7) on a waveform produces some complications, and these are treated in Chapter 3. Chapter 4 applies the  $v_N$  calculations to model-scale jet data, and Chapter 5 treats the full-scale jet data. These chapters show that even though there are complications that are not fully understood, the analysis seems to work well for broadband data.

## Chapter 2

# Theoretical Investigations with the Generalized Burgers Equation

This chapter investigates the behavior of the quadspectral nonlinearity indicator,  $v_N$  [see Eq. (1.8)], when dealing with well-known solutions. This will give more insight to the expected behavior of  $v_N$  when dealing with experimental data. The first three sections in this chapter deal with three different solutions to the generalized Burgers equation (GBE). The first, the Blackstock Bridging Function (BBF),<sup>30</sup> assumes no geometric spreading and no thermoviscous absorption. In other words, the geometric spreading factor,  $m$ , and diffusivity of sound,  $\delta$ , in Eq. (1.1) are both set equal to zero. This makes for a simple case that isolates nonlinear effects. In addition, the BBF has an exact solution that is valid for all distances. The second, the Mendousse solution,<sup>31</sup> assumes no geometric spreading but includes thermoviscous absorption (i.e., only  $m$  is set to zero). This case allows for a direct comparison of nonlinearity and absorption effects with an elegant solution that is also valid for all distances. The third and final case is a numerical solution to the GBE with spherical spreading, thermoviscous absorption, and nonlinearity.<sup>8</sup> There is no known analytical solution to this equation that is valid for all distances, but there are analytical expressions valid in the far field for weak and strong waves that will be examined briefly.<sup>32</sup> The final section summarizes what was found.

## 2.1 Blackstock Bridging Function

The BBF was originally intended to be a connecting solution between the Fubini and Fay solutions to the Burgers equation.<sup>30</sup> It is valid for a lossless propagating plane wave, which has  $m = 0$  and  $\delta = \alpha = 0$  ( $\Gamma = \infty$ ) in Eq. (1.7). The solution is represented as an infinite sum,

$$p(\sigma, \tau) = p_0 \sum_{n=1}^{\infty} B_n(\sigma) \sin(\omega_n \tau) , \quad (2.1)$$

where  $p_0$  is a constant and  $\omega_n = n\omega$ . The amplitude of the  $n^{\text{th}}$  harmonic,  $B_n$ , is given by

$$B_n(\sigma) = \frac{2}{n\pi} V_b + \frac{2}{n\pi\sigma} \int_{\Phi_{\min}}^{\pi} \cos\{n[\Phi - \sigma \sin(\Phi)]\} d\Phi , \quad (2.2)$$

where  $V_b$  is a solution to the transcendental equation

$$V_b = \sin(\sigma V_b) , \quad (2.3)$$

and  $\Phi_{\min}$  is specified as

$$\Phi_{\min} = \begin{cases} 0, & 0 \leq \sigma < 1 \\ \sigma V_b, & \sigma \geq 1 \end{cases} . \quad (2.4)$$

The shape of the propagating waveform is dependent only on the normalized distance,  $\sigma = x/\bar{x}$ , as described in Section 1.2.1. Figure 2.1 (a) shows the evolution of the waveform from  $\sigma = 0$  to  $\sigma = 3$ . Note that the waveform first steepens until  $\sigma = 1$ , where the first pressure discontinuity

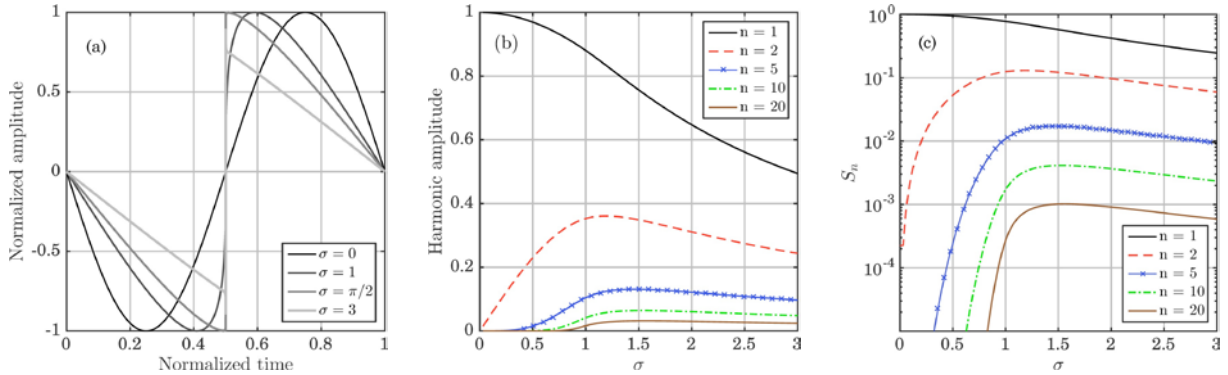


Figure 2.1. (a) Progression of the BBF solution from a sinusoid to a sawtooth at various values of the normalized distance,  $\sigma$ . The shock first begins at  $\sigma = 1$  and reaches a maximum height at  $\sigma = \pi/2$ . (b) Amplitude coefficients of the waveform harmonics. Note the delayed onset of successive harmonics. (c) Waveform spectrum. This plot is simply a logarithmic scale of part (b).

appears. The shock continues to increase in amplitude until  $\sigma = \pi/2$ , where the pressure discontinuity is a maximum (i.e., the entire height of the waveform). After this distance the waveform begins to decay in amplitude due to the nonlinear losses that are present at the shock. In addition, after  $\sigma = 3$ , traditionally regarded as the onset of the sawtooth regime, the waveform continues to decay and remains a sawtooth for all subsequent distances.

Based on the above behavior, the values of  $\nu_N$  can be calculated from the BBF waveform. For the fundamental frequency,  $\nu_N$  should always be negative. This is because the waveform progresses from a single-frequency sinusoid to a sawtooth with multiple harmonics; these harmonics are generated from the energy contained in the fundamental frequency. The value of  $\nu_N$  for higher harmonics will initially be positive ( $+\infty$ ) as the amplitude coefficients become nonzero, whose growth is seen in Figs. 2.1 (b)-(c). As the waveform steepens, an increasingly greater number of harmonics will need to be included in the sum because of their delayed onset relative to each other, easily visible in Fig. 2.1 (c). However,  $\nu_N$  will eventually be negative for all harmonics because the waveform will have reached a constant shape and has simply begun to decay. After a certain distance, all harmonics begin to decay at the same rate. From part (c) this appears to happen around  $\sigma = 2$ , but this plot only includes up to the 20<sup>th</sup> harmonic. Based on the traditional onset of the sawtooth regime, after which the waveform preserves its general sawtooth shape, the uniform decay will begin to occur for  $\sigma > 3$ .

Figure 2.2 (a) shows the values of  $\nu_N$  for several harmonics. The colored lines represent the predicted change in sound pressure level ( $\nu_N$ ), and the circles represent the actual change in harmonic level (obtained by taking numerical derivatives). In order for the predicted and actual values to converge to an error of less than 5%, 12,000 terms were used in Eq. (2.1) with 24,000 samples per period. (The error was less than 1% for all but the 20<sup>th</sup> harmonic.) Note that the

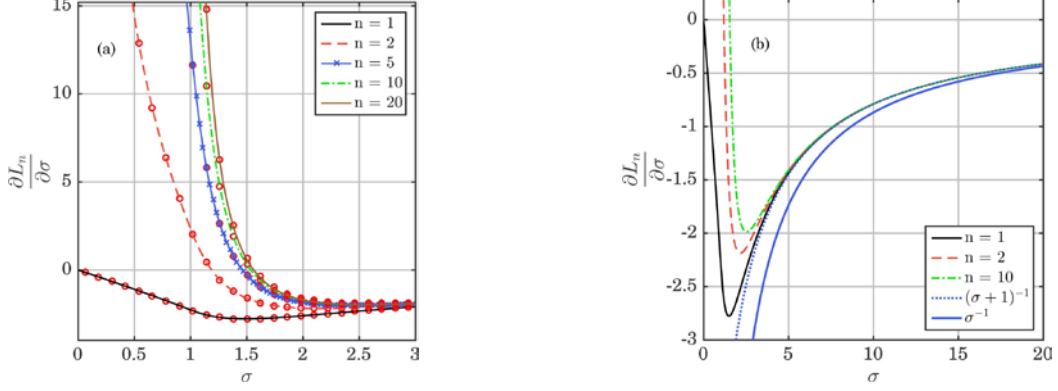


Figure 2.2. Change in sound pressure level with distance for several harmonics. (a) Near field results for various harmonics. The colored lines represent the predicted change,  $v_N$ . The circles represent the numerical derivatives. Note that the values for all harmonics converge at about  $\sigma = 3$ . (b) Far field results for various harmonics. The asymptotic value is  $(\sigma + 1)^{-1}$ , or more loosely  $\sigma^{-1}$ .

values for the fundamental harmonic are always negative. The curves for harmonics other than the fundamental begin at  $+\infty$  and eventually go negative. It appears that the curves for most of the harmonics become negative close to  $\sigma = \pi/2$ . This is where the maximum shock height has been reached, and it can be seen from Figs. 2.1 (b)-(c) that the harmonic amplitudes are decaying at this distance. The curves for all harmonics appear to be converging to the same value, and they are nearly converged at  $\sigma = 3$ . This is as expected, because at this point the waveform shape is essentially constant and is decaying. Each harmonic should decay at the same rate, as observed from the uniform negative slope of the harmonic amplitudes in Fig. 2.1 (c). However, the asymptotic value for  $v_N$  is not simply a constant. As derived by Reichman *et al.*,<sup>24</sup> in the old-age region

$$v_N = \frac{\partial L_n}{\partial \sigma} = -20 \log_{10}(e) (\sigma + 1)^{-1} \approx -20 \log_{10}(e) \sigma^{-1} . \quad (2.5)$$

This convergence can be seen in Fig. 2.2 (b). Eq. (2.5) can also be recast as a derivative in  $x$  to obtain

$$v_N = \frac{\partial L_n}{\partial x} = -20 \log_{10}(e) (x + \bar{x})^{-1} \approx -20 \log_{10}(e) x^{-1} . \quad (2.6)$$

## 2.2 Mendousse Solution

The Mendousse solution incorporates not only nonlinearity, but also thermoviscous absorption in the GBE. This is represented by  $m = 0$  in Eq. (1.7). The form of the solution is given by Pierce as<sup>31</sup>

$$p = p_0 \frac{\frac{4}{\Gamma} \sum_{n=1}^{\infty} (-1)^{n+1} I_n \left( \frac{\Gamma}{2} \right) n e^{-n^2 \sigma / \Gamma} \sin(\omega_n \tau)}{I_0 \left( \frac{\Gamma}{2} \right) + 2 \sum_{n=1}^{\infty} (-1)^n I_n \left( \frac{\Gamma}{2} \right) e^{-n^2 \sigma / \Gamma} \cos(\omega_n \tau)}, \quad (2.7)$$

where  $I_n$  is the modified Bessel function of the first kind. Because thermoviscous absorption increases with frequency, the shocks will not be as steep as they were for the BBF at the same scaled distance,  $\sigma$ . The variability between the two solutions depends on  $\Gamma$ . In the limit that  $\Gamma \rightarrow \infty$ , the solutions will be the same. A comparison of the waveform shape for the BBF and the Mendousse solution with  $\Gamma = 30$  at  $\sigma = \pi/2$  is shown in Fig. 2.3 (a). Note the smoother function provided by the Mendousse solution for this value of  $\Gamma$ .

Based on similar behavior to the BBF solution, some of the general trends in  $v_N$  should remain the same. For example, the waveform begins as a monofrequency sinusoid and begins to deform, so  $v_N$  for the fundamental harmonic should always be negative. For higher harmonics,  $v_N$  should start at  $+\infty$  as they begin to grow from a zero value. However, at this point the asymptotic value of  $v_N$  remains uncertain because there are now two competing effects: nonlinearity and thermoviscous absorption. It is certain that the asymptotic value of  $v_N + v_\alpha$  should be negative, since the old-age waveform will eventually decay.

However, additional insight can be gained from discussion of the asymptotic behavior of solutions to the GBE incorporating only nonlinearity and thermoviscous absorption. Blackstock gives an old-age, asymptotic expression for a pure-tone, high-amplitude plane wave at great distance ( $\alpha_0 x \gg 1$ ) and shows that the term corresponding to decay goes as  $e^{-n\alpha_0 x}$  (or equivalently

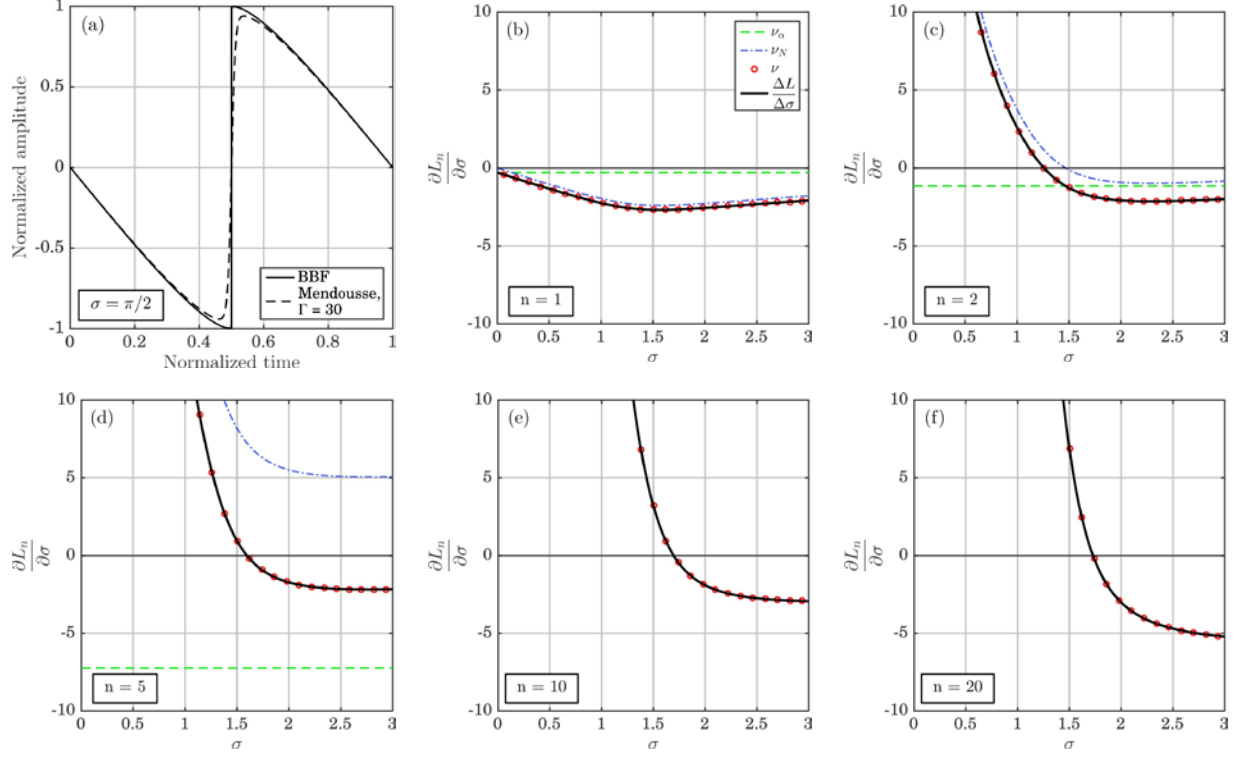


Figure 2.3. (a) Comparison of the BBF and the Mendousse solution. (b)-(f) Values of  $v_N$ ,  $v_\alpha$ , their sum, and the actual numerical derivative (red circles).

$e^{-n\sigma/\Gamma_0}$ .<sup>32</sup> Here  $\alpha_0$  and  $\Gamma_0$  are the absorption coefficient and Gol'dberg number for the fundamental frequency, respectively. The expected decay from absorption is  $e^{-n^2\alpha_0x}$ , much greater than seen in the asymptotic solution. In this paper, the  $e^{-n\alpha_0x}$  and  $e^{-n^2\alpha_0x}$  decays will be referred to as linear and quadratic exponential decays, respectively. Since  $v_\alpha$  goes approximately as  $-n^2\alpha_0$  (proportional to the square of the frequency) and the sum  $v_N + v_\alpha$  should go as  $-n\alpha_0$ , then  $v_N$  should go asymptotically as

$$v_N = 20 \log_{10}(e) (n^2 - n)\alpha_0 . \quad (2.8)$$

Thus it is expected that the asymptotic (old-age) value of  $v_N$  is positive for all harmonics.

The values for  $v_\alpha$ ,  $v_N$ , their sum, and the numerical derivative are shown in Fig. 2.3 (b)-(f) for the fundamental along with harmonics 2, 5, 10, and 20. The values are as expected, with both nonlinearity and absorption being negative for the fundamental, and the asymptotic values for  $v_N$

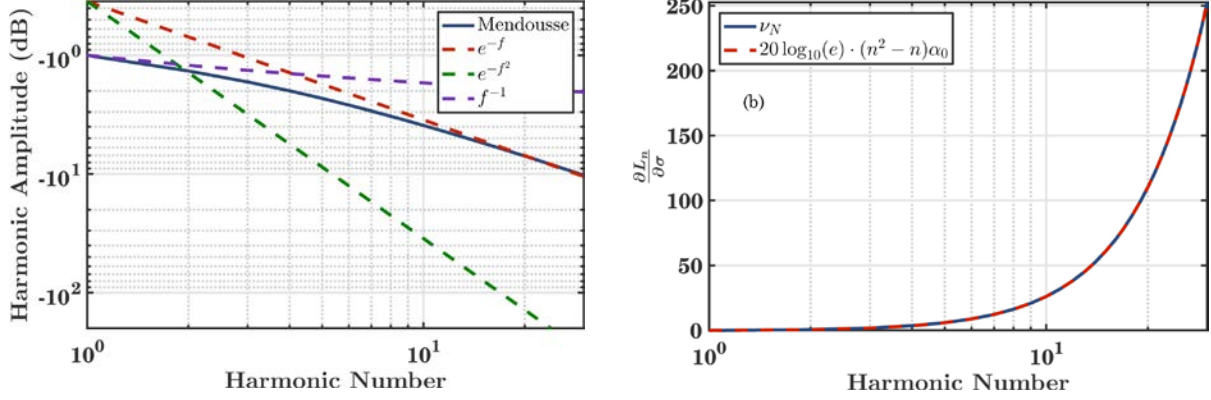


Figure 2.4. (a) Harmonic amplitude of the Mendousse solution on a logarithmic scale at  $\sigma = 30$ . The decay of the high-frequency harmonic amplitude closely matches a linear exponential decay. (b) The  $\nu_N$  values at the same distance. Note the values are exactly as predicted in Eq. (2.8).

being positive for all higher harmonics. Note that  $\nu_N$  for the second harmonic in part (b) is actually negative for some distances before eventually converging to a positive value (not pictured here). The propagation distance at which each harmonic reaches the asymptotic value varies, however. The sum  $\nu_N + \nu_a$ , red circles in parts (c)-(f), becomes increasingly negative and is proportional to harmonic number rather than the square of harmonic number, as expected. In fact, the spectrum of the waveform in the old-age region (arbitrary distance of  $\sigma = 30$ ) is shown in Fig. 2.4 (a). Linear ( $e^{-f}$ ) and quadratic ( $e^{-f^2}$ ) exponential decay curves are also shown along with a  $1/f$  power-law slope (or  $1/f^2$  spectral slope). The decay initially follows the  $1/f$  slope, as expected from a sawtooth, but at high frequencies the behavior is more like a linear exponential, as expected from a nonlinearly decaying waveform in the far field. Part (b) shows the  $\nu_N$  values as a function of frequency, and they are exactly as predicted in Eq. (2.8).

### 2.3 Generalized Burgers Equation with Spherical Spreading

There is no analytical solution that solves the GBE with spherical spreading, thermoviscous absorption, and nonlinearity. However, a numerical solution can be attained using known methods that propagate an initial waveform with the model equations.<sup>8</sup> The numerical

method is used in this section to perform a similar analysis as with the BBF and the Mendousse solution. In addition, there are asymptotic expressions for weak and strong spherical waves.<sup>32</sup> Let the numerical source consist of a pulsating sphere of radius  $r_0$ . For weak waves the asymptotic solution, including harmonics up through the fourth, is obtained from a perturbation solution of the Burger's equation:<sup>33</sup>

$$p = p_0 \sum_{n=1}^4 \left(\frac{r_0}{r}\right)^n \left(\frac{\Gamma}{4}\right)^{n-1} e^{-n\alpha_0(r-r_0)} \sin(\omega_n \tau) . \quad (2.9)$$

Once again, the thermoviscous absorption term goes as a decaying exponential linear with harmonic number as opposed to quadratic. However, the geometric spreading shockingly goes as  $r^{-n}$  as opposed to  $r^{-1}$ , as expected with linear theory. This is also true for the asymptotic expression for strong waves:<sup>34</sup>

$$p = p_0 \frac{4}{\Gamma} \sum_{n=1}^{\infty} K^n \left(\frac{r_0}{r}\right)^n e^{-n\alpha_0(r-r_0)} \sin(\omega_n \tau) , \quad (2.10)$$

where  $K^n$  is an undetermined constant (independent of  $r$ ). The same spreading and absorption dependencies are evident.

Ultimately a decay of  $r^{-n} e^{-n\alpha_0 r}$  is slower than the linear decay of  $r^{-1} e^{-n^2 \alpha_0 r}$  in the limit that  $r \rightarrow \infty$  and for  $n > 1$ .<sup>32, 33</sup> The difference between the nonlinear and linear decay rates is given by the asymptotic value of  $v_N$ . Since the nonlinear decay rate is less than the linear decay rate, the difference between the rates is positive, and  $v_N$  is expected to be positive in the far field. However, the positive value of the indicator should be smaller than its value for the Mendousse solution: the indicator not only conveys a reduction in absorption (positive value) but also an increase in spreading (slight negative value). From Eq. (1.7), it can be shown that the asymptotic

value of  $\nu_N$  should be proportional to the derivative of the logarithm of the ratio of nonlinear to linear asymptotic decay rates:

$$\begin{aligned}
\nu_N &= 20 \log_{10}(e) \frac{\partial}{\partial r} \ln \left( \frac{(r_0/r)^n e^{-n\alpha_0(r-r_0)}}{(r_0/r) e^{-n^2\alpha_0(r-r_0)}} \right) \\
&= 20 \log_{10}(e) \frac{\partial}{\partial r} \ln \left( (r_0/r)^{n-1} e^{(n^2-n)\alpha_0(r-r_0)} \right) \\
&= 20 \log_{10}(e) \left[ -\frac{(n-1)}{r} + (n^2-n)\alpha_0 \right] .
\end{aligned} \tag{2.11}$$

Both the (positive) reduction in absorption and (negative) increase in spreading are seen in Eq. (2.11). The  $\nu_N$  asymptotic value for a spherically spreading wave is the same as for the Mendousse solution in Eq. (2.8), but with an added negative term due to spreading. Other trends in  $\nu_N$  are expected to be the same as they were for both the BBF and the Mendousse cases:  $\nu_N$  should always be negative for the fundamental and start at  $+\infty$  for harmonics other than the fundamental.

To verify the asymptotic behavior, a sinusoidal waveform with parameters similar to the model-scale jet experiment<sup>35</sup> in Chapter 4 was numerically propagated using the GBE with spherical spreading, thermoviscous absorption, and nonlinearity.<sup>8</sup> However, unlike the jet noise case—which exhibits range, angle, and frequency-dependent geometric spreading—spherical spreading was assumed at all distances. The distance was scaled with respect to a jet nozzle diameter ( $D_j$ ), equal to 3.5 cm. In addition, the radial shock formation distance,  $\bar{r}$ , can be found from the linear shock formation distance,  $\bar{x}$ , defined in Eq. (1.2) by<sup>13</sup>

$$\bar{r} = r_0 \exp \left( \pm \frac{\bar{x}}{r_0} \right) , \tag{2.12}$$

where  $r_0$  is either the source radius or a position where the waveform is known to be sinusoidal. Because a spherical wave continually diverges, the radial equivalent of the linear normalized

distance,  $\sigma = x/\bar{x}$ , cannot be found simply by taking  $r/\bar{r}$ . Instead, the equivalent radial distance at which a particular value of the linear normalized distance occurs is calculated as

$$r = r_0 \exp\left(\pm \frac{\sigma \bar{x}}{r_0}\right), \quad (2.13)$$

where  $\sigma$  takes on a particular value.

The atmospheric conditions were taken to be the same as in the experiment, with temperature at 22.9°C, atmospheric pressure at 96.8 kPa, and relative humidity at 53%. However, only thermoviscous—not atmospheric—absorption was simulated. The fundamental frequency of the wave was 4 kHz with amplitude of 22 kPa at 1  $D_j$ , so as to approximate the root-mean-square amplitude of the jet data at 10  $D_j$ . For accuracy in the calculations, a sampling frequency of 88 MHz was used with  $2^{16}$  total samples. Details about the accuracy and sampling frequency will be treated in Section 3.2. Figure 2.5 (a) compares the nonlinearly propagated wave with the linear approximation (includes only spreading and thermoviscous absorption) at a

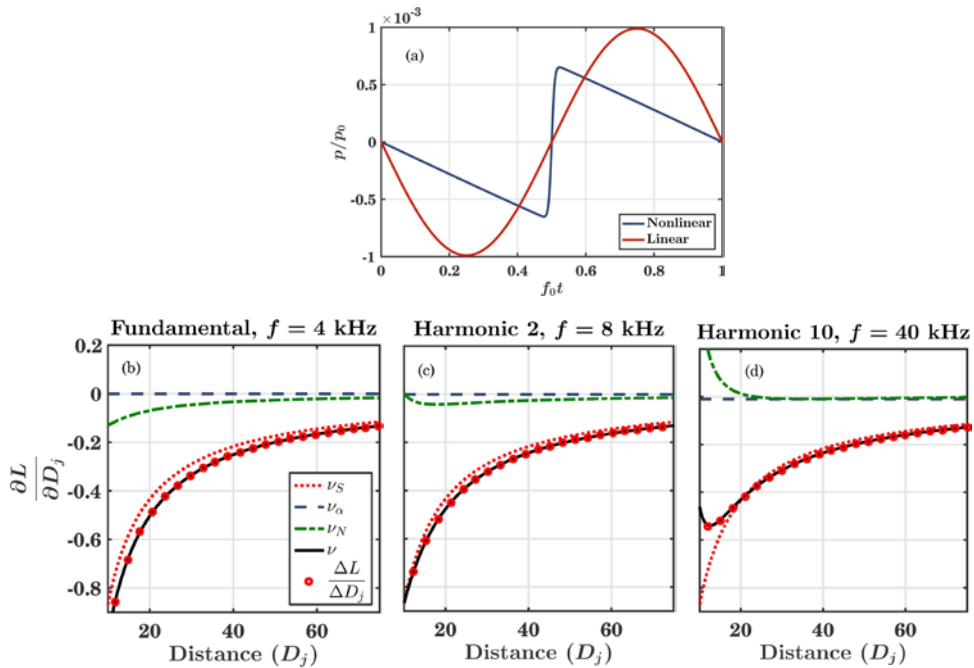


Figure 2.5. (a) Comparison of a linearly and nonlinearly propagated waveform at 1000  $D_j$  ( $\sigma \approx 6.9$ ). (b)-(d) The values of  $v_S$ ,  $v_a$ ,  $v_N$ , their sum  $v$ , and the numerical derivatives (red circles) as a function of the scaled distance for various harmonics.

distance of  $1000 D_j$  ( $\sigma \approx 6.9$ ). Relative to linear propagation, significant wave steepening has occurred along with a slight decrease in the peak-to-peak pressure.

The calculated  $v_S$ ,  $v_\alpha$ , and  $v_N$  indicators, along with their sum, are shown in Fig. 2.5 (b)-(d) as a function of distance for the fundamental, second harmonic, and tenth harmonic. A solid black line shows  $v$ , the sum of  $v_S$ ,  $v_\alpha$ , and  $v_N$ , and the red circles represent the numerically calculated derivative from the waveform itself. The percent error between the two is less than 1% for all values shown.

Very close to the source,  $v_N$  is positive for all harmonics as they are first generated nonlinearly. Not pictured in part (c),  $v_N$  is positive for the second harmonic at a distance less than  $10 D_j$ . However, nonlinear losses at the shock and energy transfer to even higher frequencies cause  $v_N$  to eventually go negative for some of the harmonics, as seen in Figs. 2.5 (c)-(d). The  $v_N$  value for the tenth harmonic eventually goes positive again at  $100 D_j$ . For higher harmonics not pictured here,  $v_N$  decreases but remains positive away from the source. If propagated far enough, the asymptotic value of  $v_N$  is positive for each harmonic other than the fundamental, confirming that the modified nonlinear decay ( $r^{-n} e^{-n\alpha_0 r}$ ) is ultimately slower than the linear decay ( $r^{-1} e^{-n^2 \alpha_0 r}$ ).

To compare the asymptotic value of  $v_N$  to theory, a wave similar to that discussed in Fig. 2.5, but with twice the initial amplitude, was computationally propagated.<sup>8</sup> This allowed for propagation into the old-age region without the waveform amplitude becoming too small to simulate. Figure 2.6 shows a spectral plot of  $v_N$  at a radial normalized distance of about  $\sigma \approx 10.6$ , which from Eq. (2.13) gives a radial distance of  $42,235 D_j$ . For perspective, the waveform in Fig. 2.5 (a) is at a radial normalized distance of about  $\sigma \approx 6.9$  ( $1000 D_j$ ). The  $v_N$  curve is compared against the theoretical value from Eq. (2.11) along with the theoretical value from the Mendousse solution in Eq. (2.8), which lacks the spreading term. The  $v_N$  values closely follow

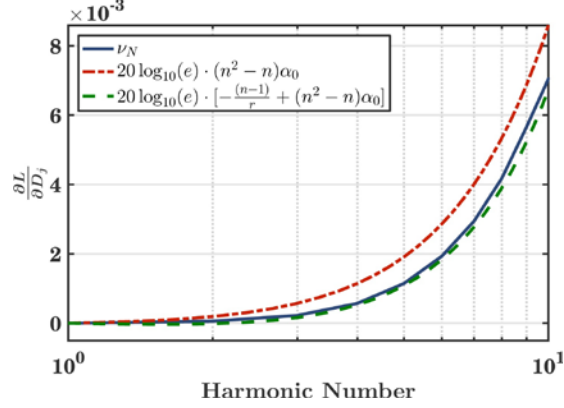


Figure 2.6. The  $v_N$  values at a radial normalized distance of about 10.6. Note the values are predicted from Eq. (2.11) to within 8% error. This propagated waveform had twice the initial amplitude as the waveform discussed in Fig. 2.5.

the expected behavior from Eq. (2.11) to within 8% error, confirming that nonlinear effects increase the spreading decay and slow the absorption decay in the far field. Future work involves using the radial shock formation distance for a spherical wave and analyzing the behavior and accuracy of  $v_N$  as a function of the radial normalized distance. Simulations with signals of varying bandwidth and Gol'dberg number could be tested to evaluate the accuracy of  $v_N$  as a function of these parameters.

## 2.4 Summary of Indicator Trends

The behavior of the quadspectral nonlinearity indicator  $v_N$  has been examined for three types of solutions to the GBE: the BBF, which includes only nonlinearity and ignores spreading and thermoviscous absorption; the Mendousse solution, which includes nonlinearity and absorption with no spreading; and a numerical solution that includes spherical spreading, thermoviscous absorption, and nonlinearity. In this section the behaviors of the various indicators are summarized for the three different solutions.

The asymptotic value of  $v_N$  represents any deviations from linear theory in waveform propagation in the old-age region. This value is given in the second column of Table 2.1 for the

Table 2.1. Asymptotic values of  $\nu_N$  and the sum  $\nu_N + \nu_\alpha$  for the three cases studied in this chapter.

<b>Assumptions (solution)</b>	<b>Asymptotic value of <math>\nu_N</math> [divided by <math>20 \log_{10}(e)</math>]</b>	<b>Asymptotic value of <math>\nu_N + \nu_\alpha</math> [divided by <math>20 \log_{10}(e)</math>]</b>
Nonlinearity only (BBF)	$-1/x$	$-1/x$
Absorption and nonlinearity (Mendousse)	$(n^2 - n)\alpha_0$	$-n\alpha_0$
Spherical spreading, absorption and nonlinearity (computational)	$-(n - 1)/r + (n^2 - n)\alpha_0$	$-(n - 1)/r - n\alpha_0$

three cases studied in this chapter. The BBF has a negative asymptotic value because of the nonlinear losses at the shock. The waveform in the old-age region is simply decaying while preserving its shape, so the change in all harmonics is negative. The Mendousse solution has a positive asymptotic value because the nonlinear decay of  $e^{-n\alpha_0 x}$  is less than the linear decay of  $e^{-n^2\alpha_0 x}$ . Similarly, the spherical solution has a positive asymptotic value because the nonlinear decay of  $r^{-n} e^{-n\alpha_0 r}$  is less than the decay predicted by linear theory of  $r^{-1} e^{-n^2\alpha_0 r}$ . However, the increase in the spherical spreading decay adds an extra negative term to  $\nu_N$  for this case, seen in the third row and second column of Table 2.1. In both the Mendousse and spherically spreading cases, the difference between the nonlinear and linear decay rates is given by  $\nu_N$ .

The asymptotic value of  $\nu_N + \nu_\alpha$  represents the total absorption decay (with compensation from nonlinearity) and any modifications to geometric spreading in the old-age region. This value is given in the third column of Table 2.1 for the three cases. The sign of  $\nu_N + \nu_\alpha$  is negative for each case. The spherical solution has the most negative asymptotic value because there is a linear ( $e^{-f}$ ) exponential decay due to absorption [albeit smaller than the quadratic ( $e^{-f^2}$ ) exponential decay for linear theory] and an increased decay in spreading. The Mendousse solution has a negative asymptotic value slightly smaller in magnitude than the spherical solution because there is a linear exponential decay due to absorption (rather than quadratic exponential decay) but no spreading. The BBF has a negative asymptotic value that is smallest in magnitude

because the decay goes as inverse distance. The only contribution to the  $\nu_N + \nu_\alpha$  sum for this case is from  $\nu_N$  because  $\nu_\alpha = 0$ .

# Chapter 3

## Practical Implementation and Issues

The previous chapter demonstrated the behavior of the indicators under study in a theoretical manner. When using numerical simulations, it is easy to increase the sampling frequency and the number of terms in sums until good results are obtained. When implementing the calculations for  $v_N$  in the field, practical concerns such as sampling frequency, signal bandwidth, scattering, and noise begin to affect the accuracy of the indicator. This chapter treats these issues mostly computationally, but they resemble experimental issues.

### 3.1 Case Study: Sawtooth Waveform

As described in Section 1.2.1, sine waves deform nonlinearly and approach the shape of a sawtooth wave before decaying. Since a sawtooth wave contains an instantaneous shock, it is essentially an ideal nonlinear waveform to study. The sawtooth waveform is the subject of study in this section. This analysis was prompted from the findings in Section 2.1, which showed that  $v_N$  converged to the same value for all harmonics. This convergence occurred only as the waveform became a sawtooth. It was then questioned whether or not the value of  $v_N$  for a sawtooth waveform could be analytically determined.

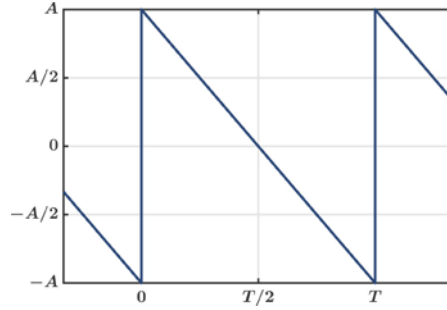


Figure 3.1. Example sawtooth waveform that is under study in this section.

Consider a sawtooth wave of amplitude  $A$ , period  $T$ , and fundamental frequency  $f_0$  (i.e.,  $T = 1/f_0$ ). Such a sawtooth wave is shown in Fig. 3.1. This is inverted from the usual definition of a sawtooth wave because shocks physically form from bottom to top. The Fourier series representation of this waveform is

$$x(t) = A \sum_{n=1}^{\infty} \frac{2}{n\pi} \sin(2\pi n f_0 t) , \quad (3.1)$$

or in standard notation the series is given by

$$x(t) = \frac{a_0}{2} + \sum_{n=1}^{\infty} a_n \cos(2\pi n f_0 t) + b_n \sin(2\pi n f_0 t) , \quad (3.2)$$

$$a_0 = a_n = 0 ,$$

$$b_n = \frac{2A}{n\pi} .$$

Written as a series of complex exponentials, the same series is written as

$$x(t) = \sum_{n=-\infty}^{\infty} c_n e^{2\pi i n f_0 t} , \quad (3.3)$$

$$c_n = \begin{cases} 0 , & n = 0 \\ \frac{iA}{n\pi} , & n \neq 0 \end{cases} .$$

The next step is to compute  $Q/S$  for this waveform as given by Eq. (1.5). This is done through use of the convolution theorem:

$$\mathcal{F}^*\{x(t)\}\mathcal{F}\{x^2(t)\} = X^*(X \otimes X) , \quad (3.4)$$

where  $X$  represents the Fourier transform of  $x(t)$ . The convolution in Eq. (3.4) is calculated by

$$X^*(X \otimes X) = c_n^* \sum_{p=-\infty}^{\infty} c_p c_{n-p} , \quad (3.5)$$

and

$$\sum_{p=-\infty}^{\infty} c_p c_{n-p} = \begin{cases} \frac{A^2}{3} , & n = 0 \\ \frac{2A^2}{n^2\pi^2} , & n \neq 0 \end{cases} . \quad (3.6)$$

Consequently,  $Q/S = 0$  for  $n = 0$  since  $c_n^* = 0$ . For  $n \neq 0$ ,

$$Q_{pp^2} = \text{Im} \left\{ c_n^* \sum_{p=-\infty}^{\infty} c_p c_{n-p} \right\} = \text{Im} \left\{ \frac{iA}{n\pi} \frac{2A^2}{n^2\pi^2} \right\} = \frac{2A^3}{n^3\pi^3} . \quad (3.7)$$

The calculation of  $S_{pp}$  and  $p_{\text{rms}}$ , follows as

$$S_{pp} = c_n c_n^* = \frac{A^2}{n^2\pi^2} , \quad (3.8)$$

$$p_{\text{rms}} = \sqrt{\frac{1}{2} \sum_{n=1}^{\infty} b_n^2} = \frac{A}{\sqrt{3}} .$$

Combining these together gives

$$\frac{Q}{S} = \frac{Q_{pp^2}}{p_{\text{rms}} S_{pp}} = \frac{2\sqrt{3}}{n\pi} . \quad (3.9)$$

Next, Eq. (1.8) gives

$$v_N = -10 \log_{10}(e) \times \frac{\omega\beta p_{\text{rms}} Q}{\rho_0 c_0^3 S} = -40 \log_{10}(e) \times \frac{A f_0 \beta}{\rho_0 c_0^3} . \quad (3.10)$$

Eq. (3.10) gives an analytical expression for the value of  $v_N$  for a sawtooth waveform. Note that  $v_N$  is not dependent on harmonic number,  $n$ , but is constant across frequency. It is only dependent

on the initial amplitude, fundamental frequency, and medium parameters. With the relation that  $\rho_0 c_0^2 = \gamma P$ , where  $\gamma$  is the ratio of specific heats and  $P$  is the ambient pressure, along with  $\beta = (\gamma + 1)/2$  for an ideal gas, Eq. (3.10) can be recast as

$$v_N = -20 \log_{10}(e) \times \frac{A f_0 (\gamma + 1)}{\gamma c_0 P} . \quad (3.11)$$

The expressions for  $v_N$  in Eqs. (3.10) and (3.11) will be used in the rest of this chapter as benchmarks.

## 3.2 Effect of Sampling Frequency: Sawtooth

In practice, calculating  $v_N$  from finitely sampled waveforms does not yield the exact values from Eqs. (3.10) and (3.11) at all frequencies. Instead, the error varies as a function of many different parameters; the effect of sampling frequency on the error is explored in this section for three different varieties of sawtooth waveforms.

### 3.2.1 Ideal Sawtooth Waveform

As a mathematical example, consider an ideal sawtooth wave similar to that in Fig. 3.1, with amplitude  $A = 1$  Pa and frequency  $f_0 = 1$  Hz. Absorption is ignored, so the low frequency is unimportant. For air with  $\beta = 1.2$ ,  $\rho_0 = 1.20$  kg/m<sup>3</sup>, and  $c_0 = 343$  m/s, Eq. (3.10) gives  $v_N \approx -4.30 \times 10^{-7}$  dB/m. However, calculating  $v_N$  directly from the waveform results in errors at high frequencies. Figure 3.2 shows (a) the calculated  $v_N$  and (b) error from the analytical value for different sampling rates. The calculation of  $v_N$  is done by using one full period of the waveform with no windowing. The value of  $v_N$  is zero for frequencies other than integer multiples of the fundamental, but since exactly one period of the waveform is used with no

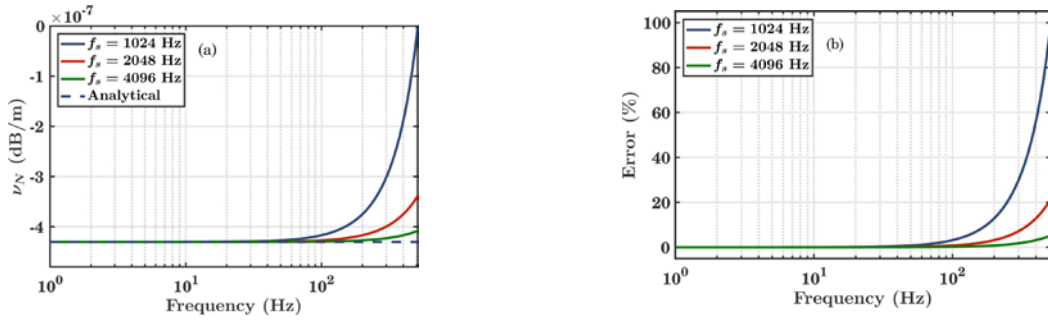


Figure 3.2. (a) Calculations of  $v_N$  for an ideal sawtooth waveform sampled at various rates. (b) The error in  $v_N$  compared to the analytic value. A 20% error occurs at about one-quarter the sampling frequency.

windowing in the calculation, only integer multiples of the fundamental frequency are included in the frequency array of the Fourier transform. Part (a) is plotted up to 512 Hz on the x axis, which is the Nyquist frequency for the first case shown in blue. The other curves show that the accuracy is better at 512 Hz when the waveform is sampled at higher frequencies. Part (b) shows the percent error, with 20% error occurring at about one-quarter the Nyquist frequency for each curve.

The source of this error is revealed by examining the power spectral density (PSD) of each waveform. Because the sawtooth contains an infinite number of frequencies, there is a wrap-around error in the PSDs due to a finite sampling rate. The wrap-around error is evident in Fig. 3.3, which shows the PSDs of both the sawtooth waveform and the waveform squared. The colors correspond to the same sampling frequencies as in Fig 3.2. The PSD of the waveform

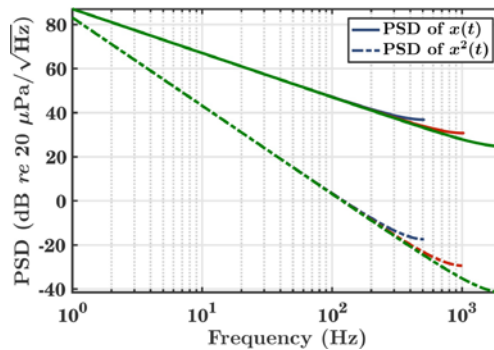


Figure 3.3. PSD of the sawtooth waveform and the waveform squared. The cross-spectrum between these two values is used to calculate  $Q/S$ . Errors due to aliasing can be seen in both quantities. The blue, red, and green curves are sampled at 1024, 2048, and 4096 Hz, respectively.

squared is included because  $Q/S$  is calculated from the cross-spectral density of the Fourier transform of the waveform and waveform squared. As expected from Eq. (3.1), the PSD is a straight line that is inversely proportional to frequency. However, near the Nyquist frequency for each case, an increase of a few decibels is observed due to the wrap-around error. The same error is observed in the PSD of the waveform squared and occurs near the Nyquist frequency. These errors combine to cause the error in  $\nu_N$  near the Nyquist frequency.

### 3.2.2 Bandlimited Sawtooth Waveforms

The ideal sawtooth waveform plotted in Fig. 3.1 is not measurable in practical applications, because it requires an infinite bandwidth to adequately capture the discontinuity. When taking measurements in the field, bandwidth limitations cause the series in Eq. (3.1) to be truncated. In effect, a limited bandwidth translates to the presence of Gibbs phenomenon, or oscillations around the shock discontinuity. However, these small oscillations translate to a huge error in  $\nu_N$ . To demonstrate, the same calculations used to make Figs. 3.2 and 3.3 were done for a sawtooth with a truncated instead of infinite series as in Eq. (3.1). Figs. 3.4 (a) and (b) show the  $\nu_N$  values and error from the analytical value, respectively. Instead of a 20% error at one-quarter

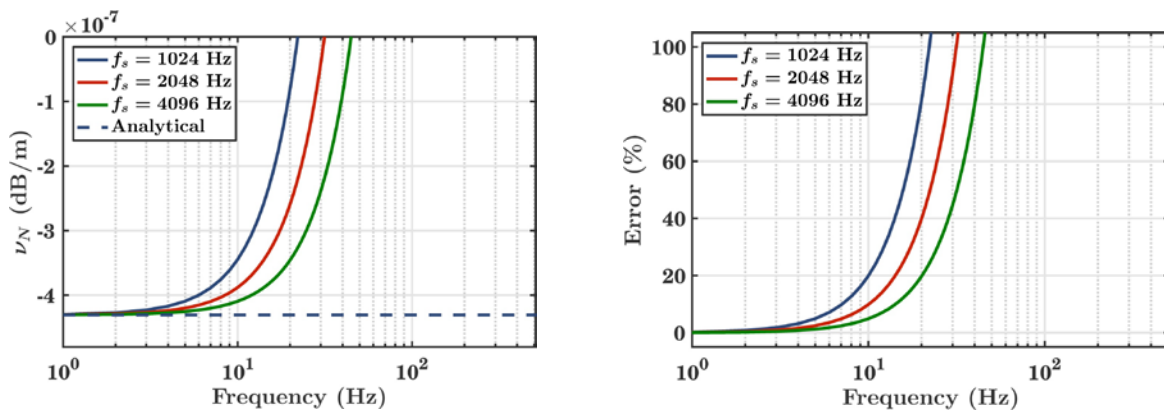


Figure 3.4. (a) Calculations of  $\nu_N$  for a sawtooth waveform calculated from a truncated Fourier series for various sample rates. (b) The error in  $\nu_N$  compared to the analytic value. A 20% error occurs at about one-hundredth the sampling frequency, much lower than for the ideal sawtooth

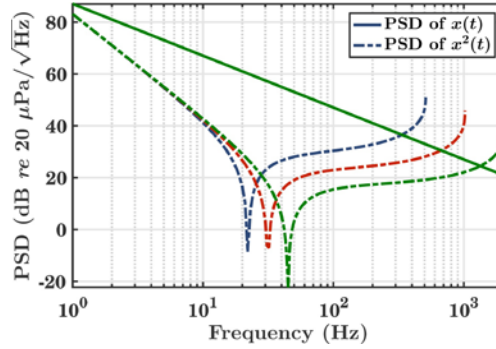


Figure 3.5. PSD of the waveform and the waveform squared for a sawtooth calculated from a truncated Fourier series. The sampling rates for each color line are as in Fig. 3.4. There is no aliasing error because the series is truncated. The error for the PSD of  $x^2(t)$  is very large.

the sampling frequency, this error occurs at one-hundredth the sampling frequency. In Fig. 3.5, the PSD of the waveform is completely flat due to the truncated series. It is in effect like a perfect brick-wall filter with no aliasing. However, for some reason the PSD of the squared waveform contains large errors at low frequencies.

The cause of this error is somehow inherent in the truncated series sawtooth waveform. The error could possibly be attributed to a natural effect in a bandlimited system measuring a sawtooth waveform. Perhaps the error from each of these tests results from the fact that Eq. (1.5) relies on the expectation of a random process, and the sawtooth waveform used in this section is deterministic. In an attempt to make the signal less deterministic, the phase of the waveform was randomized in each block of the PSD calculation. However, since  $Q_{pp^2}$  depends on the phase difference between the waveform and squared waveform, and the phase randomization affected both waveforms, the calculated  $v_N$  value was exactly the same. Future work is to explore alternate methods of calculating  $Q_{pp^2}$ , such as integrating the bispectrum, which do not require taking the cross-spectral density between the pressure and pressure squared waveforms.

In practice, an anti-aliasing filter is used instead of a hypothetical brick-wall filter to remove the spectral content higher than the Nyquist frequency, and these filters have some kind

of roll-off. This can be simulated computationally by using a Butterworth filter on an ideal sawtooth waveform. This has been done, and the  $v_N$  values and errors, along with the PSDs, look similar to those in Figs. 3.4 and 3.5. The main difference is that the PSDs of both the waveform and squared waveform roll off at the higher frequencies, but the errors occur at about the same frequencies.

### 3.2.3 Experimental Sawtooth Waveform

To confirm the numerical results, a National Instruments PXI DAQ was used to measure the voltage output of a function generator creating a sawtooth waveform. The function generator used was an Agilent 33220A with 20 MHz resolution. The sampling frequency of the PXI 4462 card was set at 204.8 kHz. The sawtooth waveform had an amplitude of 1 V and a fundamental

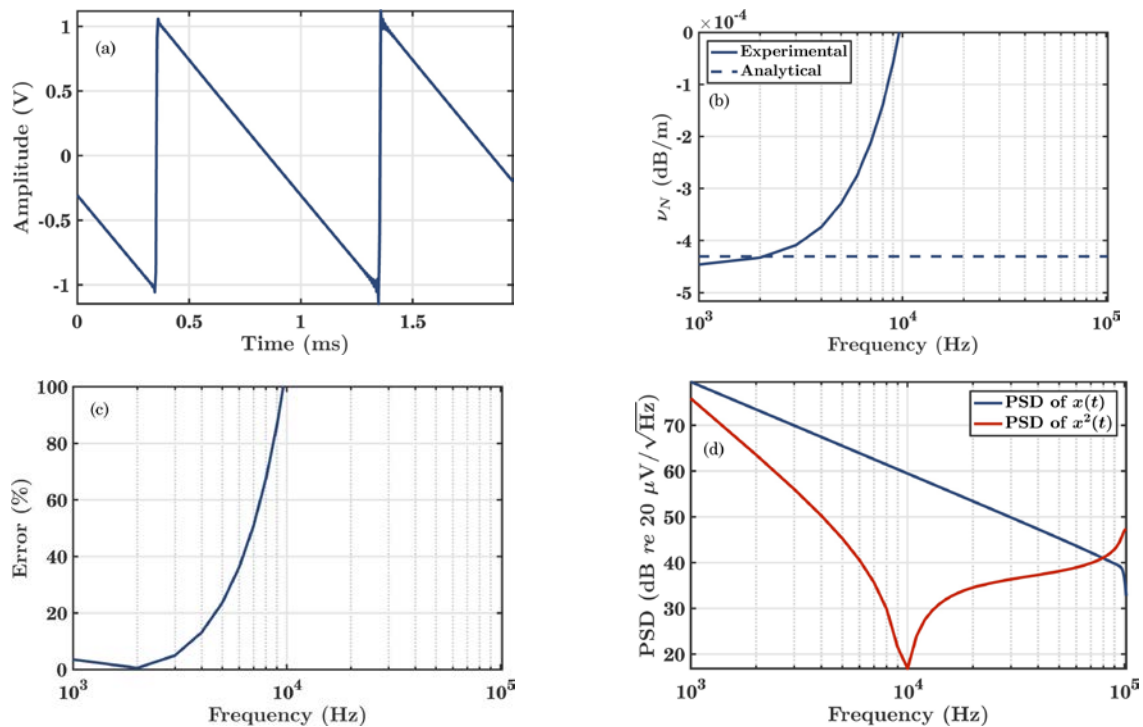


Figure 3.6. (a) Experimentally measured sawtooth waveform. (b) Calculated value of  $v_N$ . (c) Error from the expected analytic value. A 20% error occurs at about 2% the sampling frequency. (d) PSD of the waveform and waveform squared. Note the sharp rolloff in the waveform PSD and the large error in the waveform squared PSD.

frequency of 1 kHz. The sawtooth and corresponding calculations from the waveform are shown in Fig. 3.6. The calculations were done as if the wave had an amplitude of 1 Pa. The error in the PSD of the squared waveform is similar to that of the truncated Fourier series waveform and results in the error in  $v_N$  as well. This is seen in parts (b)-(d). The error reaches 20% at a frequency of about 2% the sampling frequency.

One important takeaway from the experimental results is that having a non-integer number of samples per period does not fix the issues seen in either Section 3.2.1 or Section 3.2.2. The indicator values for the computational sawtooth waveforms were calculated from exactly one period of the waveform that was periodic in the window. Any error that may have been a product of these exact conditions would have disappeared from the experimental data. The error seen in Fig. 3.6 must therefore be a result of the direct calculation of  $v_N$  from a bandlimited sawtooth waveform.

### 3.2.4 Mendousse Solution Revisited

The error in  $v_N$  appears to be large for a sawtooth waveform, but what about waveforms that are shock-like but do not have a perfect sawtooth shape? Due to thermoviscous absorption, the Mendousse solution preserves a finite shock thickness, as exhibited in nature. An important point regarding sampling rate limitations is illustrated by examining the accuracy of  $v_N$  at various stages of the solution. For a Gol'dberg number of  $\Gamma = 30$ , the waveform shapes are shown for various values of the normalized distance,  $\sigma$ , in Fig. 3.7 (a). Part (b) shows the PSD amplitudes of the same waveforms. Part (c) shows the percent error in  $v_N$  calculated for each waveform, where the actual change in level was calculated by taking numerical derivatives of the spectra

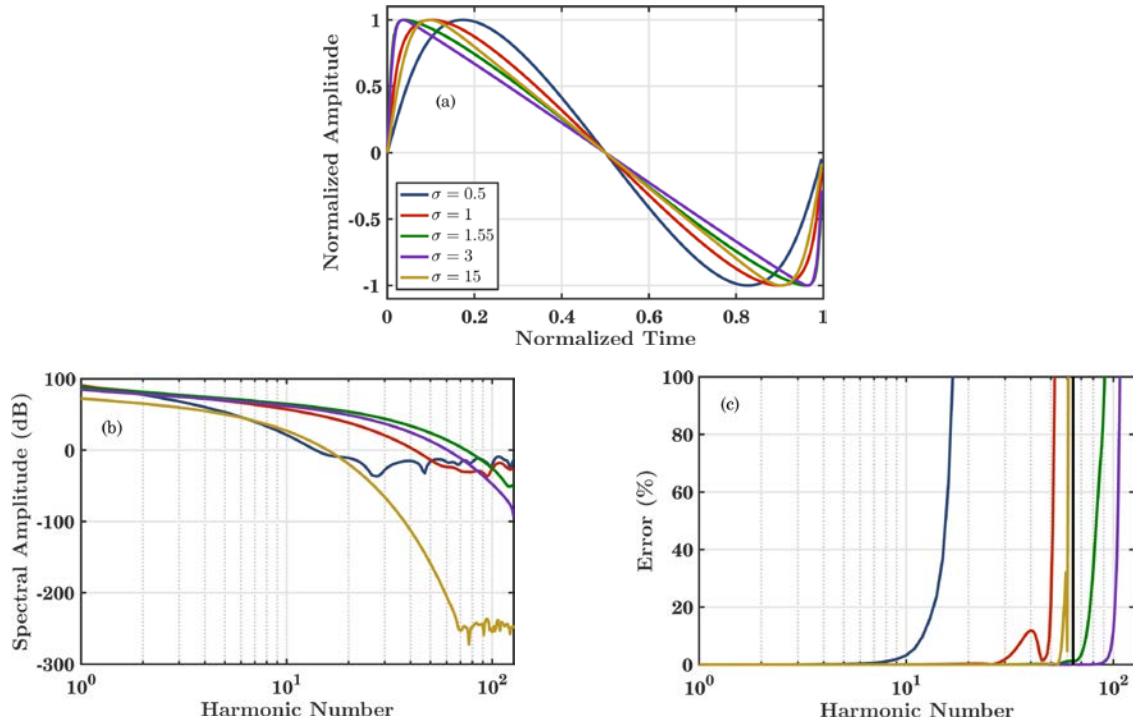


Figure 3.7. (a) Mendousse solution waveforms at various normalized distances with  $\Gamma = 30$ . (b) Spectral amplitudes of the waveforms. (c) Percent error in the  $v_N$  indicator. The vertical black line is at one-quarter the sampling frequency. The legend in part (a) applies to parts (b) and (c) as well.

with a step size of  $\Delta\sigma = 0.05$ . The black vertical line is located at one-quarter the sampling frequency, which for this example was taken to be 256 times the fundamental frequency.

The frequencies at which the curves exceed 20% error in part (c), in order of increasing distance, are 5.1%, 16.8%, 28.9%, 40.2%, and 22.7% the sampling frequency. The PSDs in Fig. 3.7 (b) do not have large amounts of energy out to the Nyquist frequency—they begin to roll off faster than a power-law slope due to absorption—which appears to increase the effective bandwidth of the  $v_N$  calculation. Comparing the curves in parts (b) and (c) reveals that the error in  $v_N$  for most of the curves occurs near where the PSDs deviate from their smooth behavior due to numerical round-off error. The round-off error is introduced at different frequencies for each waveform because of the complicated nature of the solution in Eq. (2.7). In other words, the accuracy of  $v_N$  may be even better with increased numerical precision. The accuracy of  $v_N$  is

better for the analytical Mendousse solution than for any other waveform, indicating the accuracy may depend on waveform type.

### 3.3 Effect of Sampling Frequency: Bandwidth

The error in the sawtooth waveforms from Section 3.2 is very large, and one might wonder how  $v_N$  could be useful at all. This section shows that the error magnitude of the indicator depends on the bandwidth of the signal under analysis. In fact, some types of waveforms show little to no error below one-quarter of the sampling frequency, suggesting they behave as ideal cases.

#### 3.3.1 Narrowband Gaussian Noise

To illustrate the effect of increased bandwidth on the behavior of  $v_N$ , an example of narrowband noise is performed computationally. To compare with the data presented in Chapter 4, some experimental conditions were copied from the model-scale jet noise tests. Consider an ideal monopole source of radius 4 cm (called  $1 D_j$ ), radiating narrowband Gaussian noise with a root-mean-square amplitude of 22 kPa. The source radiates spherically, and the atmospheric conditions are as follows: temperature is 22.9°C, ambient pressure is 0.956 atm, and relative humidity is 53.3%. The Gaussian noise is centered spectrally at 1 kHz, with 3-dB down points at 973 and 1030 Hz. In addition, the noise was filtered to have a power-law decay for high frequencies, as seen from the curve at  $1 D_j$  in Fig. 3.8 (d). The signal was propagated out to  $1000 D_j$ , and the resulting waveform, along with the linear approximation and original waveform (amplitude compensated for with geometric spreading), is plotted in Fig. 3.8 (a). The output waveform closely resembles a sawtooth waveform.

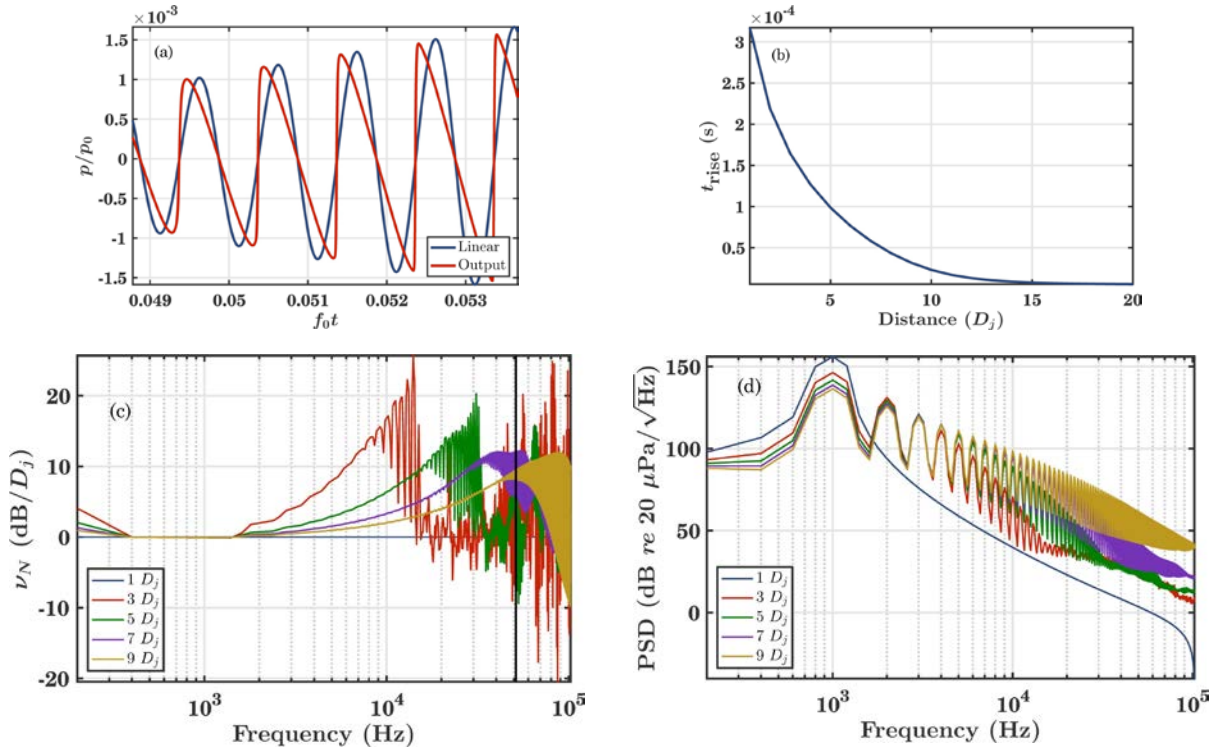


Figure 3.8. (a) Comparison of the linear (spreading and absorption), and output (including nonlinearity) waveforms. (b) Shock rise time of the largest shock in the waveform. The waveform quickly shocks up over a short distance. (c) The  $v_N$  values for various distances. The  $v_N$  curve at  $1 D_j$  is zero everywhere. The vertical black line marks one-quarter the sampling frequency. (d) PSD at various distances. The initial spectrum at  $1 D_j$  has a power-law decay in the high frequencies. Note the waveform becomes more broadband due to nonlinear harmonic generation.

Shocks develop in the waveform quickly, as demonstrated by the shock rise time<sup>36</sup> in part (b). Part (c) shows the  $v_N$  spectral values from  $1 D_j$  to  $9 D_j$  at intervals of  $2 D_j$ . (The  $v_N$  values at  $1 D_j$  are zero.) A vertical black line marks one-quarter the sampling frequency. Note the large initial growth in the 10-kHz range as the shocks first begin to form. At  $3 D_j$ , the  $v_N$  values are very noisy above 15 kHz due to the very small amplitude of the PSD. As the waveform propagates farther, the noisy oscillations diminish and the curves become smoother. However, the smoothness does not necessarily imply accuracy. Figure 3.9 shows  $v_S$ ,  $v_a$ ,  $v_N$ , their sum, and the actual numerical derivative for six different harmonics of the waveform. The term “harmonic” is used loosely here, since the initial signal is of finite bandwidth. The agreement between  $v$  and  $\Delta L/\Delta D_j$  can be seen to worsen slightly as harmonic number increases. From

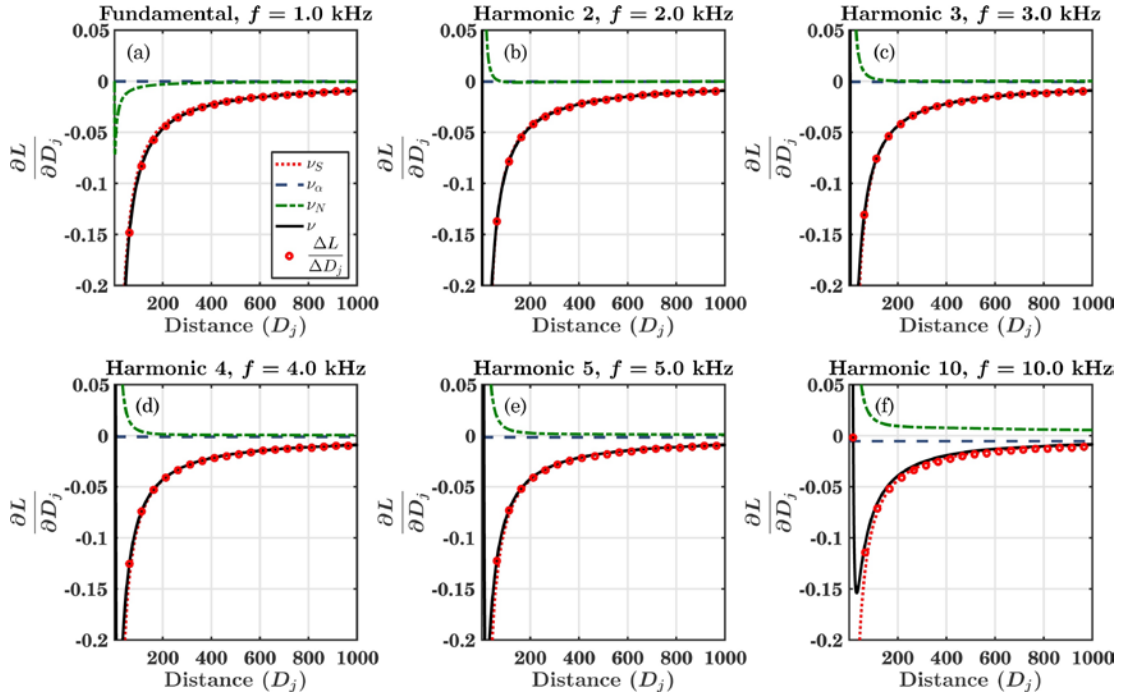


Figure 3.9. Values of  $\nu_S$ ,  $\nu_\alpha$ ,  $\nu_N$ , their sum ( $\nu$ ), and the actual numerical derivative ( $\Delta L/\Delta D_j$ ) for six different harmonics of narrowband Gaussian noise. The fundamental frequency is defined as the center frequency of the lowest noise band. The agreement between the prediction and the numerical derivative worsens with harmonic number.

part (f), at  $965 D_j$  the error between the  $\nu$  prediction and the actual numerical derivative,  $\Delta L/\Delta D_j$ , for 10 kHz is 19.6%. However, the nature of the error in  $\nu_N$  depends on the waveform shape. Figure 3.10 shows (a) the PSDs and (b) the percent error in  $\nu_N$  calculated at various distances. In the far field ( $1000 D_j$ ), the 20% error occurs at only 5% the sampling frequency, less than the expected one-quarter the sampling frequency for the exact sawtooth waveform (see Fig. 3.2). At the other distances reported—except for  $25 D_j$ —the accuracy of  $\nu_N$  is good to much higher frequencies. Note that the initially large errors around 300 and 400 Hz for the red and blue curves are due to the large changes that are happening very quickly at those frequencies. The error is only large because the step size in distance is not large enough. Figure 3.10 seems to imply a similar result as Fig. 3.7: the accuracy of  $\nu_N$  depends on the waveform shape and type, and it seems to perform better in the pre-shock region.

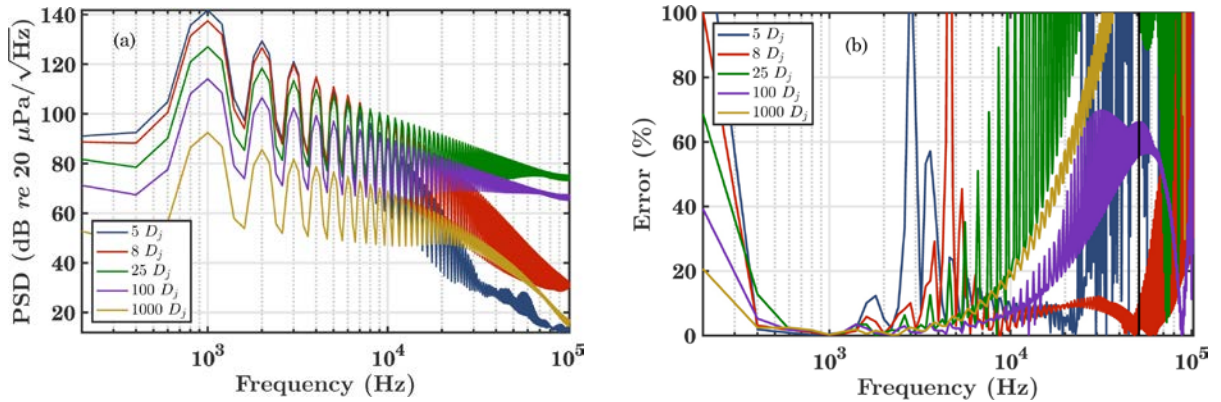


Figure 3.10. (a) PSDs of the computationally propagated narrowband Gaussian noise at various distances. (b) Percent error in  $v_N$  for the same distances. At  $1000 D_j$ , a 20% error occurs at about 5% the sampling frequency.

The narrowband noise error in the far field is less than the error for the bandlimited sawtooth waveform, where 20% error occurs at just 1% the sampling frequency (see Fig. 3.4). The improvement in the narrowband Gaussian noise is likely due to two factors: one, the final waveform is not an exact sawtooth because it has been smoothed out by absorption, and two, the signal is initially narrowband instead of monofrequency. However, the simulation from Section 2.3, similar to that given above but starting with a sinusoid waveform rather than narrowband Gaussian noise, shows the improvement is largely due to bandwidth. In the sinusoid simulation, the >20% error occurs at only 0.3% the sampling frequency. Thus it appears that  $v_N$  calculations for narrowband signals are valid to much higher frequencies than for initially monofrequency signals.

In part (d) of Fig. 3.8, the initial spectrum rolloff can be seen from the curve at  $1 D_j$ . In addition, the troughs in the PSD begin to decrease in depth as the waveform propagates. This is because of nonlinear harmonic generation, but also because the bandwidth of each harmonic increases with frequency.<sup>37</sup> However, as opposed to the monofrequency sawtooth wave, sum-and-difference harmonic generation occurs for all frequencies present in this signal. Nonlinear generation then occurs for many more frequencies in the upper-frequency range. With sufficient

propagation and harmonic generation, essentially all frequencies will eventually be nonlinearly generated if the waveform is of sufficient amplitude. The evolved PSD is approaching a smooth  $1/f^2$  power-law spectral slope typical of jet noise. Comparing parts (c) and (d) of Fig. 3.8,  $v_N$  begins to increase for the  $3 D_j$  curve just as the PSD for the same distance begins to deviate from the power-law spectral slope. This indicates the nonlinear behavior of going from sine wave to sawtooth, which exhibits the same power-law spectral slope.

### 3.3.2 Experimental Broadband Noise

The ability of  $v_N$  to quantify the rate of nonlinear waveform steepening is further improved when the noise is broadband instead of narrowband. The example from this section is

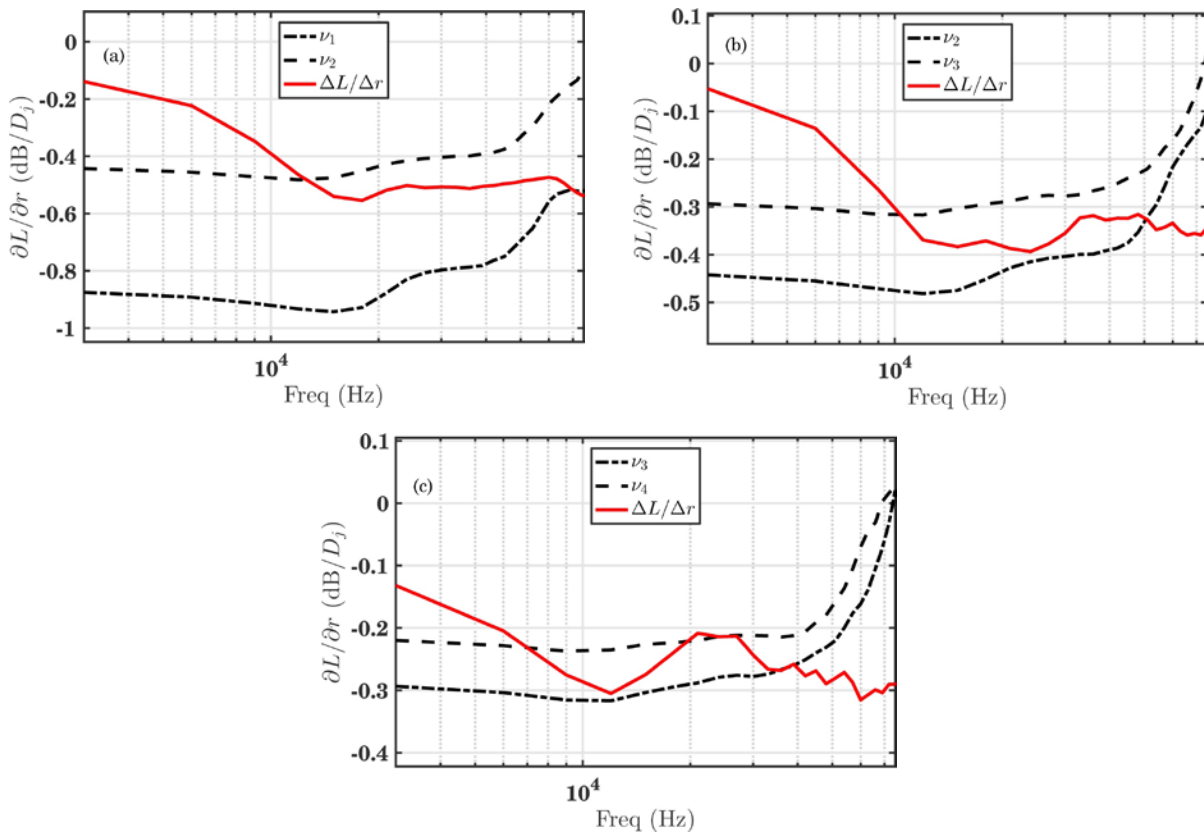


Figure 3.11. Predicted change in sound pressure level— $v$ , or the sum  $v_S + v_\alpha + v_N$ —with numerical derivatives of the PSD levels between microphones. The derivatives are taken between (a) microphones 1 and 2, (b) microphones 2 and 3, and (c) microphones 3 and 4.

drawn from experimental data reported in Sections 4.1 and 4.2 rather than simulation because of better accuracy. The noise was measured from a Mach-2.0 model-scale jet with diameter 3.5 cm ( $1 D_j$ ). The data was sampled at 192 kHz along a radial with the first four microphones spaced  $10 D_j$  apart. Figure 3.11 compares the predicted change in sound pressure level— $\nu$ , or the sum  $\nu_S + \nu_\alpha + \nu_N$ —with numerical spatial derivatives of the PSD levels between microphones. The derivative,  $\Delta L/\Delta r$ , found in part (a) is a centered-difference between microphones 1 and 2. The  $\nu_N$  values are shown for microphones 1 and 2 as well. Part (b) shows a derivative between microphones 2 and 3, part (c) between microphones 3 and 4. Since the  $\nu$  values are instantaneous derivatives and the numerical derivative is centered between the microphones, the  $\Delta L/\Delta r$  curve is expected to lie somewhere between the two  $\nu$  curves.

The error in the low frequencies of each part of Fig. 3.11 is due to the frequency-dependent directivity of the source.<sup>16, 38</sup> There are changes in the frequency content simply due to directivity, not nonlinearity, that are not predicted by the  $\nu$  metrics. In addition, spherical spreading is assumed for the  $\nu_S$  metric, which may or may not be accurate for measurements near a model-scale jet. However, from about 10 kHz to 50 kHz the agreement is good. A sharp increase in the  $\nu$  curves is seen around 40 kHz, which is 21% the sampling frequency. Besides this sharp increase, the predictions seem to follow the actual derivatives fairly well. For certain, the agreement between  $\nu_N$  and measured values is good above 5% the sampling frequency, or about 10 kHz.

Another indication of the reliability of  $\nu_N$  when working with experimental data is found in the PSD of the square of the waveform. Examples from Section 3.2 show significant errors in the PSD of the waveform squared. However, the PSDs of various model-scale jet noise waveforms reported in Section 4.1 are shown along with the PSDs of those waveforms squared

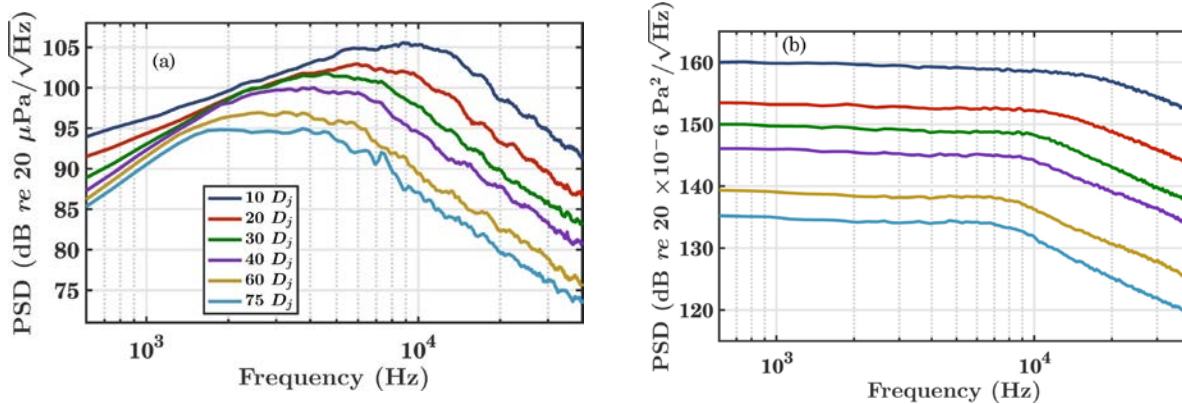


Figure 3.12. (a) PSDs of model-scale jet noise waveforms. (b) PSDs of the same model-scale jet noise waveforms squared. The PSDs of the waveforms squared exhibit a smooth behavior.

in Fig. 3.12. There is no indication of large errors in the PSDs of the squared waveforms, which gives further confidence as to the reliability of the  $v_N$  indicator for broadband data. Experimental broadband data such as that examined in this section is currently the best confirmation for the use of  $v_N$  as a nonlinearity indicator.

### 3.3.3 Broadband Noise from the Literature

As a further examination of the effect of the sampling frequency on broadband noise, other papers which use the Morfey-Howell indicator,  $Q/S$ , and which report results for noise data are examined for probable errors heretofore undetected. McNerny *et al.*<sup>21</sup> give  $Q/S$  values for high-intensity rocket noise sampled at 48 kHz. For example, parts (c)-(e) of Fig. 12 show a steady upward slope in the magnitude of  $Q/S$  from about 10 to 20 kHz. This type of increase is expected since in the far field nonlinearity increases with frequency to slow absorption. However, there is an even steeper increase in  $Q/S$  starting at about 20 kHz, followed by a sharp decrease down to zero due to the rolloff in the spectra. It is likely that the second increase and subsequent decrease are due to bandwidth limitations of the Morfey-Howell indicator. It is difficult to know whether or not the steady upward slope beginning at 10 kHz is due to error, but

the increase with frequency is expected in the far field. Regardless, the data appears to behave well up to about one-quarter the sampling frequency. Similar behavior is seen in Fig. 13 of Ref. [21], but the data are shown only up to 20 kHz instead of 24 kHz. Parts (b) and (d) of Fig. 13 show the steady upward slope in  $Q/S$ , but there appears to be no secondary sharp increase; the absence of a sharp increase implies accurate values for the indicator up to at least one-quarter the sampling frequency for this case.

McInerny *et al.*<sup>39</sup> give  $Q/S$  values for aircraft flyover data sampled at 96 kHz. The spectra in Ref. [39] appear to roll off significantly due to absorption beginning around 5 kHz. Figures 12-15 show increasing  $Q/S$  values up to about 12 kHz, where the curves kink and the values suddenly begin to decrease in magnitude. It is likely that the initial increase shows the accurate slowing of absorption due to nonlinear growth, but the final decrease could either be a product of the low sound pressure levels measured at high frequencies or a product of limitations in the indicator. However, it is difficult to know whether or not the increasing  $Q/S$  values are reliable without performing spatial derivatives on data from multiple microphones as a verification. Similarly, Downing *et al.*<sup>40</sup> give  $Q/S$  values for the Concorde, Boeing 727 and Boeing 757 aircrafts sampled near 45 kHz. Figures 1 and 2 show an increase in the magnitude of  $Q/S$  up to about 10 kHz, followed by a sudden decrease in magnitude to zero. Though not completely clear, the initial increase appears to be accurate, and the sudden decrease seems to be from limitations inherent in the indicator; the steep decrease begins almost right at one-quarter the sampling frequency. The  $Q/S$  values shown in Fig. 3 are very noisy and imply little nonlinearity in the signal, but the magnitude of the noise increases distinctly above 10 kHz. The increased noise at high frequencies adds credibility to the idea that the decreasing  $Q/S$  magnitudes above 10 kHz in Figs. 1 and 2 are erroneous.

Petitjean *et al.*<sup>7</sup> sampled high-speed jet noise near 180 kHz or higher and report  $Q/S$  values in Figs. 15 and 16 up to about 50 kHz. These findings show no sign of the errors investigated in this section. The curves are relatively smooth and show transition of energy from low to high frequencies. Gee *et al.*<sup>41</sup> sample noise from supersonic jets at 298.5 kHz and show  $Q/S$  values up to 100 kHz. In Fig. 2 there is evidence of a slight decrease in the  $Q/S$  magnitude beginning around 70 kHz, close to one-quarter the sampling frequency. Finally, Gee *et al.*<sup>42</sup> report high-performance jet aircraft noise sampled at 44.1 kHz. They give  $Q/S$  values up to just under one-quarter the sampling frequency. A sharp transition from increasing to decreasing  $Q/S$  magnitude is visible in Fig. 6 at about 8 kHz, while the increase becomes steeper in Fig. 7 around the same frequency. It is unclear whether or not these effects are due to bandwidth limitations of the Morfey-Howell indicator.

In summary, the vast majority of papers reporting  $Q/S$  values do not exhibit the large errors observed in the sawtooth and narrowband noise observed in Sections 3.2 and 3.3. Errors do seem to occur for frequencies above one-quarter the sampling rate, but this is as expected from the ideal sawtooth in Section 3.2.1. Of course, the examination of the literature here is mostly qualitative, and a quantitative analysis of the data from the papers would be necessary to confirm the accuracy of  $Q/S$  for each case. However, a viable conclusion is that the Morfey-Howell indicator—and by connection  $v_N$ —is much more accurate for experimentally measured broadband noise than for either simulated noise or sawtooth waveforms.

Future work to provide further understanding of the accuracy of the  $v_N$  indicator requires a controlled environment where high-amplitude signals of several varieties can be tested and physically propagated. This could be done in a plane-wave tube experiment. However, past experiments have shown that even small discontinuities in the tube can cause scattering and

ringing in the waveform,<sup>15, 43, 44</sup> so care must be taken to ensure a proper experiment. A high-amplitude sinusoid could be propagated such that it deforms into a sawtooth waveform, and  $v_N$  could be calculated on the waveform to search for errors similar to those found in Section 3.2. Similarly, narrowband and broadband data could be propagated to more systematically determine the effect of bandwidth on the accuracy of  $v_N$ . Studies of this type could give more conclusive evidence as to why the indicator seems to behave so much better for experimental broadband data than for monofrequency tones or computationally propagated waveforms.

### 3.4 Effect of Scattering and Measurement Noise

#### 3.4.1 Effect of Scattering

Because the  $v_N$  indicator is so sensitive to errors at high frequencies, scattering can create large issues in its accuracy. For example, some measurements from the F-35 reported in Chapter 5 were taken with relatively large microphone holders that caused scattering. Measurements from one microphone in particular showed oscillations of about  $\pm 2$  dB in the PSDs from 2 to 20 kHz. Figure 3.13 shows the one-third-octave band (a) PSD and (b)  $v_N$

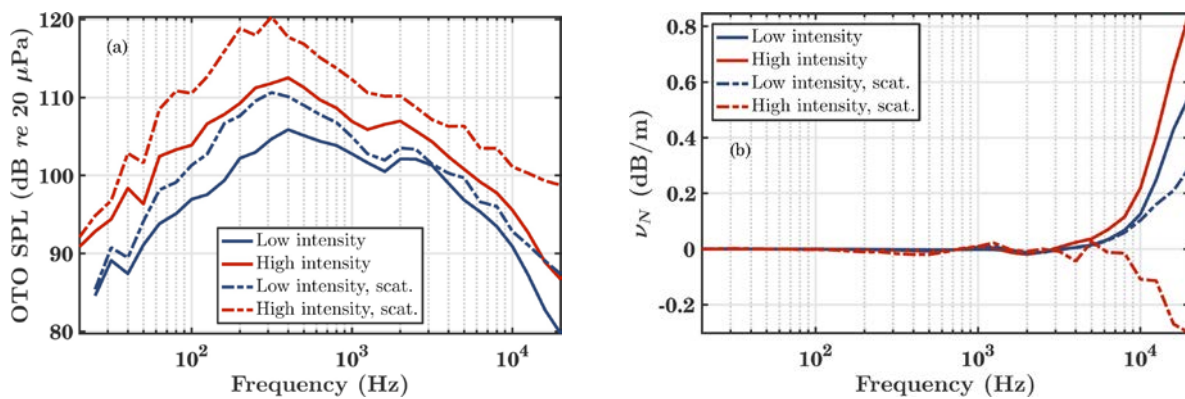


Figure 3.13. One-third-octave (OTO) band (a) SPL and (b)  $v_N$  values for F-35 noise data at two different power levels and with and without scattering. The scattering most adversely affects  $v_N$  for the high-intensity noise.

calculations for a clean measurement and one with scattering at two different power levels. The clean and scattered measurements were taken at the same distance and just  $10^\circ$  apart; the difference between these measurements was due to variation of microphone placement in their holders during experimental setup.

The high-power condition with scattering has nearly completely corrupted the  $v_N$  values. The narrowband calculations, not shown here, exhibited variations in  $v_N$  of over 200% the uncorrupted values. However, the low-power condition with scattering shows  $v_N$  values similar to those computed from the data without scattering up to about 10 kHz. It is unclear why  $v_N$  is corrupted by scattering for one measurement (high intensity) and not for another (low intensity). Care must be taken to ensure that scattering effects do not invalidate the  $v_N$  metric. Ground reflections also pose an issue for  $v_N$  and  $Q/S$ ,<sup>42</sup> as discussed and illustrated in Sections 5.2 and 5.3.1.

### **3.4.2 Effect of Measurement Noise**

General measurement noise also causes problems for  $v_N$  calculations. This is in part because the noise is increased when the waveform is squared in the  $Q/S$  calculation. This is evident in Fig. 3.14, which shows  $v_N$  calculations for an ideal sawtooth waveform with added noise at a signal-to-noise ratio (SNR) of 60, 80, and 100 dB. The sampling frequency was 1024 Hz. Parts (a) and (b) show that for an SNR of 60 dB, the indicator is valid only up to about 6% the sampling frequency. While this is much worse than the ideal case with no noise, the adverse effect is much less important than a bandlimited system (compare Fig. 3.4). Perhaps for this reason, measurements with an SNR of 60 dB can still be used for  $v_N$  calculations. Part (c) of Fig. 3.14 shows that the added noise is emphasized in the PSD of the waveform squared, which

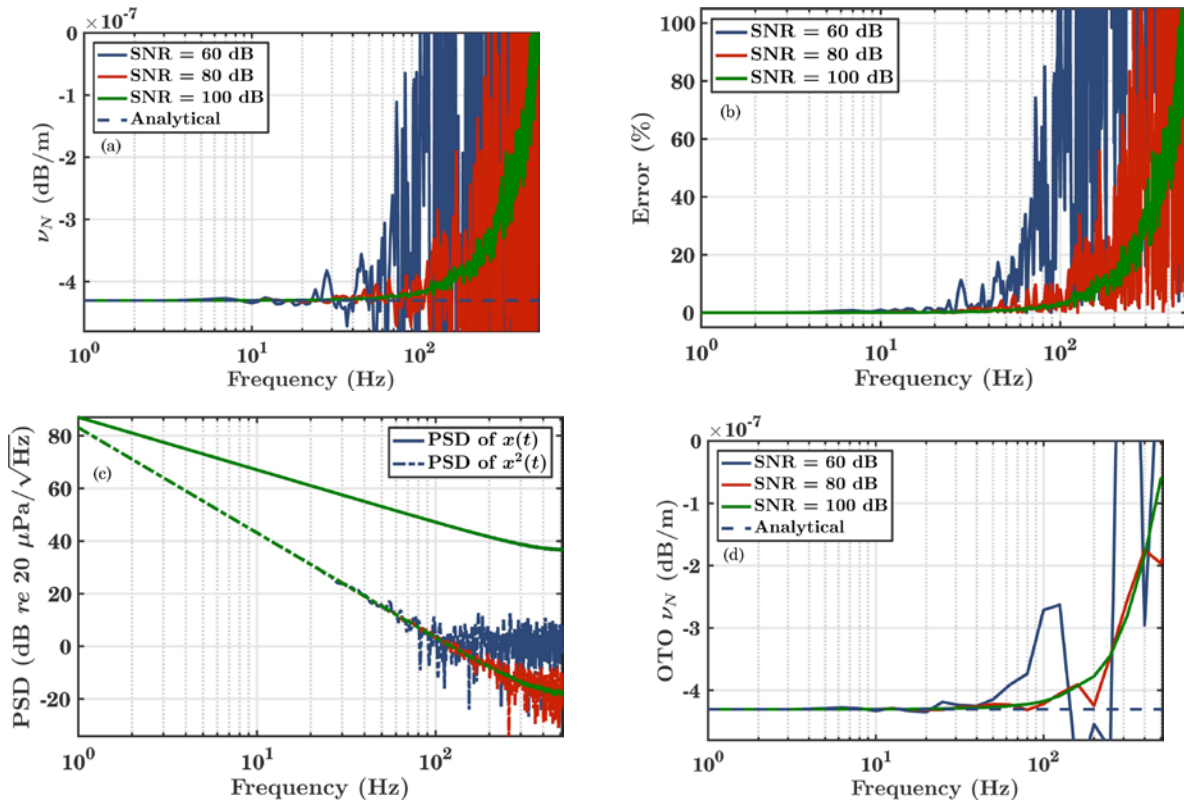


Figure 3.14. (a) Values of  $\nu_N$  for an ideal sawtooth waveform with added noise. (b) Error compared to the analytical value for the same. (c) PSD of the waveform and waveform squared. The noise more adversely affects the waveform squared PSD than the waveform PSD, creating the error. (d) OTO band averages of  $\nu_N$  from part (a). The noise does not produce much effect for 80 and 100 dB SNR.

is what causes such a large error in the  $\nu_N$  values. In part (d), a one-third-octave band calculation of  $\nu_N$  is used, and the values are much more accurate. See Appendix A for information on calculating  $\nu_N$  for one-third-octave bands.

### 3.5 Summary and Experimental Recommendations

This section summarizes the findings and advises on experimental conditions necessary to use the  $\nu_N$  indicator (and by extension the Morfey-Howell,  $Q/S$  indicator). The frequency at which the error in  $\nu_N$  is greater than 20%, given in percentage of the sampling frequency ( $f_s$ ), is listed in Table 3.1 for the separate cases studied in Sections 2.3, 3.2, and 3.3. The accuracy is best for analytical or infinite-bandwidth signals. The next best signal is experimentally measured

Table 3.1. Frequency ratio at which  $v_N$  exhibits greater than 20% error for various cases.

Case	Frequency with 20% error in $v_N$ (% of $f/f_s$ )
Mendousse solution at $\sigma = 3$	40%
Ideal sawtooth with finite sampling rate	24%
Experimental model-scale jet data	21%
Computationally propagated narrowband Gaussian noise in the far field	5%
Experimentally generated sawtooth	2%
Computationally filtered sawtooth	1%
Computationally propagated sinusoid	0.3%

broadband noise, for which the  $v_N$  predictions appear to agree with the measured spatial derivatives for frequencies up to 21% of the sampling frequency. Next best is computationally propagated narrowband noise. Bandlimited measurements of a sawtooth waveform (experimental then computational) and a computationally propagated sinusoid give the worst agreement. Overall, noise with some finite bandwidth tends to give better accuracy than non-ideal, bandlimited sawtooth waves. Based on Table 3.1, under ideal conditions the maximum frequency up to which data should be trusted is 24%, or about one-quarter of the sampling frequency. This frequency limit also makes intuitive sense, since squaring a waveform to calculate  $Q_{pp^2}$  introduces sum-and-difference frequencies, including a component at double that of each original frequency. Because of the Nyquist limit, the doubled components will only be accurately represented for original frequencies up to half the Nyquist frequency, or one-quarter the sampling frequency.

The restriction to one-quarter of the sampling frequency seems to be due to a limitation inherent either in the indicator itself or in the method of calculating  $v_N$ . In an ideal measurement with an infinite-bandwidth signal, aliasing errors in the waveform and squared waveform spectra for a fully developed weak shock (sawtooth waveform) cause the error. If the measurement is bandlimited, the error is exacerbated for both a brick-wall filter and a more traditional anti-

aliasing filter. Likely errors above one-quarter the sampling frequency are seen in several papers reporting  $Q/S$  measurements. However, the maximum reliable frequency for  $Q/S$  and  $v_N$  seems to be much higher for experimental broadband noise signals than for a bandlimited sawtooth waveform or computationally propagated noise. In fact, in the jet- and rocket-noise literature, the expected smooth behavior is largely observed below one-quarter the sampling frequency. The experimental broadband signals appear to behave nearly like an ideal sawtooth waveform.

Both scattering and measurement noise can be large sources of error when using the  $v_N$  indicator. Since the indicator is proportional to frequency (see Eq. [1.8]), even small variations at high frequencies can disrupt the indicator values dramatically. In addition, the effect of measurement noise increases when the waveform is squared, further disrupting the indicator values. The effect of scattering on the indicator seems to depend on the nature of the source (bandwidth, amplitude, etc.). Judgment should be made on a case-by-case basis as to the impact of scattering when calculating  $v_N$ . However, the adverse effects of scattering and measurement noise seem to be overall less important than those of a finite sampling frequency and a finite-bandwidth signal.

Overall, the  $v_N$  indicator seems to work best for experimentally measured broadband signals, but the sampling frequency should be made as large as possible to ensure measurement reliability. In experiment,  $Q/S$  and  $v_N$  values should not be taken as accurate above one-quarter the sampling frequency. Measurements can be made along a propagation radial with relatively small spacing to ensure that the spatial derivatives predicted by  $v_N$  match the actual derivatives in the data, as done in Section 3.3.2 (Fig. 3.11). Perhaps verification of  $v_N$  on a case-by-case basis is necessary until further experiments can be conducted with a spatial grid of microphones to better determine its accuracy for experimental noise.

# Chapter 4

## Nonlinearity Analysis of Model-Scale Jet Data

Despite the issues discussed in Chapter 3, the  $v_W$  indicator seems to perform well for analyzing broadband jet noise data.<sup>35</sup> Prior to treating jet-noise from a full-scale military aircraft in Chapter 5, this chapter deals with noise from a model-scale jet. It is devoted to analysis of the experimental data taken, along with comparison between engine conditions. Results are not reported above one-quarter the sampling frequency. Parts of the analysis refer to Section 2.3, which contains a computational analysis of a monopole emitting a sinusoidal signal with conditions similar to those in which the jet noise data were taken. This entire chapter is modeled after Ref. [35], and the same dataset has been analyzed previously using other nonlinearity indicators.<sup>5, 16, 45</sup>

### 4.1 Spectral Analysis for Mach 2.0

Unheated laboratory-scale jet noise data were collected in an anechoic chamber on jets of nozzle diameter 3.5 cm. Jet conditions were varied between subsonic Mach 0.85, overexpanded Mach 1.8, and ideally expanded Mach 2.0. The analyses in Sections 4.1 and 4.2 treat the Mach-2.0 case and Section 4.3 treats the other two. Waveforms sampled at 192 kHz were

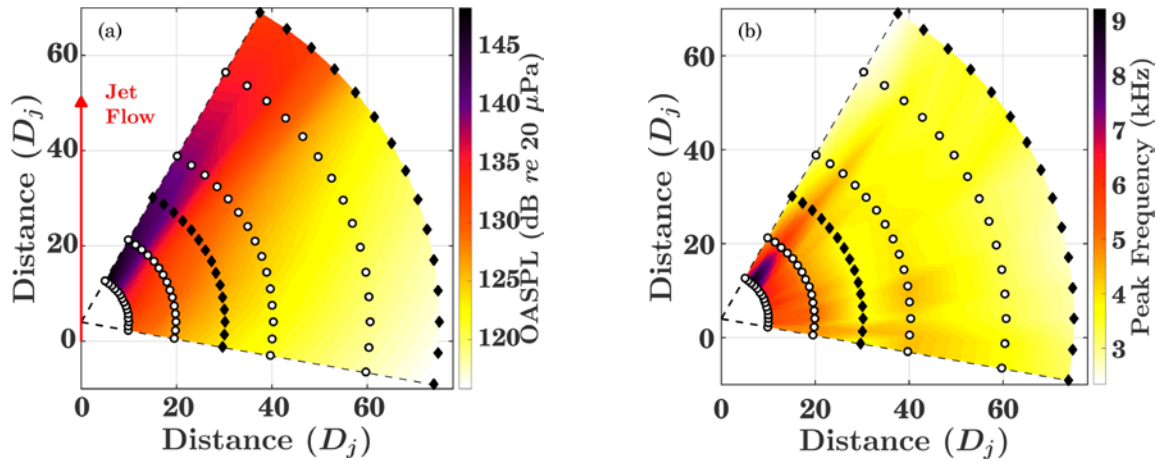


Figure 4.1. Plots for the Mach-2.0 model-scale jet noise data. (a) Overall sound pressure level (OASPL) for the microphone array. Circles represent 3.18-mm microphones and filled diamonds represent 6.35-mm microphones. (b) Peak frequency map.

acquired at distances between 10-75 jet nozzle diameters ( $D_j$ ) and along radials from  $80^\circ$  to  $150^\circ$  in  $5^\circ$  increments (relative to upstream axis). Six microphones with diameters of 3.18 mm and 6.35 mm were mounted in an array whose origin was located  $4 D_j$  downstream of the nozzle exit. This origin is upstream from the expected overall noise source region,<sup>38</sup> but facility configuration constraints required this positioning.

The overall sound pressure level (OASPL) for the Mach-2.0 case is shown in Fig. 4.1 (a), along with an arrow indicating the direction of jet flow. Note the primary radiation lobe along the  $145^\circ$  radial, which is one line of microphones in from the top-most edge. In this figure, circles represent 3.18-mm microphones and filled diamonds represent 6.35-mm microphones. The OASPL is large enough that nonlinear behavior is to be expected near the principal lobe.<sup>5, 16,</sup>  
<sup>45</sup> In part (b), the peak frequency at each microphone is displayed. The peak frequency was calculated by finding the geometric mean of the frequency range 3 dB down from the spectrum maximum. Note that the line of microphones along the  $150^\circ$  radial (closest to the jet plume) has a predominantly lower peak frequency than the surrounding microphones. This is due to the directivity of the jet, with lower frequencies being projected at steeper angles from the nozzle

head. In addition, very close to the source, a few microphones have a very high peak frequency.

These locations are in the near field, so their spectra are relatively flat with a high peak

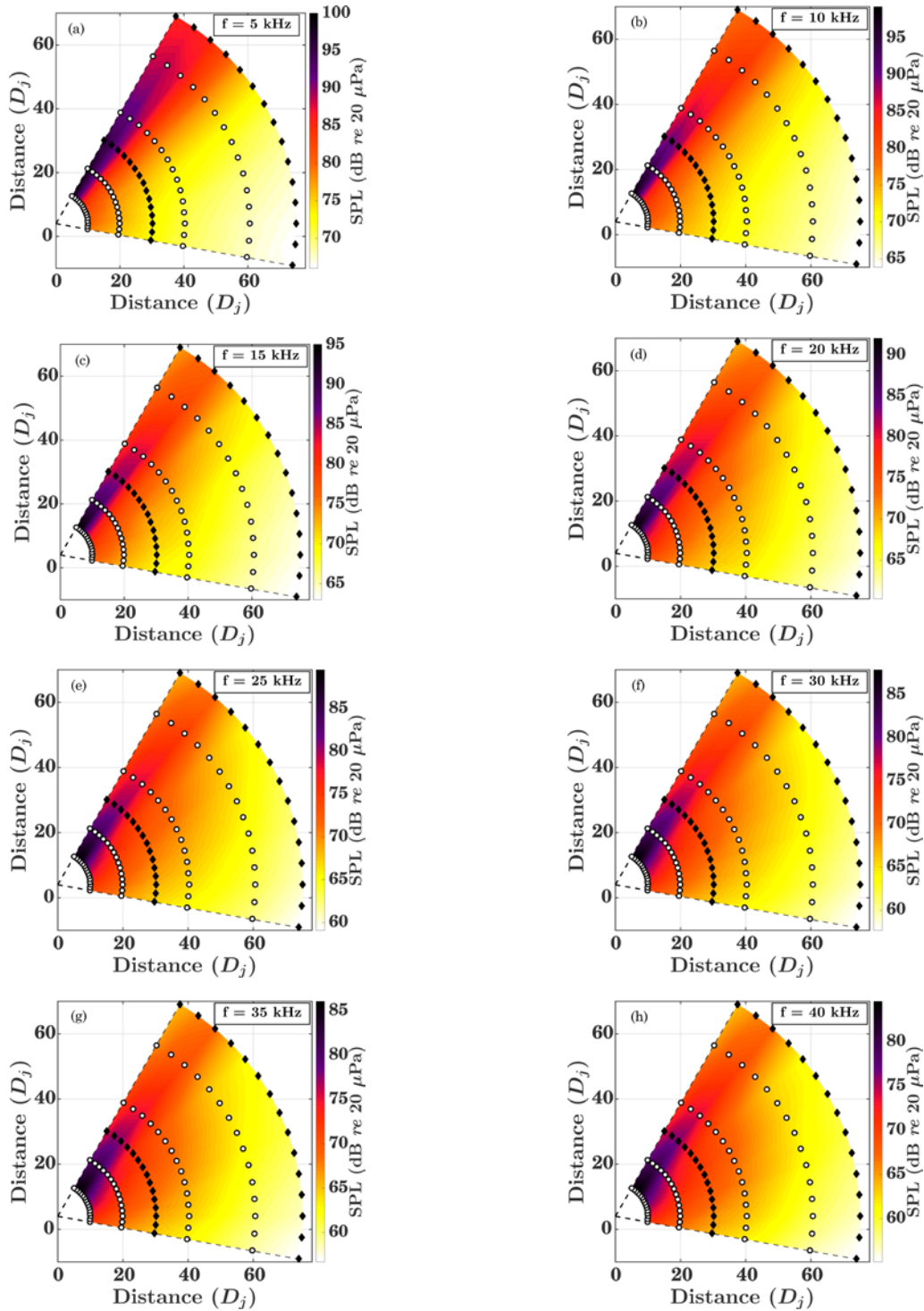


Figure 4.2. Sound pressure level maps for eight different frequencies at Mach 2.0. Note that the angle of radiation decreases (moves farther from the jet plume) with frequency.

frequency. Figure 4.2 shows the sound pressure level (SPL) for eight individual frequencies. Here a slight change in directivity is visible for each frequency, with the higher frequencies radiating at shallower upstream angles (farther away from the jet flow). This correlates well with the peak frequency plot in Fig. 4.1 (b).

Characteristics of the source can be observed through examination of the power spectral densities (PSDs). Figure 4.3 (a) shows the measured PSDs along the 145° radial as a function of distance. This radial is at the maximum far-field radiation angle. A shift in peak frequency is observed along the radial from 10 to 60  $D_j$ , due to those microphones being in the geometric near field of a source with frequency-dependent source location, directivity, and spreading rate.<sup>46</sup> It is important to note that this downward shift in peak frequency is not related to nonlinear effects (see discussion regarding Fig. 4 in Ref [46]). For example, low-frequency noise is generated farther downstream from the nozzle than is high-frequency noise,<sup>38</sup> so their propagation radials are different from each other and from the microphone array before converging at  $\sim 60 D_j$ . This is visible in the peak frequency plot and SPL plots in Figs. 4.1 (b) and 4.2, respectively. The high-frequency spectral shapes in Fig. 4.3 (a) reveal nonlinear propagation effects. Between 10-20 kHz the roll-off changes from  $\sim 28$  dB/decade at 10  $D_j$ , the decay rate for large-scale

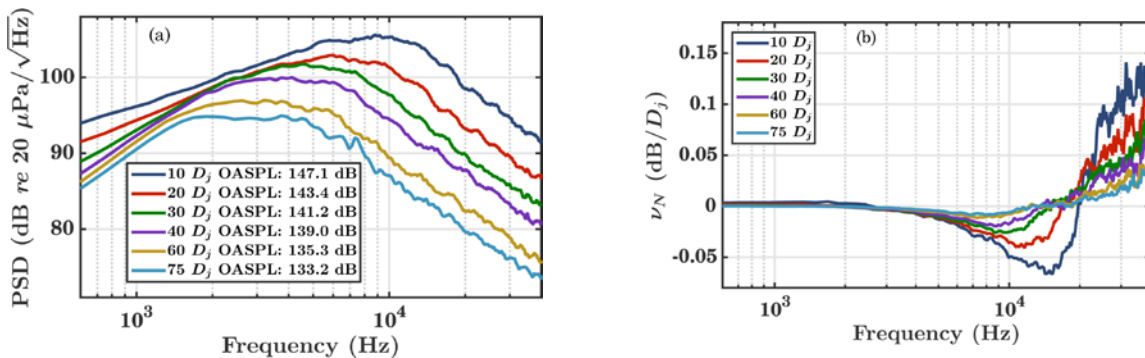


Figure 4.3. (a) PSD for the six microphones along the principal radiation radial for Mach 2.0. Note the decrease in peak frequency along with a relatively constant high-frequency spectrum. (b) The  $\nu_N$  values for the same microphones. The zero-crossing frequency of the indicator decreases with radius, tracking the decrease in peak frequency from part (a).

structure radiation,<sup>47</sup> to  $\sim 20$  dB/decade ( $1/f^2$  spectral slope), typical of shock-containing noise.<sup>48</sup> This spectral shape of the high frequencies remains fairly constant with distance after about  $40 D_j$ , indicating that the energy losses due to absorption and energy gains due to nonlinearity are of similar magnitude. This is explored quantitatively in the next section.

## 4.2 Nonlinearity Analysis at Mach 2.0

Quantitative trends due to nonlinearity are seen by investigation of the  $v_N$  indicator. Figure 4.3 (b) shows  $v_N$  along the same radial as in part (a). Negative and positive values of  $v_N$  indicate loss of energy and gain in energy due to nonlinearity, respectively. The frequency at which the sign of  $v_N$  changes from negative to positive tracks the downward trend in PSD peak frequency with propagation into the far field. The results indicate energy losses from the largest-amplitude region of the spectrum at a given location, with corresponding nonlinear energy gains at higher frequencies, similar to the results from Chapter 2. The overall amplitude of  $v_N$  diminishes with propagation into the far field as well. This is not only because the amplitude of the noise decreases due to geometric spreading, but also because shocks have mostly formed by about  $30 D_j$  (seen in the  $1/f^2$  spectral slope).

Similar to the SPL plots, spatial maps of  $v_N$  are shown in Fig. 4.4. The maps were created using a linear interpolation of the color scheme, and they quantitatively confirm that nonlinear effects are localized at angles near the maximum radiation direction, as indicated by prior analyses.<sup>45, 46, 49</sup> Along the principal radiation lobe ( $145^\circ$ ), the energy loss rate ( $\sim -0.01$  to  $-0.05$  dB/ $D_j$ ) at 10 kHz and gain rate at 40 kHz ( $\sim +0.03$  to  $+0.1$  dB/ $D_j$ ) are very similar in magnitude to the  $v_N$  values shown in Fig. 2.5. Similar to the numerically propagated sine wave in Section 2.3, nonlinearity is more dominant than absorption close to the source, but the two

effects are close to the same strength in the far field. However, Fig. 4.4 (h) shows a small negative region close to the source at about  $130^\circ$ , where energy is still being lost at 40 kHz. The

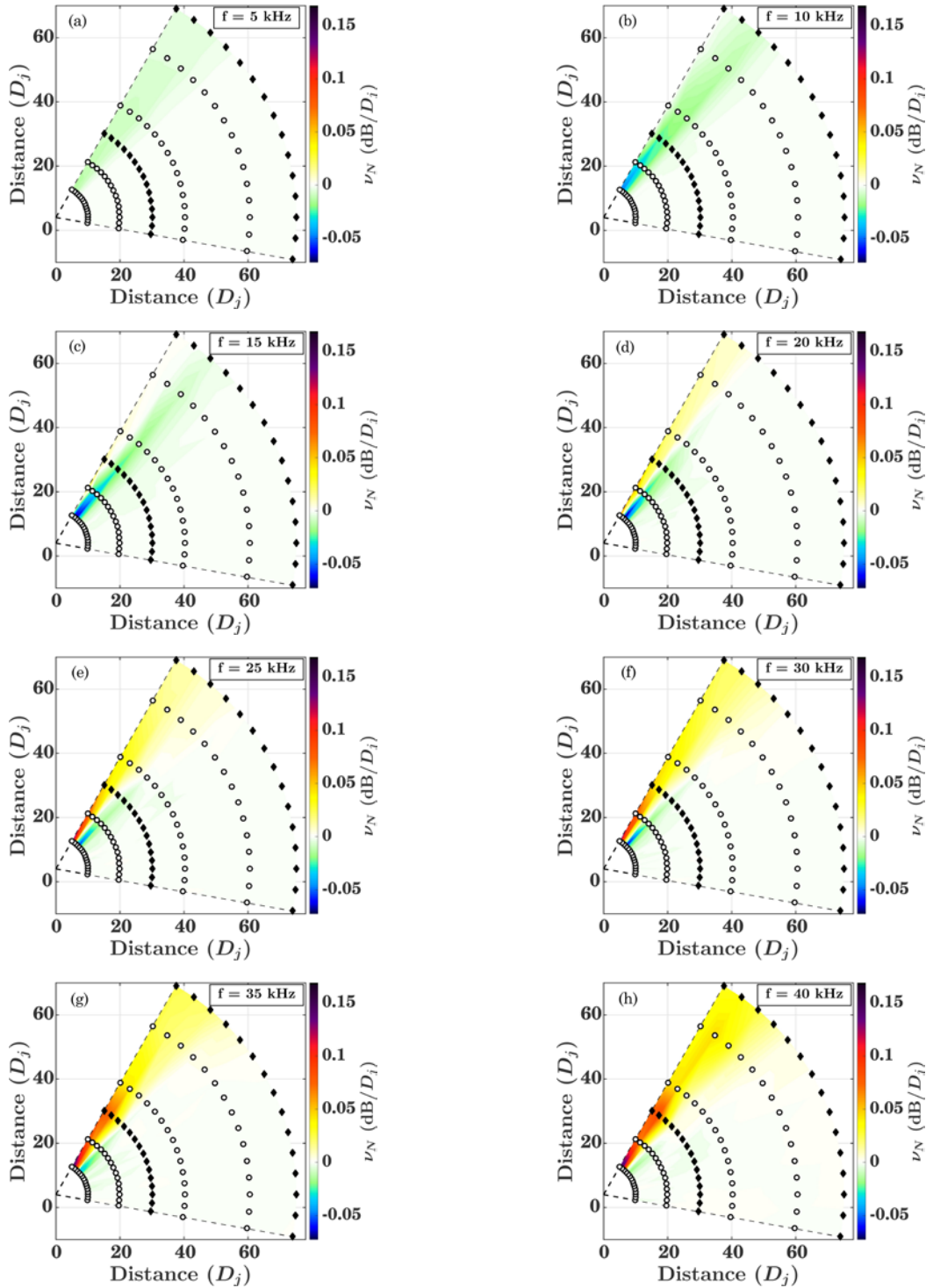


Figure 4.4. Spatial maps of  $\nu_N$  for eight different frequencies at Mach 2.0. The transition to nonlinear loss (driving other harmonics) to nonlinear gain (being nonlinearly driven) can be seen.

peak frequency in this region is about twice that of the principal radiation radial, and energy is being lost at this frequency to generate energy at higher frequencies. At all microphones in the tested region, the change due to spherical spreading is stronger than both nonlinearity and absorption. For comparison, the values for  $\nu_\alpha$  and  $\nu_S$  are given in Fig. 4.5. Absorption gives a change of only  $-0.004 \text{ dB}/D_j$  at 10 kHz and  $-0.05 \text{ dB}/D_j$  at 40 kHz, while spreading gives a change of more than  $-0.1 \text{ dB}/D_j$  everywhere. The atmospheric absorption model used in this chapter and in Chapter 5 is that of Bass *et al.*,<sup>50</sup> which includes both thermoviscous and vibrational relaxation processes.

Based on the argument from Sections 2.2 and 2.3, the nonlinear decay due to absorption of the spectra in the far field should be linear ( $e^{-f}$ ) exponential rather than quadratic ( $e^{-f^2}$ ) exponential. This type of decay is not exactly visible in the PSD in Fig. 4.3 (a) because there has not been sufficient radial propagation. However, the trend towards the expected linear exponential behavior can be seen by examining the sum  $\nu_N + \nu_\alpha$ . This sum essentially gives the modified absorption due to nonlinearity. That sum for all the microphones along the principal radiation radial ( $145^\circ$ ) is given in Fig. 4.6 on (a) linear and (b) logarithmic axes. In addition,  $\nu_\alpha$  (black dash-dotted line) is plotted along with a linear exponential decay (red dashed lined). The  $\nu_\alpha$  curve has the same slope as a quadratic exponential decay from about 4 to 40 kHz, as was

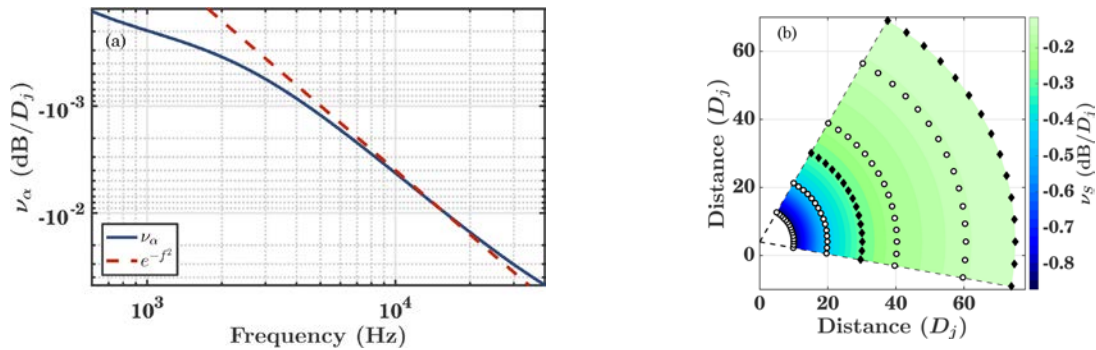


Figure 4.5. (a) Value of  $\nu_\alpha$  (independent of position). The absorption decay closely follows a quadratic exponential decay from about 4 to 40 kHz. (b) Spatial map of  $\nu_S$ . Its values are distinctly larger than either  $\nu_\alpha$  or  $\nu_N$ , showing that spreading is the most dominant effect.

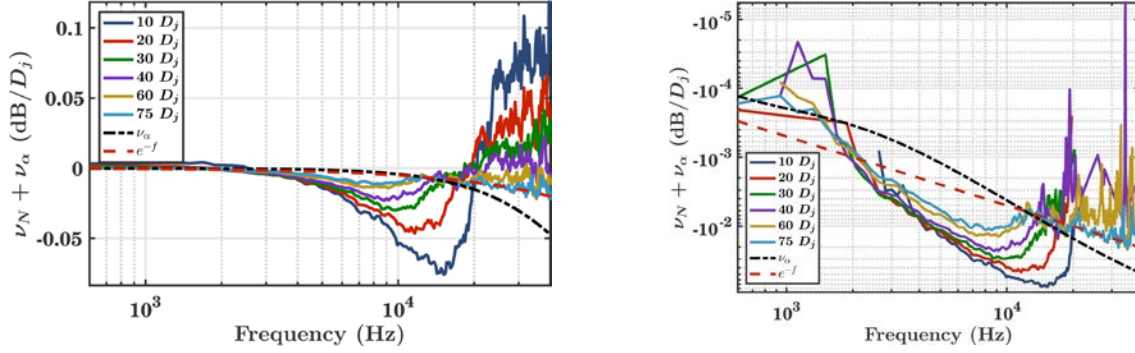


Figure 4.6. (a) Value of the sum  $\nu_N + \nu_\alpha$  along the principal radiation radial ( $145^\circ$ ) for Mach 2.0. Note that in the far field the sum is slightly negative. In addition, the rolloff with frequency is a linear exponential decay. (b) The same plot as (a) but on a logarithmic scale. Only negative values are shown.

seen in Fig. 4.5 (a). The linear exponential curve in Fig. 4.6 fits the decay at  $75 D_j$  almost perfectly, exhibiting the same asymptotic behavior as predicted from Sections 2.2 and 2.3. Fiévet *et al.*<sup>51</sup> report derivative skewness values for a dataset collected from a similar model-scale jet. The derivative skewness values peak at about  $80 D_j$ , indicating the decay of shocks after this distance. The negative values of  $\nu_N + \nu_\alpha$  at  $75 D_j$  correlate well with these derivative skewness values.

### 4.3 Comparison of Jet Conditions

The Mach-2.0 engine condition exhibited the most nonlinearity, but comparison to the other conditions is also valuable. First, the OASPL and peak frequency maps are shown in Fig. 4.7 for Mach 0.85 and 1.8. The levels in part (a) are much lower than for either the Mach-1.8 or Mach-2.0 data, and negligible nonlinearity is expected in the data.<sup>16</sup> Note the secondary radiation lobe occurring in the Mach-1.8 data at about  $125^\circ$ , as seen in part (c). This corresponds to the transition region from low to high peak frequency, as seen in part (d).<sup>5</sup>

Comparing the OASPL maps between the Mach-1.8 and Mach-2.0 data, the Mach-2.0 case only has values 2-4 dB higher than the Mach-1.8 case. The directivity has changed, with the

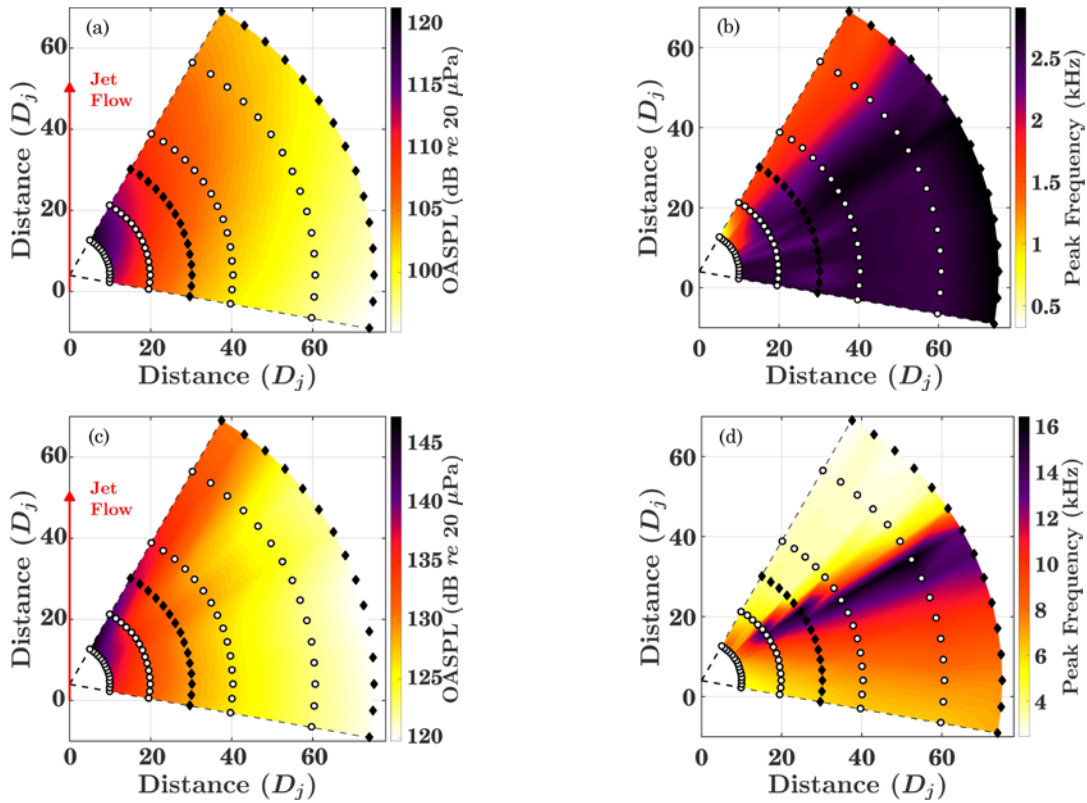


Figure 4.7. (a) OASPL and (b) peak frequency spatial maps for Mach 0.85. (c)-(d) Similar maps for Mach 1.8.

main lobe being located more downstream at Mach 1.8. The  $\nu_N$  values are compared together for the three test cases in Fig. 4.8. As expected, part (a) shows negligible nonlinearity for the Mach-0.85 case. The plot contains only noise, and the small fluctuations in  $\nu_N$  contain no real information. The Mach-1.8 and Mach-2.0 cases in parts (b) and (c), respectively, are plotted with

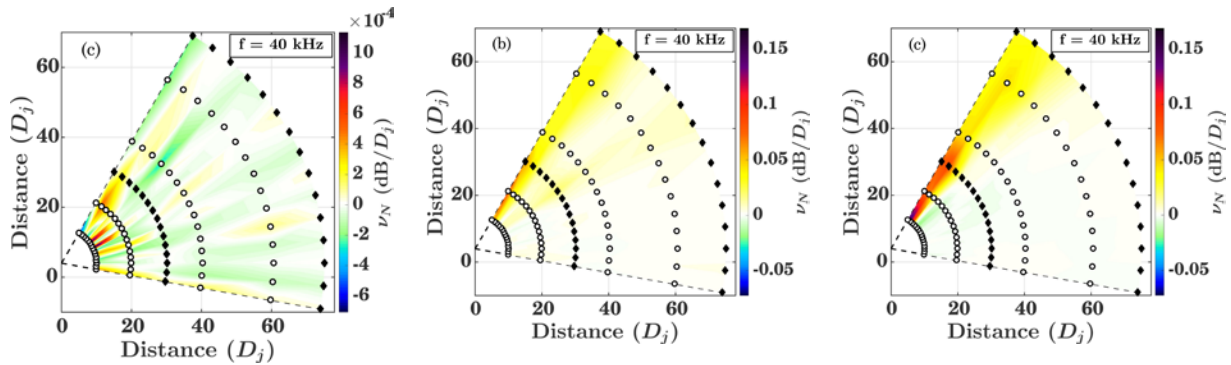


Figure 4.8. The  $\nu_N$  values at 40 kHz for the three engine conditions: (a) subsonic (Mach 0.85), (b) overexpanded (Mach 1.8), and (c) ideally expanded (Mach 2.0). Parts (b) and (c) are plotted on the same scale. The nonlinearity for Mach 2.0 is nearly twice that at Mach 1.8. Part (c) is a copy of Fig. 4.4 (h).

the same color mapping to more directly compare their values. Even though the OASPL levels are only about 3 dB higher (factor of  $\sqrt{2}$ ) at Mach 2.0, the  $\nu_N$  values are nearly twice as large along their respective principal radiation lobes at this frequency. This highlights the nonlinear process occurring, with only a small increase in OASPL causing a large nonlinear generation of high frequencies.

To examine the decay due to nonlinearly adjusted absorption, the same plots are given as in Section 4.2 but for the other engine conditions. The sum  $\nu_N + \nu_\alpha$  is given along with  $\nu_\alpha$  and a linear exponential decay in Figs. 4.9 (a)-(b) for Mach 0.85 and Figs. 4.9 (c)-(d) for Mach 1.8. Each is along the principal radiation radial for that condition:  $150^\circ$  and  $145^\circ$  for Mach 0.85 and Mach 1.8, respectively. For the Mach-0.85 data, there is almost no contribution to the sum from

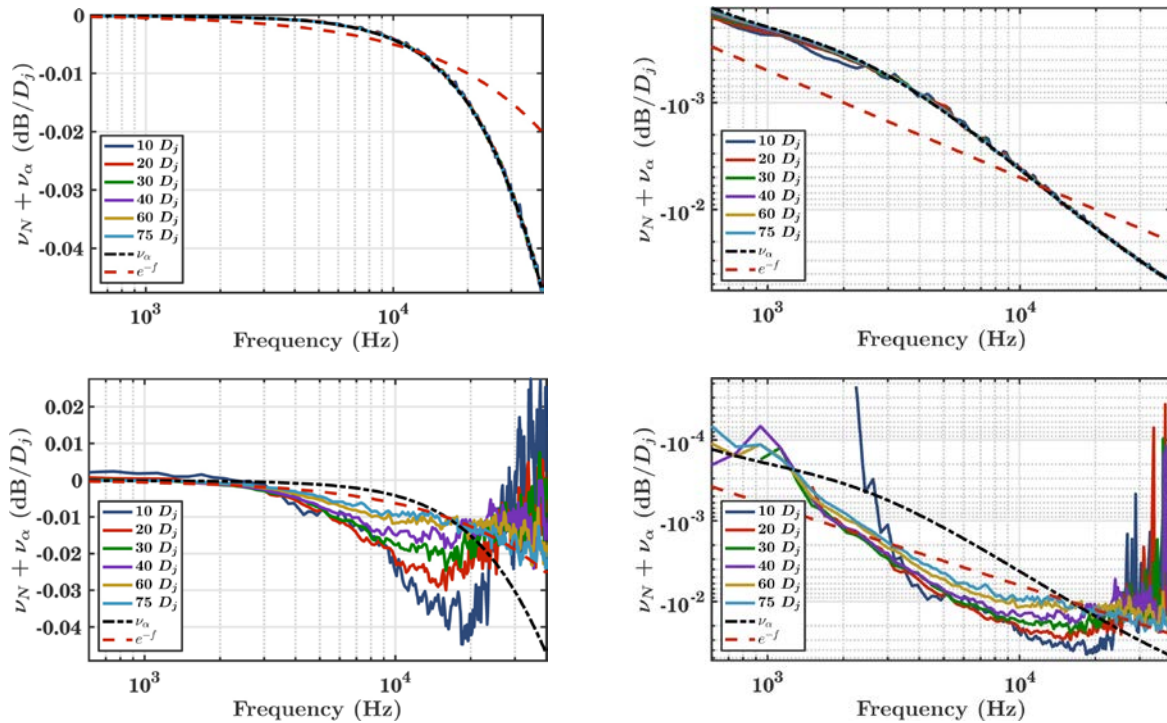


Figure 4.9. The sum  $\nu_N + \nu_\alpha$  on linear and logarithmic scales for (a)-(b) Mach 0.85 along  $150^\circ$  and (c)-(d) Mach 1.8 along  $145^\circ$ , respectively. The contribution due to nonlinearity is essentially zero for (a)-(b), the Mach-0.85 case, and the rolloff goes as absorption only (close to a quadratic exponential decay). For Mach 1.8, or (c)-(d), the rolloff approaches a linear exponential decay, though not as exact as in Fig. 4.6. The linear exponential decay does, however, indicate a reduction in the expected absorption decay due to nonlinearity.

$v_N$ ; the decay is simply according to atmospheric absorption. For the Mach-1.8 data, however, the decay is similar to that of the Mach-2.0 data: a linear exponential decay at 60 and 75  $D_j$ .

### 4.3.1 Summary of Comparisons

As the jet condition increases, the OASPL increases and the directivity of the principal lobe moves upstream. Different from the other conditions, Mach 1.8 shows a secondary radiation lobe in the same region as a sharp increase in peak frequency. The peak frequencies of this condition are nearly twice as large as for Mach 2.0. The OASPL for Mach 0.85 is about 25 dB less than Mach 1.8, which is about 3 dB less than Mach 2.0. The nonlinearity observed from the  $v_N$  indicator is negligible at the lowest condition, and about twice as large at Mach 2.0 compared to Mach 1.8. The sum of the effects of absorption and nonlinearity produce a nearly quadratic ( $e^{-f^2}$ ) exponential decay in the far field at Mach 0.85, but the far-field decay is that of a linear ( $e^{-f}$ ) exponential for Mach 1.8 and Mach 2.0. This shows that nonlinearity is significant enough for these two conditions to change the far-field nature of the waveforms. This confirms the expected results from Section 2.3, namely that a nonlinear waveform experiences a smaller decay in the far field than does a linear waveform.

## Chapter 5

# Quadspectral Analysis of Military Aircraft Jet Noise Data

Military jets pose hearing loss problems for military veterans and aircraft personnel, create annoyance in neighborhoods surrounding airports, and can even cause structural damage. When of sufficient amplitude, the noise from these jets exhibits a characteristic sound known as crackle,<sup>52</sup> a phenomenon closely related to nonlinearity.<sup>53-55</sup> Each of these characteristics contribute to the need to understand the physics behind the noise propagation from these sources and the role of nonlinearity in each. This chapter addresses measurements taken from an F-35A military jet aircraft at Edwards Air Force Base in 2013.<sup>56</sup> These and previously collected F-35 data have been analyzed with nonlinearity indicators such as average steepening factor,<sup>57</sup> derivative skewness,<sup>54, 57</sup> crackle,<sup>54</sup> crest factor,<sup>58</sup> and Gol'dberg number.<sup>59</sup> Here, a nonlinearity analysis using the  $v_N$  indicator is presented.

### 5.1 Experimental Setup

The ground run-up measurements of the F-35A aircraft consisted of 235 unique microphone locations. The 90 locations reported here had radii of 19.1, 28.6, 38.1, 76.2, 152, and 305 m (63, 94, 125, 250, 500, and 1000 ft). The microphone array reference point was located

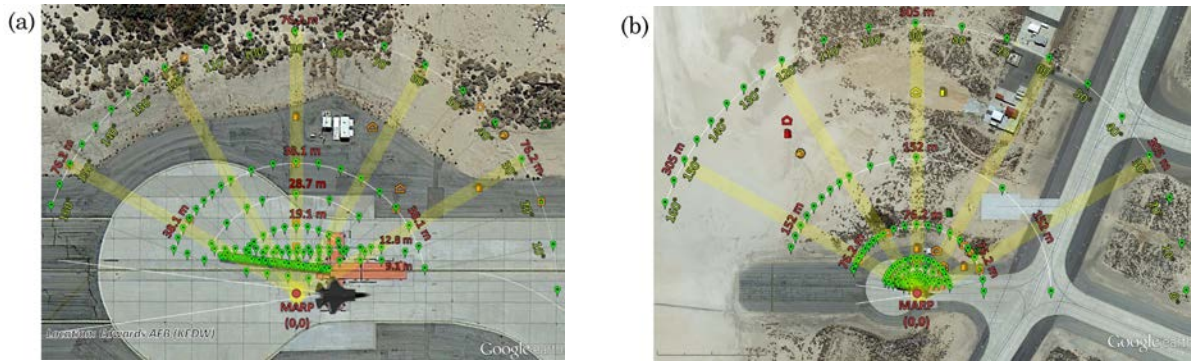


Figure 5.1. Depiction of the experimental setup out to (a) 76.2 m (250 ft) and to (b) 305 m (1000 ft). The microphone array is centered 6.6 m (21.6 ft) behind the aircraft nozzle. Microphone angles ranged from  $0^\circ$  to  $160^\circ$  relative to the engine inlet.

6.6 m (21.6 ft) behind the nozzle of the aircraft. Microphones were located for different angles at each radius, but ranged from  $0^\circ$  to  $160^\circ$  relative to the upstream direction. The heights of the microphones ranged from 1.5 to 9.1 m (5 to 30 ft). The spread of microphones and experiment layout is shown in Fig. 5.1. Data was sampled at 204.8 kHz at all microphones except at 305 m (1000 ft). At 305 m, data was sampled at 96 kHz from  $0^\circ$  to  $80^\circ$  and at 51.2 kHz from  $90^\circ$  to  $160^\circ$ . Spectra are reported from 20 Hz to 20 kHz, well below one-quarter the sampling frequency for all but a few microphones at 305 m.

The temperature varied between  $19.4^\circ\text{C}$  and  $23.1^\circ\text{C}$ , and the relative humidity varied between 37.6% and 45.7%. These parameters were taken into account when calculating atmospheric absorption. The average wind speed was 3.3 kts (1.7 m/s). This chapter will focus on steady engine conditions of 50%, 75% (intermediate), 100% (military), 130% (minimum afterburner), and 150% (maximum afterburner) engine thrust request (ETR). Multiple data acquisition systems were used to collect the data from different organizations, and data taken by Brigham Young University, Blue Ridge Research and Consulting, LLC, and Wyle Laboratories will be reported here. See Ref. [56] for more information on the experimental setup and conditions.

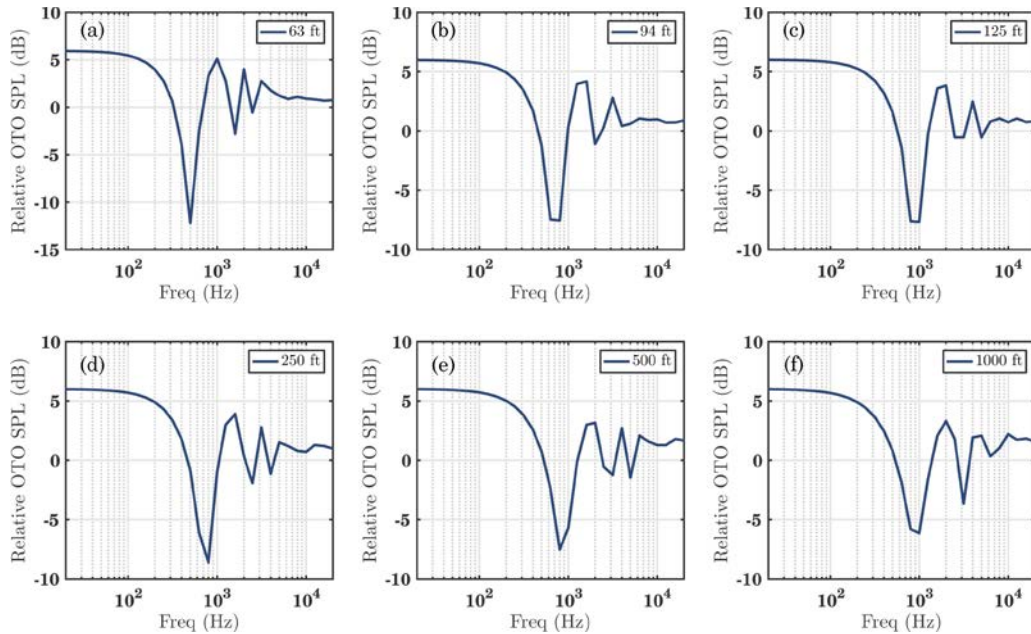


Figure 5.2. Relative OTO SPL due to ground reflections at varying distances. Each curve was calculated based on the height of the microphone and modeling the ground with flow resistivity of 4000 kPa s/m<sup>2</sup>.

## 5.2 Spectral Analysis

In this section, trends in OASPL, peak frequency, and PSD will be examined. However, before treating these, it is important to address the effect of ground reflections. The effect is dependent on ground conditions, source height, microphone height, distance, and frequency. The jet nozzle was at a nominal height of 2.1 m (81 in). Based on the microphone heights at each location, the change in measured SPL due to ground reflections was calculated at each microphone arc, modeling the ground as exposed earth with effective flow resistivity of 4000 kPa s/m<sup>2</sup>.<sup>60</sup> The only spectra for the F-35 shown here are OTO band data, so the relative SPL is given in OTO bands in Fig. 5.2. The main interference nulls occur between 400–1000 Hz, so caution must be used when interpreting  $v_N$  results around these frequencies. The effect of ground reflections on  $Q/S$  calculations for high-performance military aircraft has been shown previously in the literature.<sup>42</sup> The calculation of  $v_N$  and  $Q/S$  assumes one source nonlinearly

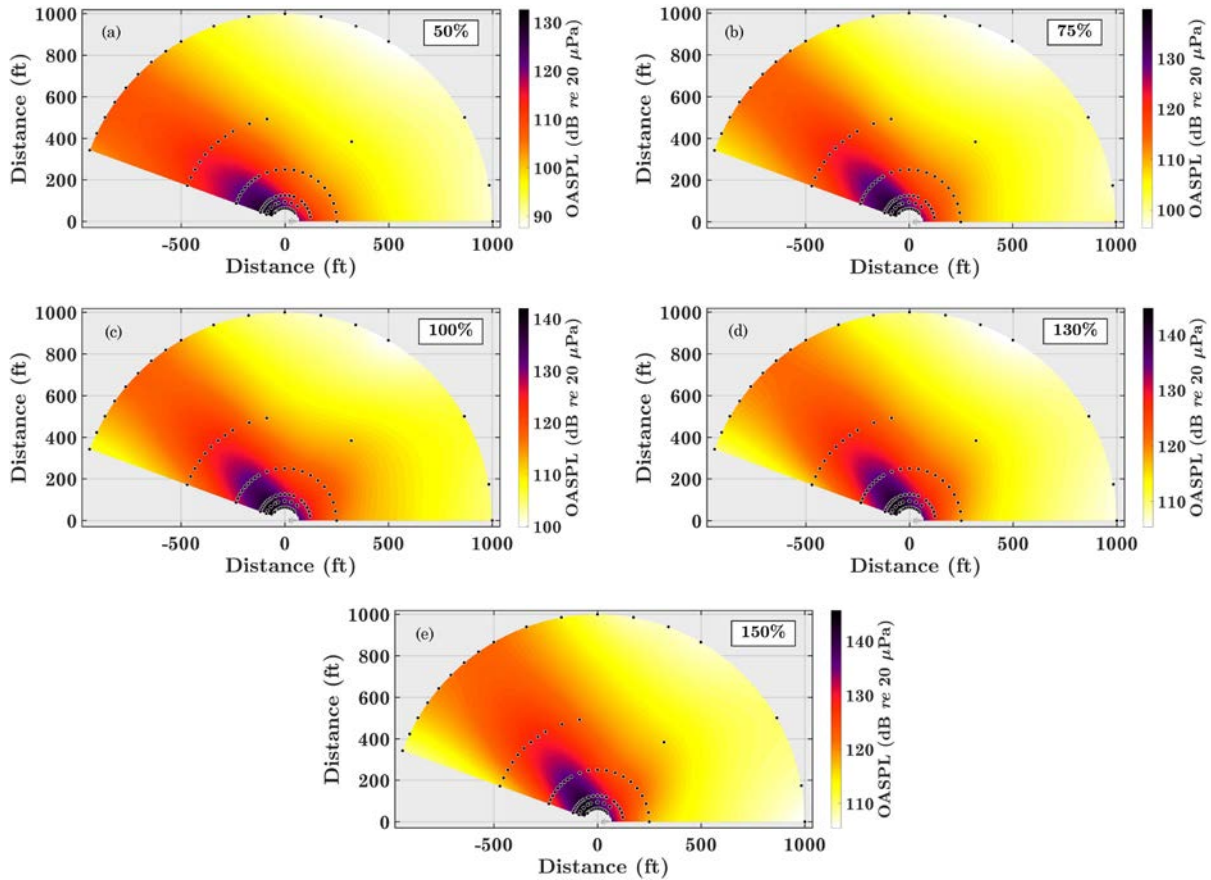


Figure 5.3. OASPL maps for each engine condition. The main radiation lobe moves upstream and levels increase with engine condition.

interacting with itself rather than the superposition of two sources far from one another. Nulls also occur at higher frequencies, but they are mostly averaged out by the larger OTO bandwidths.

Spatial maps of the OASPL are given in Fig. 5.3 for the five engine conditions. The radial distances of the microphone are as listed in Section 5.1, and the aircraft pictured near the origin is to scale. The levels are similar to those of the Mach-1.8 model-scale jet data from Section 4.3. A trend in directivity is visible, with the direction of the main radiation radial moving farther from the jet plume as engine condition increases. The highest level also increases by about 15 dB from lowest to highest engine condition. Peak frequency maps for each engine condition are displayed in Fig. 5.4. The peak frequency was found from the center-band

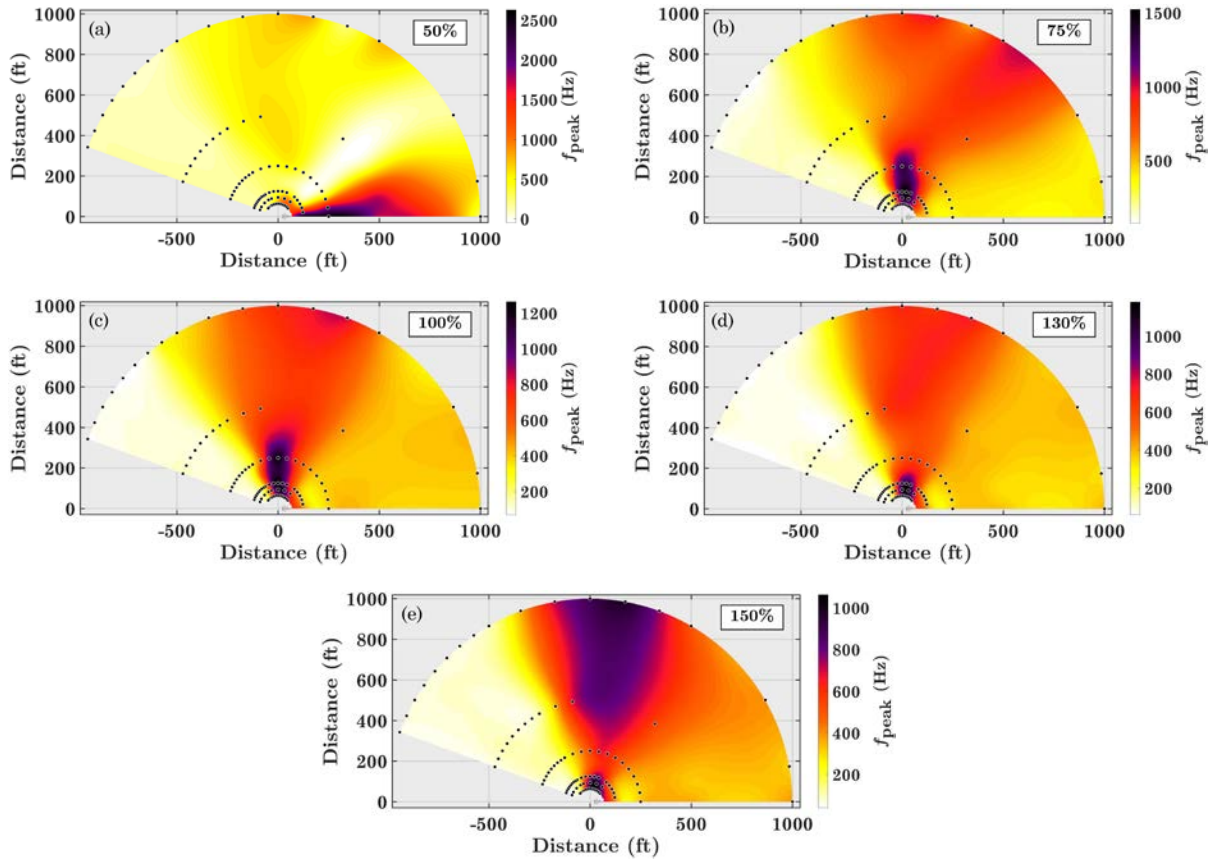


Figure 5.4. Peak frequency maps for each engine condition. Low frequencies are present in the peak radiation area, high frequencies perpendicular to the jet, and mid-range frequencies in the upstream direction.

frequencies of the OTO spectral peaks. An average of these center-band frequencies was performed across four separate runs at each condition to make the plots in Fig. 5.4. The general trend is that low frequencies are present at large angles (measured from the upstream direction) where the radiation is strongest, high frequencies are present perpendicular to the jet, and mid-range frequencies are present in the upstream direction. This is due to the varying directivity of the source, with high frequencies projecting farther upstream. The frequencies that are nonlinearly generated along each radial will depend on the peak frequency in that region, as seen in Section 5.3.

The trends in peak frequency with angle and distance can be viewed in a different light by examining the PSDs as a function of radius and angle. The peak frequency and pressure

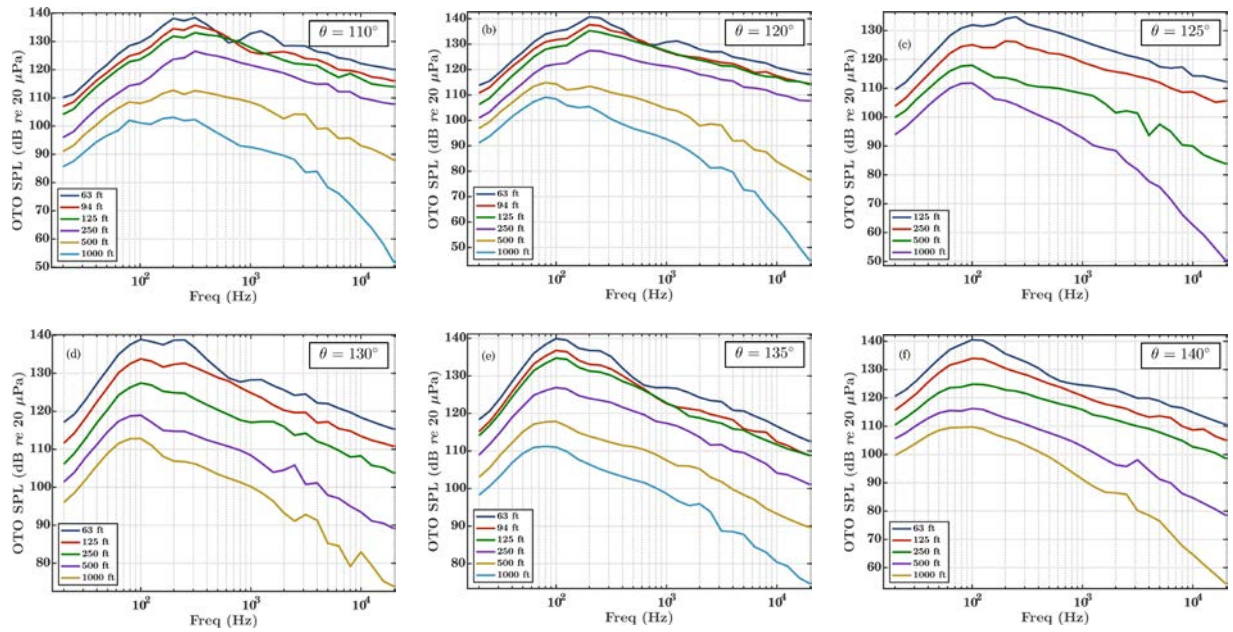


Figure 5.5. OTO SPL for six different angles and 130% ETR. Each plot displays the OTO SPL for all available microphones along the radial as a function of frequency. The peak frequency is larger for smaller angles. In addition, the rolloff at 1000 ft (305 m) is less at 130° and 135° than for the other angles.

amplitude close to the source impacts the spectral evolution even 305 m from the source. The OTO SPL levels along six different radials are shown for the 130% engine condition in Fig. 5.5. Note the high-frequency noise that is a result of scattering off microphone holders (this is even more obvious in the narrowband data, not shown here). See Section 3.4 for more information on scattering and the accuracy of  $v_N$ . At 130° and 135°, the 1000-ft data exhibit little to no deviation from a  $1/f^2$  power-law slope in the high frequencies, implying that the effects of nonlinearity and absorption are balanced. These angles have low peak frequencies and are located most closely to the peak radiation radial seen in Fig. 5.3 (d). The high-amplitude, low frequencies nonlinearly generate high frequencies very efficiently. At 125° and 140°, the 1000-ft data is only beginning to deviate from the power-law slope. The spectral peaks at these angles are starting to transition to higher frequencies, and the peak is more broad. This means that nonlinear generation will occur at a larger variety of frequencies. At 110° and 120° the deviation from a power-law slope

is significant, implying that absorption losses have begun to overcome nonlinear gains. The peak frequency is much higher at these angles, and the amplitude is slightly smaller. With propagation into the far field, however, the peak frequency begins to decrease. This is a function of the varying directivities of the low and high frequencies. Because the “fundamental” frequency is changing, it appears that nonlinear generation is not sufficient to balance absorption, but the high frequencies start to decay significantly. However, the decay away from a power-law slope at 110° and 120° is more shallow than either a linear ( $e^{f}$ ) or quadratic ( $e^{f^2}$ ) exponential decay. Because a linear exponential decay is expected in the far field of a nonlinear waveform, all of the waveforms in Fig. 5.5 appear to be short of the far field and contain evolving shocks.

## 5.3 Nonlinearity Analysis

### 5.3.1 Spectral and Spatial Plots of $v_N$ for Minimum Afterburner

The scattering that is visible in the OTO SPL plots in Fig. 5.5 is also visible in the spectral plots of  $v_N$ . The  $v_N$  spectra are shown in Fig. 5.6 for the same angles and radials as in Fig. 5.5. All data shown is below one-quarter the sampling frequency except for a few microphones at 1000 ft, as discussed in Section 5.1. For some angles,  $v_N$  starts off as negative close to the source and then eventually ends up positive. This is curious, because it is not expected that high frequencies close to the source would be losing energy. However, examination of the narrowband  $v_N$  spectral values (not pictured) reveals contamination due to scattering that is averaged to incorrect values in OTO bands. Therefore, unfortunately nearly all the negative  $v_N$  values at high frequencies and along the principal radiation lobe are due to scattering in the data and cannot be taken as accurate. It can be seen from Fig. 5.6 that the effect

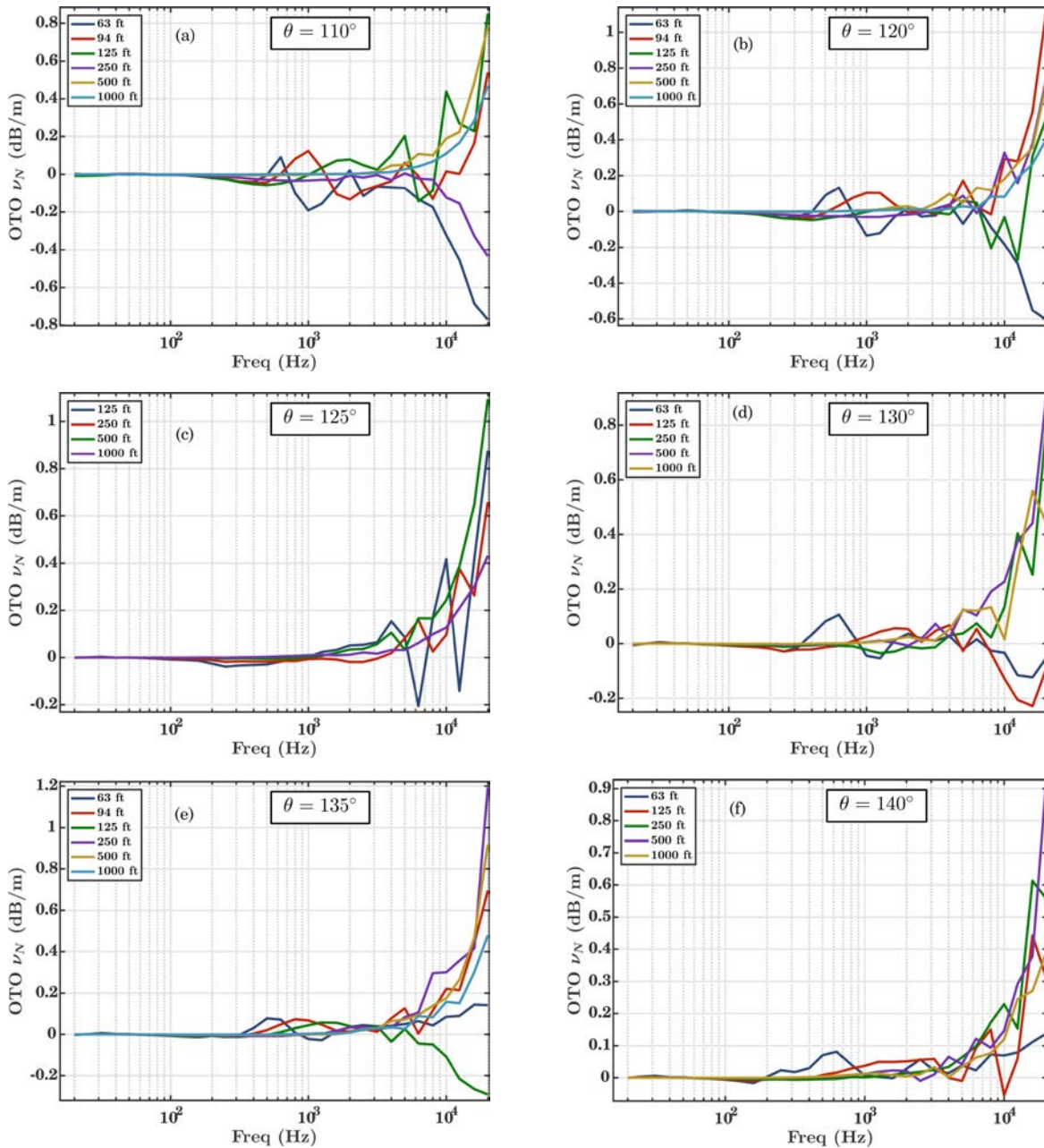


Figure 5.6. OTO  $\nu_N$  values for six different angles. The curves that go negative for distances close to the source are erroneous and due to scattering in the PSDs. Strong nonlinearity is present for all angles.

of scattering on  $\nu_N$  is generally worst for the 63 and 125 ft data, but the curves are fairly smooth at 500 and 1000 ft. However, there is still scattering present at these distances in the PSDs. So then why would the scattering affect some  $\nu_N$  curves and not others? Investigating the narrowband PSDs and  $\nu_N$  curves reveals that at 130% ETR, the spectral slope of the PSD up to

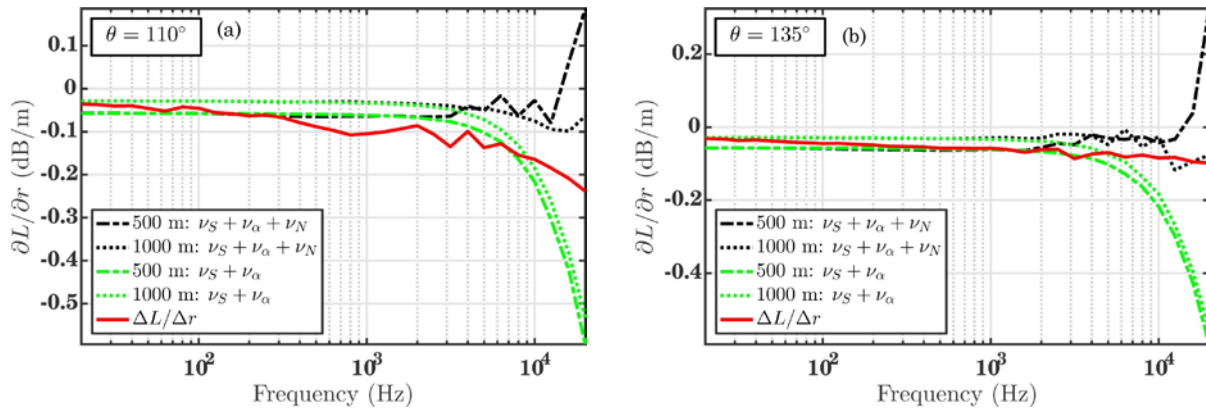


Figure 5.7. Predicted and actual changes in sound pressure level between 500 and 1000 ft at angles of (a)  $110^\circ$  and (b)  $135^\circ$ . The nonlinear predictions (black lines) are generally closer to the numerical derivatives (red lines) than are the linear predictions (green lines).

250 ft is a power-law slope typical of jet noise. However, at 500 and 1000 ft, the slope is steeper, showing some sign of absorption. It appears that the oscillations due to scattering when the PSD is near a power-law slope affect  $\nu_N$  more than when the rolloff is faster.

Despite these problems with scattering, spatial maps of  $\nu_N$  reveal what appear to be accurate trends in the data. The reliability of  $\nu_N$  for the full-scale jet is determined in a manner similar to that shown in Fig. 3.11 for the model-scale jet. Figure 5.7 shows the predicted and actual changes in sound pressure level between 500 and 1000 ft, calculated by summing the  $\nu$  indicators and performing numerical derivatives, respectively. The calculation is done for both (a)  $110^\circ$  and (b)  $135^\circ$ . The  $\nu$  values give instantaneous derivatives and the numerical derivative is a centered-difference between the microphones, so the  $\Delta L/\Delta r$  curve is expected to lie somewhere between the two  $\nu$  curves at 500 and 1000 ft. To illustrate the increased accuracy given when accounting for spreading, absorption, and nonlinearity (black lines), the sum of only spreading and absorption effects is also shown (green lines). Though the nonlinear predictions (black lines) do not exactly line up with the numerical derivatives (red lines), and scattering can be seen to negatively impact the nonlinear prediction, the agreement is close and the error is small. In fact, the slopes of the black and red lines are very similar, with only a vertical offset between them.

This offset with a consistent shape has been seen before in numerical propagation of the same dataset.<sup>61</sup> General trends given by the  $\nu_N$  indicator can be treated as mostly reliable for this dataset, particularly beyond 500 ft.

To further diminish errors due to scattering,  $\nu_N$  values from four different tests at the same engine power (130% ETR) were averaged. The averaged  $\nu_N$  values are presented for eight different frequencies in Fig. 5.8. Negative and positive values represent losses and gains in

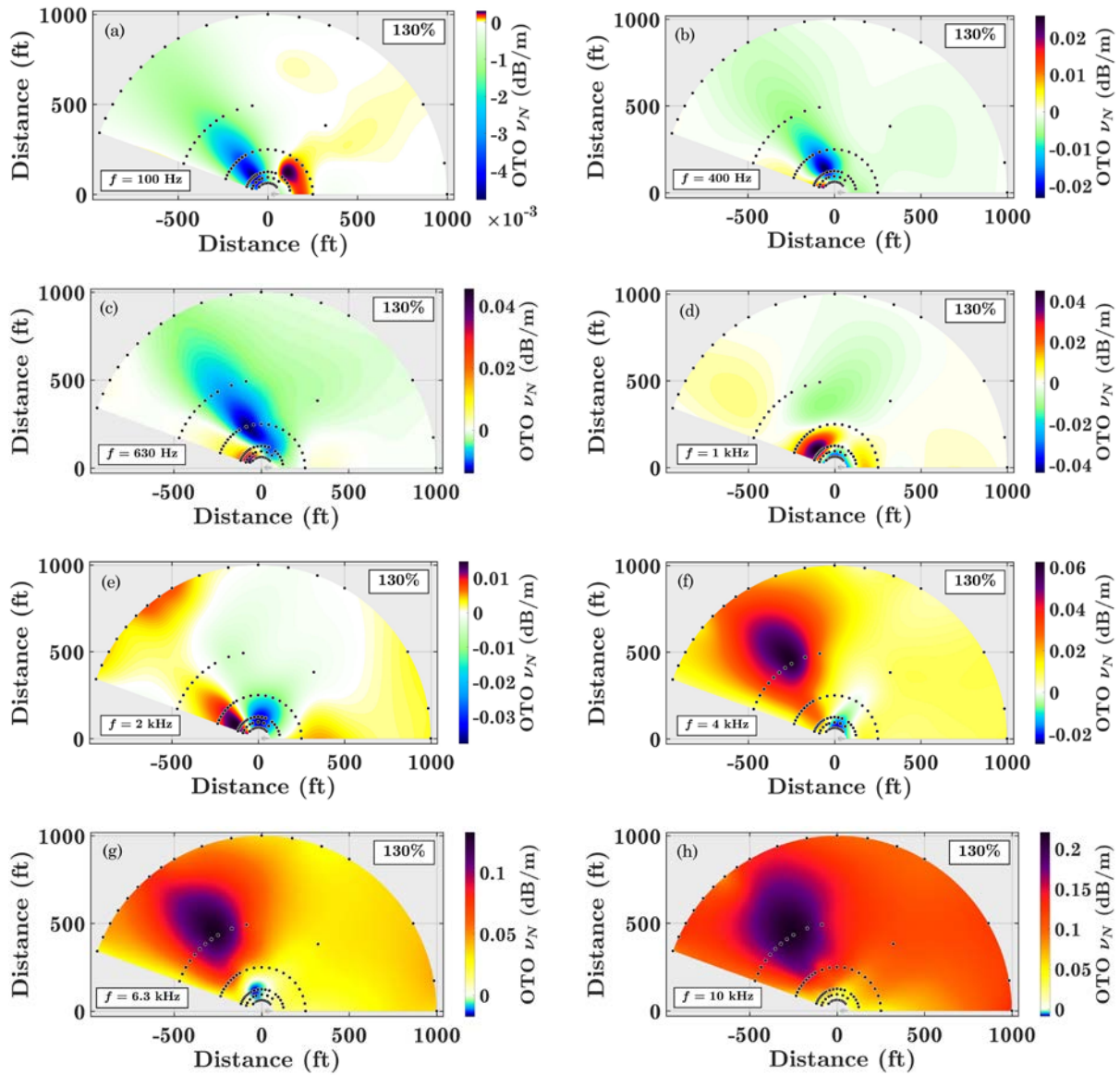


Figure 5.8. Spatial maps of  $\nu_N$  for eight different frequencies at 130% ETR. The trend shows loss of energy (negative values) at low frequencies and a transition to a gain of energy (positive values) at high frequencies. Ground reflections cause the 1-kHz data in (d) to be especially noisy.

energy due to nonlinearity, respectively. At very low frequencies, energy is being lost along the principal radiation lobe around  $130^\circ$ , and energy is being gained along the secondary radiation lobe around  $40^\circ$ . Part (b) shows a loss nearly everywhere. This is because 400 Hz is close to the peak frequency of both radiation lobes, so energy is being lost from this frequency and transferred to others. At 630 Hz, part (c) shows a transition from nonlinear loss to nonlinear gain at  $130^\circ$ , but the 1 kHz data in part (d) is contaminated by ground reflections (see Fig. 5.2). Figures 5.8 (e) and (f) have gains along the principal lobe and losses along the secondary lobe, illustrating the importance of peak frequency in nonlinear frequency generation. As frequency increases, the maximum  $v_N$  also increases for each map, seen in parts (e)-(h). The slight negative values near the source for parts (g) and (h) are potentially due to scattering in the data. However, they could also be a result of the increased losses due to nonlinear geometric spreading discussed at the beginning of Section 2.3. The asymptotic behavior of an initial sinusoid with thermoviscous absorption and spherical spreading is a nonlinear decay of  $r^{-n}e^{-nar}$  that is ultimately less than the linear decay of  $r^{-1}e^{-n^2ar}$ . If this larger spreading decay was somehow present close to the source for the jet noise data, then  $v_N$  could be negative, indicating increased spreading losses. However, the increased spreading decay is only expected asymptotically, so it is likely that the negative  $v_N$  values are not due to increased spreading losses but due to scattering in the data.

### 5.3.2 Comparison of Engine Conditions

To compare engine conditions, not only the nonlinearity indicator will be used, but also the sum of the absorption and nonlinearity indicators. This will allow for determining the asymptotic behavior of the noise by looking in the far field. As a reference, Fig. 5.9 shows the  $v_\alpha$

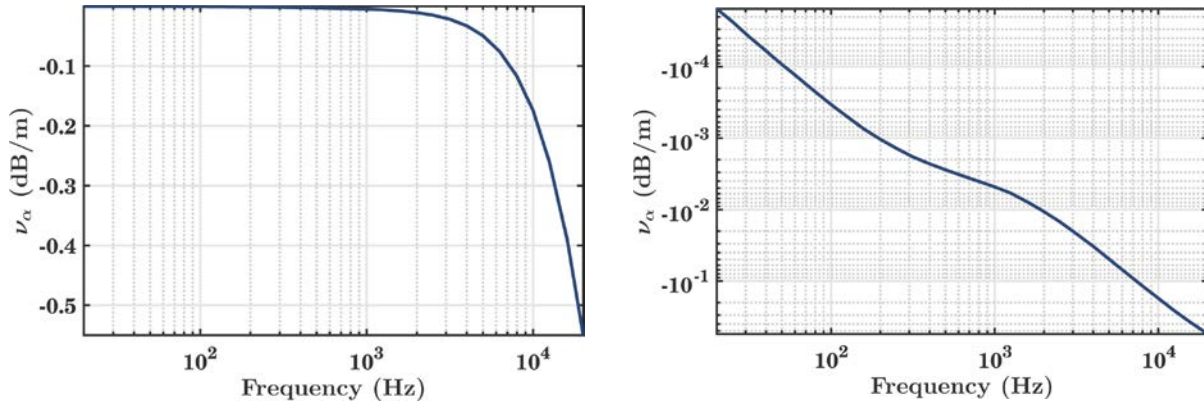


Figure 5.9. The spatial rate of change in SPL due to absorption,  $\nu_\alpha$ , as a function of frequency for typical measured weather conditions. The parameter  $\nu_\alpha$  is shown on a (a) linear and (b) logarithmic scale.

values for the average atmospheric conditions given in Section 5.1. Based on the discussion in Section 2.3,  $\nu_N$  should be positive and the sum  $\nu_\alpha + \nu_N$  should be slightly negative in the far field, corresponding to a decreased absorption. However, from Fig. 5.5, some far-field spectra have begun to exhibit a linear ( $e^{-f}$ ) exponential decay and others continue in a  $1/f^2$  spectral power-law decay. Where the power-law decay is still present, this means that effects from nonlinearity and absorption are nearly equal, and the sum  $\nu_\alpha + \nu_N$  should be close to zero; the spectral shape remains constant and the spatial derivative is nonzero only due to spreading. At these points, the total energy is sufficient to continue to drive nonlinear frequency generation and the waveform is not yet in the old age.

The directivity changes in OASPL for each condition (see Fig. 5.3) are expected to be mirrored by  $\nu_N$ . Figure 5.10 shows the  $\nu_N$  values for 100 Hz and 10 kHz for each engine condition. For each 100-Hz plot, the lobe where energy is lost tracks the OASPL lobe as engine condition increases. Similarly,  $\nu_N$  at 10 kHz shows not only the same varying directivity, but the overall magnitude of the indicator also increases with condition. The spatial rate of change due to nonlinearity increases by nearly a factor of four between 50% and 150% ETR [compare parts (b) and (j)]. Most interesting, however, are the plots for the sum  $\nu_\alpha + \nu_N$  shown in Fig. 5.11. The 50%

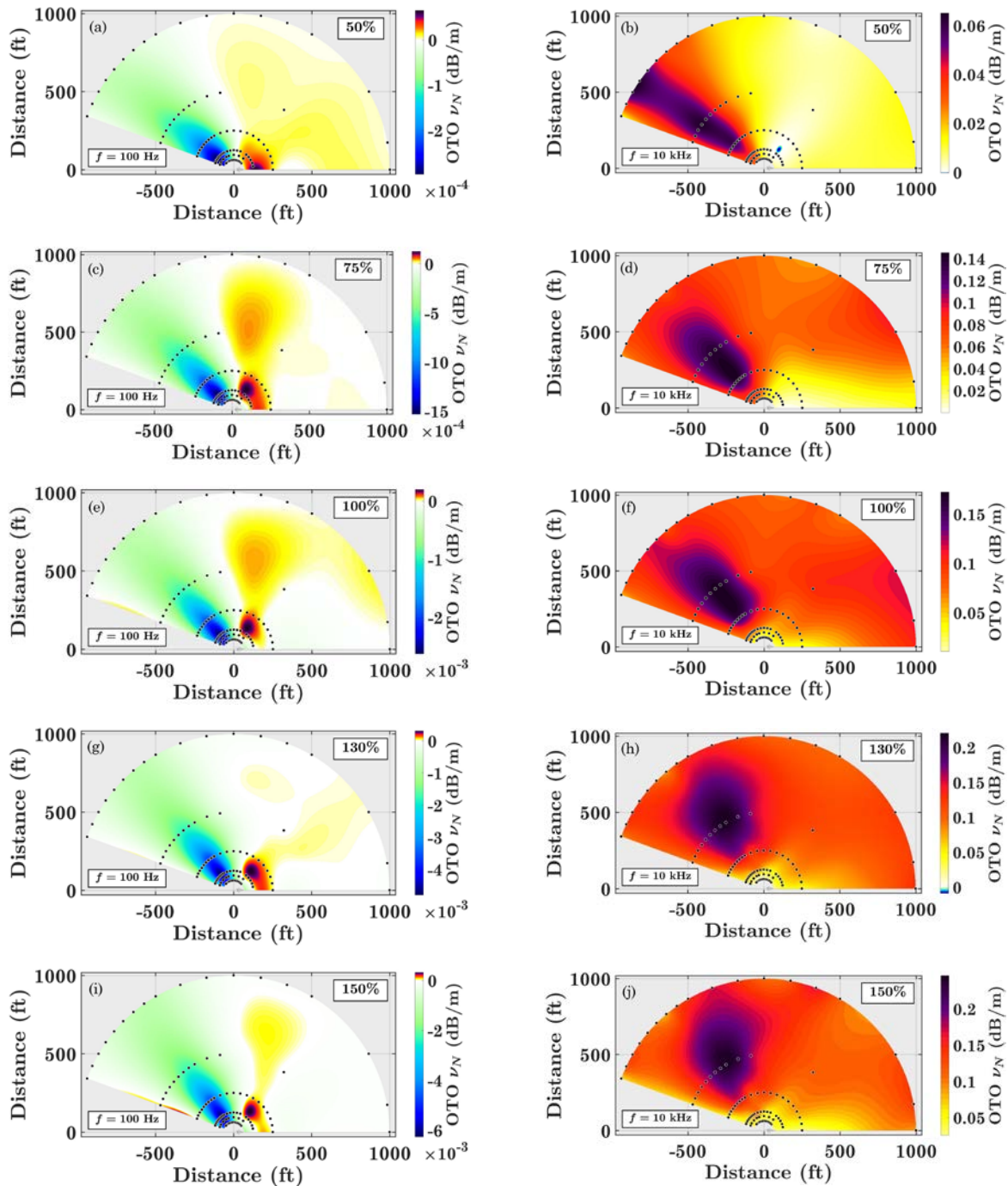


Figure 5.10. Spatial maps of  $\nu_N$ . The first column shows  $\nu_N$  at 100 Hz. Nonlinear losses are seen in the peak radiation range. The second column shows  $\nu_N$  at 10 kHz. Nonlinear growth increases with engine condition, and the directivity moves upstream as well.

and 75% ETR plots in parts (a) and (b), respectively, show that absorption is stronger than nonlinearity everywhere: the sum is never positive. The sum for the 100% ETR case in part (c), however, goes to zero along the principal radiation lobe at 152 m (500 ft). For local propagation

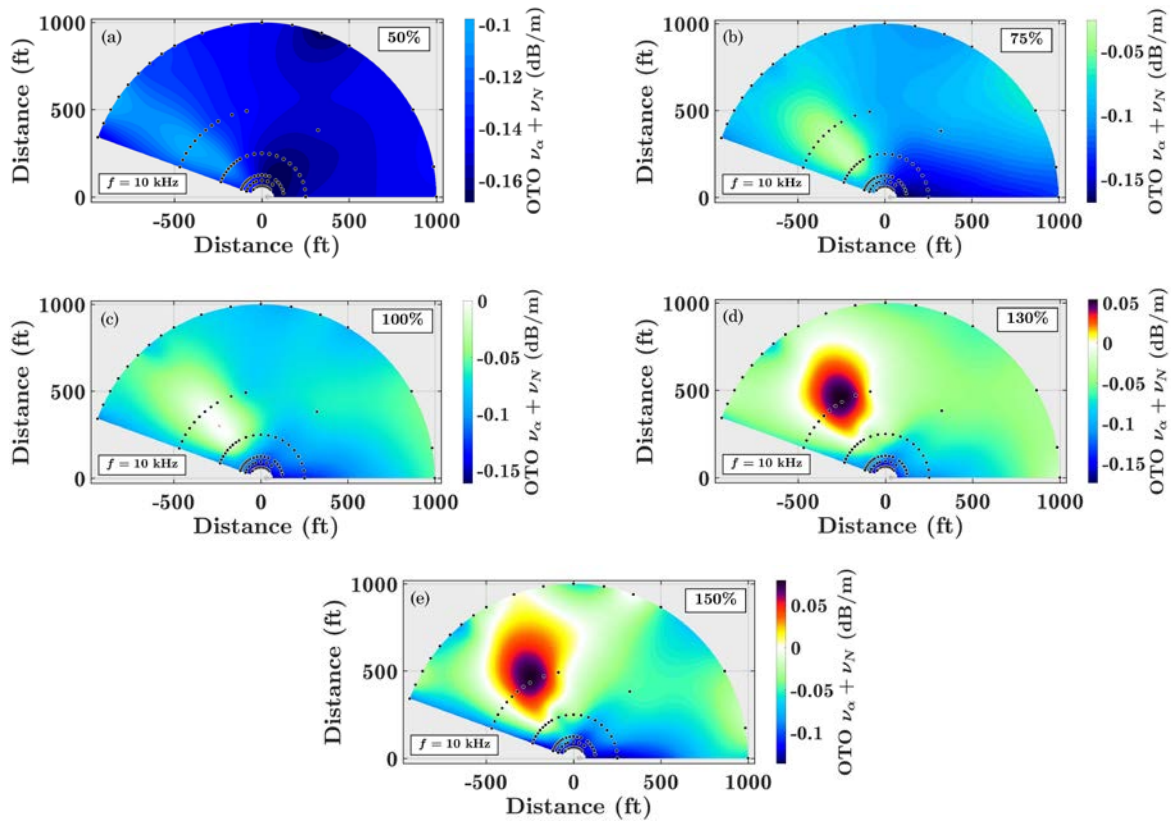


Figure 5.11. Spatial maps of the sum  $\nu_N + \nu_\alpha$  at 10 kHz. Nonlinearity balances or overcomes absorption only for the 100%, 130%, and 150% engine conditions.

away from 152 m, the spectral shape thus remains constant, neither increasing nor decreasing from its power-law shape. The weak shocks here have formed and are possibly near their maximum heights; the waveform has not yet entered the old-age region. It is expected from the asymptotic solution that in the far field, the sum  $\nu_\alpha + \nu_N$  will go negative. This is exactly what happens at 305 m (1000 ft) in part (c). Here absorption has overcome nonlinearity, and a linear exponential decay has begun.

Note that the sum is negative within 76.2 m (250 ft) for all conditions. This is definitely unexpected for 130% and 150% ETR, because there should be initial high-frequency growth due to nonlinearity. Recall, however, that the scattering off the microphone holders generally decreases the value of  $\nu_N$  (see Section 5.3.1), which could make the sum negative when it should be positive. For the 130% and 150% ETR maps in Figs. 5.11 (d) and (e), the sum becomes

positive for some microphones at 152 m (500 ft) before going negative again at 305 m (1000 ft). It is unclear why the amplitude of the 10-kHz frequency should be increasing that far from the source, rather than simply remaining constant. Based on the spectral shapes in Fig. 5.5, the characteristic power-law slope seems to have formed by 28.6 m (94 ft). Little or no change in the spectrum at 10 kHz is observed along the main radiation radial, so the sum in Fig. 5.11 (d) is expected to be zero at 152 m (500 ft) as it is in part (c). However, the color bar reveals that the positive amplitude is small. It is likely that at this frequency, which is about 5% the sampling frequency, a small amount of positive error is present in  $v_N$  (see errors from Section 3.2). This small positive error makes the sum slightly positive instead of close to zero.

However, a trend is still visible through the errors: at 152 m (500 ft) in Fig. 5.11 (d), nonlinearity remains of similar strength as absorption, and only at 305 m (1000 ft) does the expected asymptotic decay begin to happen. In fact, the 150% ETR condition even shows some microphones at 305 m (1000 ft) that have not begun to show the old-age decay. Evidence is found in Fig. 5.11 (e), which shows some microphones between  $100^\circ$  and  $120^\circ$  at 305 m where the sum  $v_\alpha + v_N$  is zero. In the old-age region, a small negative decay is expected (the spectrum develops a linear exponential decay), but  $v_N$  remains large enough out to 305 m that nonlinear generation is still prevalent. In summary, the strength of nonlinearity varies greatly between engine conditions, but growth due to nonlinearity is seen to balance the decay due to nonlinearity before an overall decay is experienced in the far field.

### 5.3.3 Other Nonlinearity Metrics

In addition to the analysis given here, these same F-35 data have been analyzed previously.<sup>56</sup> The parameters reported include OASPL, OTO SPL, directivity, pressure

skewness, and pressure time-derivative skewness. The pressure skewness was seen to peak at angles upstream of the OASPL maximum, but the pressure time-derivative skewness peaked close to the OASPL maximum. For background information, the pressure time-derivative skewness is calculated by

$$Sk\left\{\frac{\partial p}{\partial t}\right\} = \frac{E\left[\left(\frac{\partial p}{\partial t}\right)^3\right]}{E\left[\left(\frac{\partial p}{\partial t}\right)^2\right]^{3/2}} \cdot \quad (5.1)$$

This indicator has been studied specifically for shock-containing noise, and a derivative skewness value of five has been found to indicate presence of significant shocks.<sup>23</sup> In Ref. [56], the derivative skewness values were approximately zero for the lowest power engine condition.

The derivative skewness for the 130% ETR condition is shown in Fig. 5.12. The values exceed 23 around 210 m before decreasing again in the far field. This increase and decrease suggests a large initial increase in weak shocks followed by a decay of the shocks. The derivative skewness is proportional to the cube of the pressure derivative [see Eq. (5.1)], so it is most sensitive to the largest shock in the entire waveform. The large shocks will form, decay, and thicken faster than the smaller shocks, which may still be increasing in magnitude out to 152 or

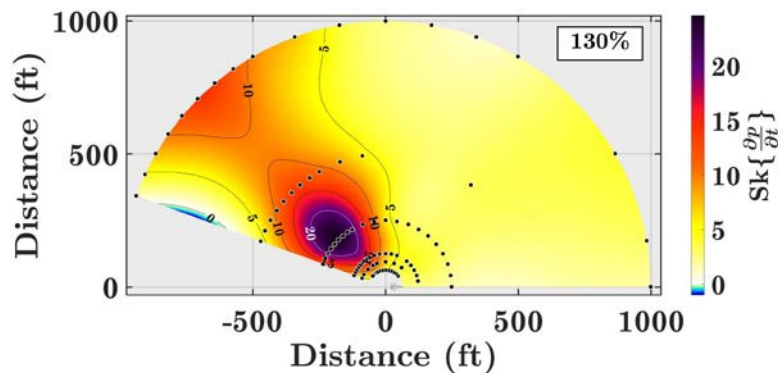


Figure 5.12. Derivative skewness values for 130% ETR. The derivative skewness peaks at 76.2 m (250 ft) due to its dependence on the cube of the pressure derivative, or sensitivity to the largest shocks.

even 305 m (500 or 1000 ft). This sensitivity causes the derivative skewness to peak and decrease quickly after 76.2 m (250 ft). The width of the derivative skewness lobe increases with propagation, suggesting an increase in weak shocks across larger angles with propagation. Similar increase in magnitude and breadth of this indicator corresponds with the results of the  $v_N$  indicator. As seen in the 10-kHz plots in Fig. 5.10, the indicator grows for high engine conditions before decaying again in the far field. The breadth of the lobe also experiences significant growth with propagation. Like the pressure time-derivative skewness,  $v_N$  at 10 kHz peaks close to the same angle as the OASPL, rather than upstream—like the pressure skewness.

Another indicator that can be used to characterize nonlinearity is the average steepening factor (ASF).<sup>15</sup> The ASF is the ratio of the average positive slope to the average negative slope, or

$$\text{ASF} = \frac{E[\dot{p}^+]}{E[\dot{p}^-]}, \quad (5.2)$$

where a dot above the pressure variable indicates a derivative. The ASF increases with shocks in a waveform. This indicator has not been calculated before from these data, but results are given here. Figure 5.13 shows the ASF for the five different engine conditions. Similar to  $v_N$  and the derivative skewness, the ASF increases in value and broadens with propagation from the source. However, unlike the other indicators, the ASF remains large in the far field; there is little change between the values at 500 and 1000 ft for each plot in Fig. 5.13. The ASF is an indicator averaged over the entire waveform, so it is less sensitive to the largest shocks in the data.

Current and future work involves characterizing the amount of annoyance due to crackle from the F-35 noise waveforms, then looking for correlations between nonlinearity indicators. Preliminary results from a subjective evaluation of crackle show a strong correlation between crackle, the derivative skewness, the ASF, and  $v_N$ .

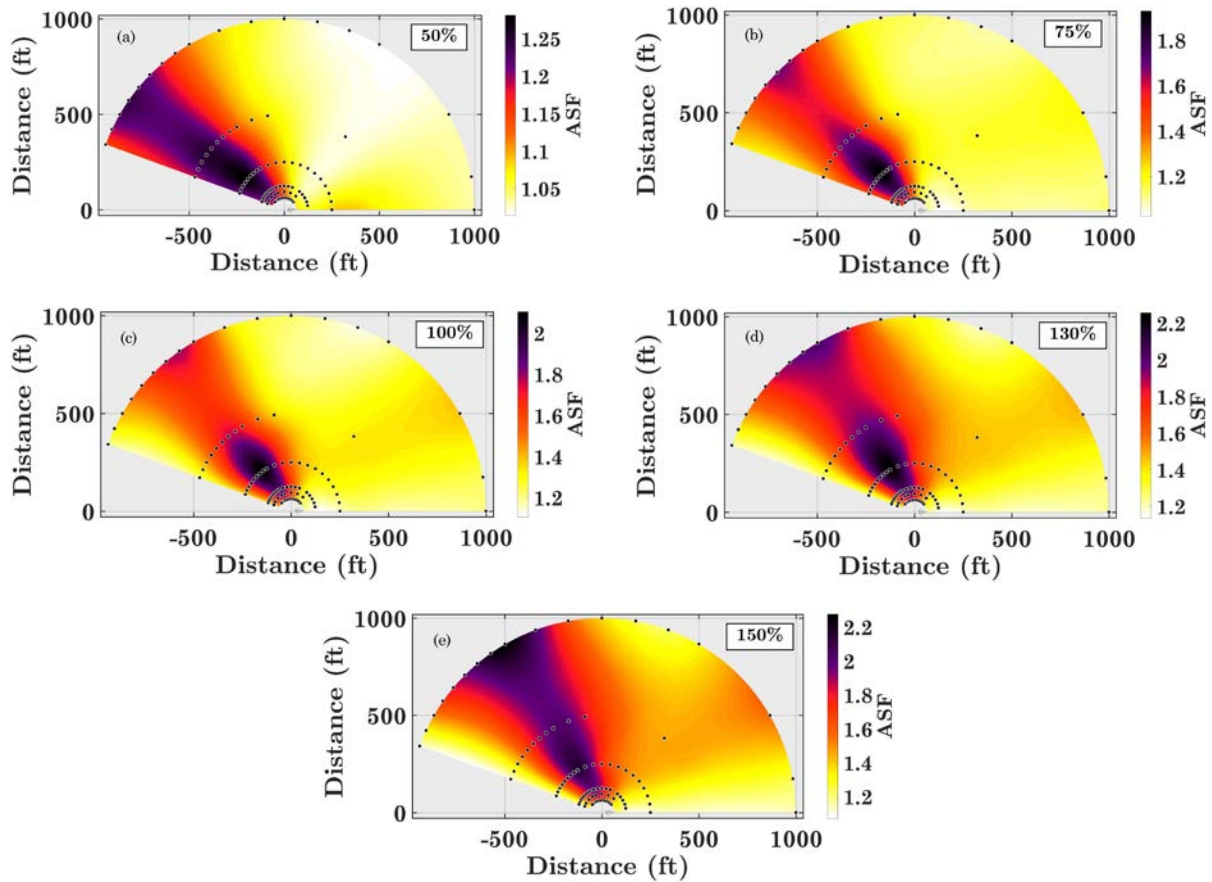


Figure 5.13. Average steepening factor (ASF) for five engine conditions. Similar to  $v_N$  and the derivative skewness, the breadth of the lobe increases with propagation. However, the ASF uniquely remains high in the far field.

At high frequencies, the  $v_N$  indicator behaves similarly to the pressure time-derivative skewness and ASF nonlinearity indicators. However, the derivative skewness is sensitive to the maximum shock amplitude while the ASF and  $v_N$  indicator look more at average properties. But the  $v_N$  indicator is so useful because it contains important information as a function of frequency. It characterizes energy loss at low frequencies along with the overall nonlinear trends given by other indicators. It is sensitive to the peak frequency of shock containing noise as well. However, a limiting factor is the error in the indicator at high frequencies; care must be taken to ensure a sufficiently large sampling frequency is used. Overall, these features make  $v_N$  a viable candidate to be a nonlinearity indicator and possibly a metric for other annoyances due to nonlinearity.

# Chapter 6

## Concluding Discussion

The study of a single-point nonlinearity indicator aids the understanding of noise from high-amplitude sources, such as high-performance military aircraft. This indicator, referred to as  $v_N$ , yields information about the rate at which nonlinear energy transfer and waveform steepening is occurring. The indicator value from a single measurement can provide similar information as can the traditional method of comparing the spectra measured at multiple locations in space. In addition, use of the indicators  $v_S$ ,  $v_a$ , and  $v_N$  makes for an easy comparison of the effects of geometric spreading, thermoviscous absorption, and nonlinearity. These indicators give a spatial derivative of the sound pressure level spectrum due to the different effects.

### 6.1 Summary of Findings

To understand the expected behavior of  $v_N$ , tests were first performed on various well-known analytical and computational solutions to the generalized Burgers equation (GBE) for initial sinusoids in Chapter 2. The  $v_N$  indicator is large and positive as harmonics are first nonlinearly generated. Asymptotically with distance, the indicator is positive with increasing magnitude as a function of frequency and acts to slow the decay from absorption. The only

exception is for the Blackstock Bridging Function (BBF), where spreading and absorption are ignored and  $v_N$  is asymptotically negative, signifying nonlinear losses at the shock.

With increased intuition from the analytical solutions, the impact of experimental conditions was then examined in Chapter 3. The effect of sampling frequency, bandwidth, scattering, and noise was explored. Though large errors are present for some analytical and computational nonlinear waveforms, the indicator is fairly accurate for experimentally measured broadband noise to about one-quarter the sampling frequency. In Chapters 4 and 5, low- and high-amplitude experimental signals were tested to show that  $v_N$  is only nonzero for high-amplitude signals, both in the model-scale and full-scale jet data. For high-amplitude signals,  $v_N$  shows nonlinear growth of high frequencies and decay of low frequencies as shocks develop. In the far field, absorption and nonlinearity combine to cause a linear ( $e^{-f}$ ) exponential decay as predicted by theory. Despite the care to be taken with experimental conditions, the  $v_N$  indicator reveals valuable insights into broadband noise data.

## 6.2 Summary of Contributions

This section summarizes the unique contributions to this work by the author. The numerical test cases in Chapter 2 were calculated and plotted, allowing for a better understanding of the expected behavior of  $v_N$  for various scenarios. In addition, the asymptotic expressions of  $v_N$  for the Mendousse and spherically spreading cases were determined. The investigations in Chapter 3 concerning the potential issues with  $v_N$  were original and carried out by the author, including the derivation found in Section 3.1. These investigations shed light on the proper use of the Morfey-Howell indicator and cautioned against improper past and future use. To the author's knowledge, no other known document treats the impact of sampling frequency on the

accuracy of this quadspectral nonlinearity indicator and its inaccuracy at frequencies lower than the Nyquist. The model-scale jet data has been analyzed with other nonlinearity indicators,<sup>5, 16, 45</sup> but for the first time the  $v_N$  indicator was used. In addition, the author examined the behavior of the indicators and drew unique conclusions by relating them to theory. Data from F-35 aircraft have been analyzed previously,<sup>14, 57, 59</sup> including the particular dataset reported in Chapter 5.<sup>56</sup> However, the detailed examination of spectra, OTO levels, and the  $v_N$  indicator is original to this dataset. In addition, experimental recommendations were made based on the observed scattering in the dataset.

### **6.3 Implications and Recommendations**

From the investigations in Chapters 3-5, a few recommendations can be made about conducting experiments for determining the nonlinearity in a signal using  $v_N$ . As a general rule,  $v_N$  values should never be trusted above one-quarter the sampling frequency. However, even the error at one-quarter the sampling frequency can be as large as (or larger than) 20%. The sampling frequency should therefore be made as high as reasonably possible to provide an adequate frequency range for nonlinearity calculations. Because the high-frequency data is so crucial to these nonlinearity calculations, care should be taken to minimize the scattering in the data. Especially when the PSD has a characteristic  $1/f^2$  power-law slope, scattering can drastically impair the accuracy of the  $v_N$  indicator unless extensive averaging is used. It is recommended that, until further experiments are conducted with a diversity of signals measured by closely spaced microphones—varying sampling frequency, bandwidth, scattering, etc.—the accuracy of  $v_N$  be verified with experimentally measured spatial derivatives up to one-quarter the sampling frequency as done in Section 3.3.2.

Future work most importantly includes using a controlled environment where experimental waveforms of various types can be tested and characterized for errors in  $v_N$ . The accuracy of the indicator appears to depend drastically on sampling frequency and waveform type, and this dependence must be explored through experimental data, perhaps in a plane-wave tube. For other future endeavors, indicators similar to the  $v$  indicators, but for model equations other than the generalized Burgers equation could be developed. Alternate methods of computing the quadspectral density,  $Q_{pp^2}$ , could also be explored. One such method deals with integrating the bispectrum, which does not involve calculating the cross-spectrum of the waveform and waveform squared. In addition, the behavior of nonlinearly propagating waveforms with spherical spreading could be more fully studied in relation to a normalized spherical distance, characterizing waveform shape as a function of that normalized distance. Finally, correlation of the perception of crackle with  $v_N$  and other nonlinearity metrics could be performed to determine their utility as crackle indicators.

The  $v_N$  indicator has been shown to provide meaningful information about the nonlinear growth and decay of harmonics for well-known solutions. It has been shown to depend on the amplitude of a signal, giving nonzero results only when nonlinearity is present in the data. The indicator provides a quantitative spatial change in sound pressure level due to nonlinearity alone, which can be verified by experiment. The  $v_N$  indicator is especially valuable because it is frequency dependent, and correlation of  $v_N$  with other nonlinearity indicators shows its significance.

# References

- [1] D. T. Blackstock, *Fundamentals of physical acoustics*, (Wiley, New York, 2000).
- [2] M. F. Hamilton and D. T. Blackstock, *Nonlinear Acoustics*, (Academic Press, San Diego, 1998).
- [3] C. L. Nikias and A. P. Petropulu, *Higher-Order Spectra Analysis: A Nonlinear Signal Processing Framework*, (Prentice Hall, Upper Saddle River, NJ, 1993).
- [4] K. L. Gee, R. J. Kenny, T. B. Neilsen, T. W. Jerome, C. M. Hobbs and M. M. James, "Spectral and statistical analysis of noise from reusable solid rocket motors," in *Proc. Mtgs. Acoust.*, **18**, (Acoustical Society of America), p. 040002.
- [5] K. L. Gee, T. B. Neilsen and A. A. Atchley, "Skewness and shock formation in laboratory-scale supersonic jet data," *J. Acous. Soc. Am.* **133**, EL491-EL497 (2013).
- [6] K. L. Gee, T. B. Neilsen, M. Downing, M. M. James and S. A. McNerny, "Characterizing nonlinearity in jet aircraft flyover data," in *Proc. Mtgs. Acoust.*, **12**, (Acoustical Society of America), p. 040008.
- [7] B. P. Petitjean, K. Viswanathan and D. K. McLaughlin, "Acoustic pressure waveforms measured in high speed jet noise experiencing nonlinear propagation," *Int. J. Aeroacoust.* **5**, 193-215 (2006).

- [8] K. L. Gee, "Prediction of nonlinear jet noise propagation," Ph. D. Thesis, Pennsylvania State University, 2005.
- [9] J. H. Ginsberg and M. F. Hamilton, "Computational methods," in *Nonlinear Acoustics*, (American Press, San Diego, 1998), pp. 309-342.
- [10] M. R. Shepherd, K. L. Gee and M. S. Wochner, "Short-range shock formation and coalescence in numerical simulation of broadband noise propagation," *J. Acous. Soc. Am.* **126**, 2886-2893 (2009).
- [11] M F. Hamilton and C. L. Morfey, "Model Equations," in *Nonlinear Acoustics*, (American Press, San Diego, 2008), pp. 57-59.
- [12] R. O. Cleveland, J. P. Chambers, H. E. Bass, R. Raspet, D. T. Blackstock and M. F. Hamilton, "Comparison of computer codes for the propagation of sonic boom waveforms through isothermal atmospheres," *J. Acous. Soc. Am.* **100**, 3017-3027 (1996).
- [13] D. T. Blackstock, M F. Hamilton and A. D. Pierce, "Progressive Waves in Lossless and Lossy Fluids," in *Nonlinear Acoustics*, (American Press, San Diego, 2008), pp. 139-142.
- [14] K. L. Gee, T. B. Neilsen, J. M. Downing, M. M. James, R. L. McKinley, R. C. McKinley and A. T. Wall, "Near-field shock formation in noise propagation from a high-power jet aircraft," *J. Acous. Soc. Am.* **133**, EL88-EL93 (2013).
- [15] M. B. Muhlestein, K. L. Gee, T. B. Neilsen and D. C. Thomas, "Evolution of the average steepening factor for nonlinearly propagating waves," *J. Acous. Soc. Am.* **137**, 640-650 (2015).
- [16] K. L. Gee, A. A. Atchley, L. E. Falco, M. R. Shepherd, L. S. Ukeiley, B. J. Jansen and J. M. Seiner, "Bicoherence analysis of model-scale jet noise," *J. Acous. Soc. Am.* **128**, EL211-EL216 (2010).

- [17] C. L. Morfey and G. P. Howell, "Nonlinear propagation of aircraft noise in the atmosphere," *AIAA Journal* **19**, 986-992 (1981).
- [18] K. L. Gee, A. A. Atchley, L. E. Falco and M. R. Shepherd, "Nonlinearity analysis of model-scale jet noise," in *19th International Symposium on Nonlinear Acoustics*, AIP Conference Proceedings, **1474**, edited by T. Kamakura and N. Sugimoto (AIP Publishing, 2012), pp. 307-310.
- [19] W. J. Baars, C. E. Tinney, M. S. Wochner and M. F. Hamilton, "On cumulative nonlinear acoustic waveform distortions from high-speed jets," *J. Fluid Mech.* **749**, 331-366 (2014).
- [20] S. A. McInerny, M. Downing, C. Hobbs, M. James and M. Hannon, "Metrics that characterize nonlinearity in jet noise," *AIP Conf. Proc.* **838**, 560-563 (2006).
- [21] S. A. McInerny and S. M. Ölçmen, "High-intensity rocket noise: Nonlinear propagation, atmospheric absorption, and characterization," *J. Acous. Soc. Am.* **117**, 578-591 (2005).
- [22] S. H. Swift and K. L. Gee, "Examining the use of a time-varying loudness algorithm for quantifying characteristics of nonlinearly propagated noise (L)," *J. Acous. Soc. Am.* **129**, 2753-2756 (2011).
- [23] B. O. Reichman, M. B. Muhlestein, K. L. Gee, T. B. Neilsen and D. C. Thomas, "Evolution of the derivative skewness for nonlinearly propagating waves," *J. Acous. Soc. Am.* **139**, 1390-1403 (2016).
- [24] B. O. Reichman, K. L. Gee, T. B. Neilsen and K. G. Miller, "Quantitative analysis of a frequency-domain nonlinearity indicator," *J. Acous. Soc. Am.* **139**, 2505-2513 (2016).
- [25] L. E. Falco, "Single-point nonlinearity indicators for the propagation of high amplitude acoustic signals," PhD Thesis, The Pennsylvania State University, 2007.

- [26] D. E. Gagnon, "Bispectral analysis of nonlinear acoustic propagation," The University of Texas at Austin, 2011.
- [27] S. Elgar and R. T. Guza, "Statistics of bicoherence," *Acoustics, Speech and Signal Processing, IEEE Transactions on* **36**, 1667-1668 (1988).
- [28] Y. C. Kim and E. J. Powers, "Digital bispectral analysis and its applications to nonlinear wave interactions," *IEEE Trans. Plasma Sci.* **7**, 120-131 (1979).
- [29] K. L. Gee, A. A. Atchley, L. E. Falco, T. B. Gabrielson and V. W. Sparrow, "Bispectral analysis of high-amplitude jet noise," *AIAA Paper 2005-2937*, (2005).
- [30] D. T. Blackstock, "Connection between the Fay and Fubini solutions for plane sound waves of finite amplitude," *J. Acous. Soc. Am.* **39**, 1019-1026 (1966).
- [31] A. D. Pierce, "Nonlinear Effects in Sound Propagation," in *Acoustics: an Introduction to Its Physical Principles and Applications*, (The Acoustical Society of America, Melville, NY, 1989), pp. 594-597.
- [32] D. T. Blackstock, "Once Nonlinear, Always Nonlinear," *AIP Conf. Proc.* **838**, 601-606 (2006).
- [33] D. A. Webster and D. T. Blackstock. "Experimental Investigation of Outdoor Propagation of Finite-Amplitude Noise," August 1978 Contract No.: N78-31876, pp. 96-103.
- [34] D. A. Webster and D. T. Blackstock, "Asymptotic decay of periodic spherical waves in dissipative media," *J. Acous. Soc. Am.* **64**, S33 (1978).
- [35] K. G. Miller, B. O. Reichman, K. L. Gee, T. B. Neilsen and A. A. Atchley, "Quantitative nonlinearity analysis of model-scale jet noise," in *RECENT DEVELOPMENTS IN NONLINEAR ACOUSTICS: 20th International Symposium on Nonlinear Acoustics including the 2nd International Sonic Boom Forum*, **1685**, (AIP Publishing), p. 090003.

- [36] D. T. Blackstock, M F. Hamilton and A. D. Pierce, "Progressive Waves in Lossless and Lossy Fluids," in *Nonlinear Acoustics*, (American Press, San Diego, 2008), pp. 129-132.
- [37] S. N. Gurbatov and O. V. Rudenko, "Statistical phenomena," in *Nonlinear Acoustics*, (American Press, San Diego, 1998), pp. 382-388.
- [38] C. K. W. Tam, K. Viswanathan, K. K. Ahuja and J. Panda, "The sources of jet noise: experimental evidence," *J. Fluid Mech.* **615**, 253-292 (2008).
- [39] S. McInerny, K. L. Gee, M. Dowling and M. James, "Acoustical nonlinearities in aircraft flyover data," AIAA paper **2007**, 3654 (2007).
- [40] M. Downing, K. L. Gee, S. A. McInerny, T. B. Neilsen and M. M. James, "Do recent findings on jet noise answer aspects of the Schultz curve?," in *Proc. Mtgs. Acoust.*, **19**, (Acoustical Society of America), p. 040022.
- [41] K. L. Gee, B. P. Petitjean, D. K. McLaughlin and V. W. Sparrow, "Nonlinear propagation of noise radiated from supersonic jets," in *Proc. Noise-Con 04*
- [42] K. L. Gee, T. B. Gabrielson, A. A. Atchley and V. W. Sparrow, "Preliminary Analysis of Nonlinearity in Military Jet Aircraft Noise Propagation," *AIAA Journal* **43**, 1398-1401 (2005).
- [43] M. B. Muhlestein and K. L. Gee, "Statistical Analysis of Nonlinearly Propagating Acoustic Noise in a Tube," (2012).
- [44] M. B. Muhlestein, "Analyses of nonlinearity measures in high-amplitude sound propagation," Brigham Young University, 2013.
- [45] K. L. Gee, A. A. Atchley, L. E. Falco and M. R. Shepherd, "Nonlinearity analysis of model-scale jet noise," *AIP Conf. Proc.* **1474**, 307-310 (2012).

- [46] K. L. Gee, A. A. Atchley, L. E. Falco, M. R. Shepherd, L. S. Ukeiley, B. J. Jansen and J. M. Seiner, "Bicoherence analysis of model-scale jet noise," *J. Acoust. Soc. Am.* **128**, EL211-EL216 (2010).
- [47] T. B. Neilsen, K. L. Gee, A. T. Wall and M. M. James, "Similarity spectra analysis of high-performance jet aircraft noise," *J. Acoust. Soc. Am.* **133**, 2116-2125 (2013).
- [48] S. N. Gurbatov and O. V. Rudenko, "Statistical phenomena," in *Nonlinear Acoustics*, (American Press, San Diego, 1998), pp. 377-398.
- [49] K. L. Gee, T. B. Neilsen and A. A. Atchley, "Skewness and shock formation in laboratory-scale supersonic jet data," *J. Acoust. Soc. Am.* **133**, EL491-EL497 (2013).
- [50] H. Bass, L. Sutherland, A. Zuckerwar, D. Blackstock and D. Hester, "Atmospheric absorption of sound: Further developments," *J. Acous. Soc. Am.* **97**, 680-683 (1995).
- [51] R. Fiévet, C. E. Tinney, W. J. Baars and M. F. Hamilton, "Coalescence in the Sound Field of a Laboratory-Scale Supersonic Jet," *AIAA Journal*, 1-12 (2015).
- [52] J. E. Ffowcs Williams, J. Simson and V. J. Virchis, "'Crackle': An annoying component of jet noise," *J. Fluid Mech.* **71**, 251-271 (1975).
- [53] W. J. Baars and C. E. Tinney, "Quantifying supersonic jet noise crackle," in *FFSIC*, Proceedings of FFSIC, 2013)
- [54] K. L. Gee, T. B. Neilsen, A. T. Wall, M. B. Muhlestein, J. M. Downing, M. M. James and R. L. McKinley, "On the Evolution of Crackle in Jet Noise from High-Performance Engines," in *19th AIAA/CEAS Aeroacoustics Conference*, (American Institute of Aeronautics and Astronautics, 2013).
- [55] J. W. Nichols, S. K. Lele, F. E. Ham, S. Martens and J. T. Spyropoulos, "Crackle noise in heated supersonic jets," *J. Eng. Gas Turb. Power* **135**, 051202 (2013).

- [56] M. M. James, A. R. Salton, J. M. Downing, K. L. Gee, T. B. Neilsen, B. O. Reichman, R. McKinley, A. T. Wall and H. Gallagher, "Acoustic Emissions from F-35 Aircraft during Ground Run-Up," in *21st AIAA/CEAS Aeroacoustics Conference*), p. 2375.
- [57] K. L. Gee, T. B. Neilsen, D. C. Thomas, B. O. Reichman, M. Muhlestein, J. M. Downing, M. M. James and R. L. McKinley, "Comparison of two time-domain measures of nonlinearity in near-field propagation of high-power jet noise," AIAA Paper 2014-3199, (2014).
- [58] K. L. Gee, T. B. Neilsen and M. M. James, "On the crest factor of noise in full-scale supersonic jet engine measurements," in *Proc. Mtgs. Acoust.*, **20**, (Acoustical Society of America), p. 045003.
- [59] K. L. Gee, J. M. Downing, M. M. James, R. C. McKinley, R. L. McKinley, T. B. Neilsen and A. T. Wall, "Nonlinear evolution of noise from a military jet aircraft during ground run-up," AIAA Paper 2012-2258, (2012).
- [60] T. F. Embleton, "Tutorial on sound propagation outdoors," *J. Acous. Soc. Am.* **100**, 31-48 (1996).
- [61] B. Reichman, A. T. Wall, K. L. Gee, T. B. Neilsen, J. M. Downing, M. M. James and R. L. McKinley, "Modeling Far-field Acoustical Nonlinearity from F-35 Aircraft during Ground Run-up," AIAA Paper 2016-1888, (2016).

# Appendix A

## Computing $v_N$ for One-Third-Octave Bands

When computing  $v_N$  for one-third-octave (OTO) bands, simply summing the narrowband  $v_N$  values over frequency bins does not provide a correct answer. The indicator has units of dB/m, and decibels cannot be summed in the same way that pressure units can be summed. Instead, the change in dB/m must first be converted to a change in Pa/m and then summed. This appendix outlines how this is to be done.

First,  $v_N$  represents a change in sound pressure level over distance, or

$$v_N = \lim_{dx \rightarrow 0} \frac{10 \log_{10}(p_2^2/p_{\text{ref}}^2) - 10 \log_{10}(p_1^2/p_{\text{ref}}^2)}{dx} = \lim_{dx \rightarrow 0} \frac{10 \log_{10}(p_2^2/p_1^2)}{dx}, \quad (\text{A.1})$$

where  $p_1$  is the pressure at  $x$  and  $p_2$  is the pressure at  $x + dx$ . Solving Eq. (A.1) for  $p_2$ , the predicted pressure, and removing the limit expression gives

$$p_2^2 = p_1^2 10^{v_N dx/10}. \quad (\text{A.2})$$

Using Eq. (A.2), the derivative of the squared pressure can then be found in terms of  $v_N$  and the initial pressure,  $p_1$ :

$$\frac{dp^2}{dx} = \lim_{dx \rightarrow 0} \frac{p_2^2 - p_1^2}{dx} = \lim_{dx \rightarrow 0} \frac{p_1^2}{dx} (10^{v_N dx/10} - 1) = \frac{p_1^2 v_N}{10} \ln(10). \quad (\text{A.3})$$

This expression can now be summed over OTO bands.

After summing, the derivative of pressure squared must then be converted back to a change in dB/m. Variables that have been summed over OTO bands are denoted with an overbar. Solving Eq. (A.3) for the predicted squared pressure summed over OTO bands,  $\overline{p_2^2}$ , gives

$$\overline{p_2^2} = \lim_{dx \rightarrow 0} \overline{p_1^2 v_N} \frac{dx}{10} \ln(10) + \overline{p_1^2} . \quad (\text{A.4})$$

Averaging Eq. (A.1) over OTO bands and using Eq. (A.4) to calculate the averaged indicator,  $\overline{v_N}$ , then yields the useful form,

$$\overline{v_N} = \lim_{dx \rightarrow 0} \frac{10 \log_{10}(\overline{p_2^2}/\overline{p_1^2})}{dx} = \lim_{dx \rightarrow 0} \frac{10}{dx} \log_{10} \left( \frac{\overline{p_1^2 v_N} dx}{\overline{p_1^2}} \frac{1}{10} \ln(10) + 1 \right) = \frac{\overline{p_1^2 v_N}}{\overline{p_1^2}} . \quad (\text{A.5})$$

One other method to calculate the averaged  $\overline{v_N}$  value goes back to its definition in Eq. (1.8). All of the terms are constants over frequency except for the terms grouped in parentheses in the following equation:

$$v_N = -10 \log_{10}(e) \times \frac{\beta}{\rho_0 c_0^3} \left( \frac{\omega Q_{pp^2}}{S_{pp}} \right) . \quad (\text{A.6})$$

Thus an alternate way of computing the averaged indicator is

$$\overline{v_N} = -10 \log_{10}(e) \times \frac{\beta}{\rho_0 c_0^3} \left( \frac{\omega Q_{pp^2}}{S_{pp}} \right) . \quad (\text{A.7})$$

Both Eqs. (A.5) and (A.7) have been tested experimentally and yield identical results for  $v_N$  over OTO bands.